Bergische Universität Wuppertal

Doctoral Thesis

Optimal creation operators for charmonium spectroscopy on the lattice

---

Author:
Juan Andrés Urrea-Niño

Supervisors:
Prof. Dr. Francesco Knechtli
Prof. Dr. Michael Peardon

A thesis submitted in fulfillment of the requirements
for the degree of Doctor of Natural Science

in the

High Performance Computing in Theoretical Physics Group
Fakultät für Mathematik und Naturwissenschaften

BERGISCHE
UNIVERSITÄT
WUPPERTAL

September 4, 2023

Declaration of Authorship

I, Juan Andrés URREA-NIÑO, declare that this thesis titled, "Optimal creation operators for charmonium spectroscopy on the lattice" and the work presented in it are my own. I confirm that:

- This work was done wholly or mainly while in candidature for a research degree at this University.
- Where any part of this thesis has previously been submitted for a degree or any other qualification at this University or any other institution, this has been clearly stated.
- Where I have consulted the published work of others, this is always clearly attributed.
- Where I have quoted from the work of others, the source is always given. With the exception of such quotations, this thesis is entirely my own work.
- I have acknowledged all main sources of help.
- Where the thesis is based on work done by myself jointly with others, I have made clear exactly what was done by others and what I have contributed myself.

Signed:

Date:

"No hay día que no llegue ni cita que no se cumpla."

Proverb

Abstract

A major problem often faced in hadron spectroscopy within lattice QCD is the signal-to-noise problem of temporal correlation functions between certain types of operators. Examples relevant for this work are iso-scalar mesons and spatial Wilson loops, whose absolute error in the correlation function remains constant in time, leading to short-lived signals from where effective masses are difficult to reliably extract. Furthermore, the existing signal at early times is heavily influenced by the presence of excited states of a same symmetry channel. The distillation technique has been shown to be a versatile tool to address these issues, where excited state contamination is suppressed by smearing the quark fields. This work presents an improvement to distillation by introducing the optimal meson distillation profiles and showing how these can be built and customized for different kinds of meson operators.

The testing ground for this new method are two $N_f = 2$ ensembles with clover-improved Wilson fermions at half the physical charm quark mass with different lattice spacings and physical volumes. The effective masses of the ground state from a wide variety of local and derivative-based iso-vector charmonium operators, including ones with exotic quantum numbers, are shown to have considerably reduced excited-state contamination at early times thanks to this improvement when compared to standard distillation. This leads to earlier, and in most cases longer, effective mass plateaus from where the mass of the state can be extracted. Effective masses of the first excited states for most of the operators are also accessible purely due to the use of the proposed method. Iso-scalar operators are also studied with the optimal profiles since the absence of light quarks restricts the possible mixing of glueballs to happen only with the charmonium states. The ground state mass of the 0^{-+} channel displays a non-negligible positive shift from the iso-vector one. The ground state mass of the 0^{++} agrees with that from spatial Wilson loops, which are purely gluonic operators. This agreement points at a possible mixing of gluonic and mesonic components which can be studied at early times thanks to the optimal profiles.

A close-to-physical setup to further apply the profiles is an $N_f = 3 + 1$ ensemble with clover-improved Wilson fermions at the $SU(3)$ light flavor symmetric point, physical charm quark mass and pion mass $m_\pi \approx 420$ MeV. The spectrum of the charmonium states which in nature are below the $D\bar{D}$ threshold is calculated using the optimal profiles, with all effective masses displaying a significant suppression of excited state contamination compared to standard distillation. Although the disconnected contributions to the correlation functions are not considered due to limited statistics, good agreement is obtained with the spectrum in nature. Mass splittings are also found to agree with nature as well as with state-of-the art lattice calculations with similar, if not smaller, statistical uncertainties.

Acknowledgements

I would like to thank Francesco Knechtli for his constant guidance and support throughout my entire PhD. His door was always open for questions and discussions, both short and long, and many of them were fundamental for this work. Not only did he give me the opportunity to pursue a PhD in such a wonderful topic but also encouraged me to explore the new ideas that appeared along the way, asked the right questions to help me make the most of them and allowed me to present the results that came from them in conferences and workshops of which I keep very fond memories and from which I also learned a lot. He, together with all members of the working group, provided me with a most productive and enjoyable setting for the last couple of years.

I also wish to thank Mike Peardon for many insightful conversations, all the little "homeworks" which always resulted in a deeper understanding of the results and illuminating notes which introduced me to the sport of glueball hunting.

I am very grateful to Tomasz Korzec for always taking the time to answer more questions than I can count, be them about physics or programming, as well as for all of his help with everything *qcdlib*-related. All the functionalities that he included there for the sake of this work made the coding endeavor an easier one.

I also want to thank Roman Höllwieser for his help in getting all the data that was used in this thesis as well as for all the discussions about the common points of our research.

I gratefully acknowledge the Gauss Centre for Supercomputing e.V. for supporting this project with computing time on the GCS Supercomputer SuperMUC-NG at the Leibniz Supercomputing Centre. I also gratefully acknowledge financial support from the DFG research unit FOR5269 "Future methods for studying confined gluons in QCD". This work greatly benefited from multiple useful discussions with members of this research unit.

Special thanks go to Francesco Knechtli, Mike Peardon, Tomasz Korzec and Roman Höllwieser for their comments and suggestions on previous versions of this thesis. Any mistakes in it are however my own.

Finally I want to thank my parents and my sister as I would not be who I am today and where I am today without their unconditional support. This work is for them.

Contents

Dedicated to my parents and sister.

Chapter 1

Introduction

Quantum Chromodynamics (QCD) is the quantum field theory which describes the dynamics between quarks and gluons,the building blocks for hadrons, via the strong interaction. The Standard Model of particle physics contains 6 different flavors of quarks (**u**p, **d**own, **c**harm, **s**trange, **t**op and **b**ottom) which are fermions with spin $\frac{1}{2}$ and are always bound together by gluons, with the the latter being a spin 1 vector gauge boson. The simplest of these bounded states are mesons; a quark q and an anti-quark $\bar{q}$. The case of interest for this work is charmonium, expressed as $\bar{c}c$ to signify the presence of a charm quark c and an anti-charm quark $\bar{c}$ together. Charmonium states are identified by their total angular momentum J, parity P and charge conjugation symmetry C within the quark model [1–3] and their physical properties (mass, decay width, decay modes, etc...) can be found in the Particle Data Group database [4]. Considering only the strong interaction, $\bar{c}c$ states can decay (at the simplest level) into pairs of so-called charmed mesons, i.e $\bar{c}c \to \bar{c}q + \bar{q}c$ with $q \in \{u, d, s\}$, or into uncharmed states via quark-anti-quark annihilation, e.g $\bar{c}c \to \bar{u}u, \bar{d}d, \bar{s}s$. Charmed mesons involving up, down and strange quarks are called D-mesons and a $\bar{c}c$ state must have an energy of at least twice the mass of the lightest D-meson in order to be able to decay into a pair at rest, a restriction called the $D\bar{D}$ or open charm threshold. Charmonium states with energy below this threshold can only decay via intermediate gluonic exchange and while such decays are observed, they are heavily suppressed. This phenomenon inspired the OZI rule [3, 5–7], which dictates processes which have an intermediate state made entirely of gluon lines are suppressed (or "forbidden") compared to those who do not, where the former are denoted as disconnected and the latter as connected. The η_c (0^{-+}), J/ψ (1^{--}), χ_{c0} (0^{++}), χ_{c1} (1^{++}), h_c (1^{+-}), χ_{c2} (2^{++}) and the first radial excitations $\eta_c(2S)$ and $\Psi(2S)$ are the only charmonium states with masses below the $D\bar{D}$-threshold in nature and therefore can only decay via the OZI-forbidden processes. Such processes are of particular interest since they can also involve a final state made entirely of gluons, a so-called glueball, where there are no quarks or anti-quarks [8–10]. These glueball states arise due to the gluon self-interaction. They are a theoretical prediction of QCD which has not yet been experimentally confirmed and their possible mixing with $\bar{q}q$ states proves a major difficulty for their detection.

To study these states and their dynamics one needs to work at small energy scales, e.g given by their masses. Since QCD exhibits confinement and the coupling constant increases as the energy decreases, a perturbative approach is not feasible. One relies on lattice QCD, a non-perturbative framework which will be explained in Chapter 2, where QCD is formulated on a discrete lattice and the spectrum of strongly interacting particles can be computed. Lattice QCD has exhibited great success reproducing experimental results, which serves as a non-trivial validation of QCD. In this framework, masses are calculated from statistical averages over Markov Chains of temporal correlation functions between lattice hadron/glueball operators. Unfortunately, the results related to quark-anti-quark annihilation processes and glueballs tend to present large statistical fluctuations and a signal-to-noise problem. Different strategies are often used to try to overcome these difficulties. For glueball spectroscopy the use of large statistics and improved operators are the standard procedures, particularly since the measurement of these operators is computationally cheap [11–15]. For meson spectroscopy a common alternative is to neglect the effects of the quark-anti-quark annihilation, since the remaining connected correlation functions generally exhibit a considerably better signal. Such choice was justified by the expectation that these neglected effects are small due to the OZI rule. Although the dynamics behind the OZI rule in the non-perturbative regime is not completely clear, charm annihilation effects were initially estimated to be around $1-4$ MeV [16]. A recent indirect lattice measurement of these effects on the mass of the η_c is an upward shift of $7.3(1.2)$ MeV [1] [17], which confirms it is small yet not negligible with the attainable precision. Other direct lattice measurements give values of similar magnitude and same sign [18]. Furthermore, since perturbative non-relativistic QCD calculations predict an effect of similar magnitude but opposite sign [19–22] there is an indication that these effects are not fully understood and should be studied. Regardless of their magnitude, the disconnected contributions are necessary to study the mixing between charmonium and glueballs. A common tool to compute them is distillation [23], where the quark fields are projected onto the low energy degrees of freedom relevant for hadron spectroscopy. This work presents a simple yet versatile improvement which optimizes the meson operators involved in the charmonium and glueball mixing calculations. The work is organized as follows. Chapter 2 provides a brief overview of lattice QCD and the methods relevant for hadron spectroscopy. Chapter 3 deals with how charmonium is studied with focus only on the connected contributions, introduces the proposed improvement to distillation and compares the resulting charmonium spectrum obtained with standard and improved distillation in two $N_f = 2$ ensembles. Chapter 4 shows how this method can also be used when the disconnected contributions are taken into account for the calculation of the charmonium spectrum as well as for mixing with gluonic operators. Chapter 5 shows how the proposed improvement is also applicable in a close-to-physical $N_f = 3+1$ ensemble with a physical charm quark and three degenerate light quarks. Finally, Chapter 6 closes this work with conclusions about the obtained results together with a discussion about additional applications of the proposed improvement and future directions of study.

---

[1] Natural units with $\hbar = 1$ and $c = 1$ are used in this work.

Chapter 2

Methods

> Count what is countable, measure what is measurable and what is not measurable, make measurable.
>
> Galileo Galilei

This chapter presents the theoretical and numerical methods used in this work. All of them are either contained in or applicable to the lattice Quantum Chromodynamics, or lattice QCD, framework. A general, non-exhaustive overview of this framework and its methods will be presented, with emphasis only on the ones directly relevant for this work. References for the different topics covered will be given such that the reader can find all details and discussions omitted here.

2.1 Lattice QCD

Lattice QCD is a non-perturbative, discretized approach to QCD, the quantum field theory that describes the strong interaction, which allows for direct calculation of quantities otherwise intractable in the continuum. First proposed in [24], a thorough introduction to the topic can be found in [25–28]. Here only the basics regarding the treatment of the relevant fields and their use for hadron spectroscopy will be presented.

2.1.1 Fields on a lattice

The continuum space-time is discretized by defining a lattice Λ with N_L sites in each of the three spatial directions and N_t in the temporal direction. The lattice can be defined by these sites as

$$\Lambda := \{x | x = (t, \vec{x}); t = ax_0; \vec{x} = a(x_1, x_2, x_3); x_1, x_2, x_3 = 0, ..., N_L - 1; x_0 = 0, ..., N_t - 1\}, \tag{2.1}$$

where a is the lattice spacing, taken as equal for space and time directions to form an isotropic lattice. The case of anisotropic lattices will not be considered in this work. The quark fields take values at every site of the lattice Λ,

$$\psi^{(f)}(x)_{\substack{\alpha \\ c}}$$
$$\bar{\psi}^{(f)}(x)_{\substack{\alpha \\ c}}$$

where f is the index for the flavor of the quark, $c = 1, 2, 3$ is a color index and $\alpha = 0, 1, 2, 3$ is a Dirac index. The variables $\psi^{(f)}(x)_{\substack{\alpha \\ c}}$ and $\bar{\psi}^{(f)}(x)_{\substack{\alpha \\ c}}$ are Grassmann variables, which means the following anti-commutation relations hold:

$$\begin{aligned}\left\{\psi^{(f_1)}(x)_{\substack{\alpha_1\\c_1}}, \psi^{(f_2)}(y)_{\substack{\alpha_2\\c_2}}\right\} &= 0\\ \left\{\bar{\psi}^{(f_1)}(x)_{\substack{\alpha_1\\c_1}}, \bar{\psi}^{(f_2)}(y)_{\substack{\alpha_2\\c_2}}\right\} &= 0\\ \left\{\psi^{(f_1)}(x)_{\substack{\alpha_1\\c_1}}, \bar{\psi}^{(f_2)}(y)_{\substack{\alpha_2\\c_2}}\right\} &= 0.\end{aligned} \tag{2.2}$$

Introducing the gauge field variables on the lattice is not as straightforward as for the fermion fields. In the continuum formulation one works with the gluon field $A_\mu(x)$ corresponding to a hermitian and traceless 3×3 matrix for a fixed x and μ. In the lattice formulation one does not work directly with $A_\mu(x)$ but rather with the SU(3) matrices $U_\mu(x)$. $U_\mu(x)$ is defined to live on the link that connects lattice points x and $x + \hat{\mu}$[1] and because of this it is called a link variable. These variables also have an orientation defined by

$$U_{-\mu}(x) = U_\mu(x - \hat{\mu})^\dagger, \tag{2.3}$$

and can be related to the original gauge fields via

$$U_\mu(x) = e^{iaA_\mu(x)}. \tag{2.4}$$

$U_\mu(x)$ is interpreted as a parallel transporter between the two lattice points it connects. The gauge transformations applied to the fermion and gauge fields are defined by introducing a set of SU(3) matrices $\Omega(x)$

$$\begin{aligned}\psi(x) &\to \Omega(x)\psi(x)\\ \bar{\psi}(x) &\to \bar{\psi}(x)\Omega(x)^\dagger\\ U_\mu(x) &\to \Omega(x)U_\mu(x)\Omega(x+\hat{\mu})^\dagger.\end{aligned} \tag{2.5}$$

It is important to note the gauge transformation involves only the color indices of the fermion and gauge fields. Other transformations relevant for these fields are parity, where $\vec{x} \to -\vec{x}$, and charge conjugation, where all particles turn into their anti-particles and therefore all charges change sign. Under parity the fields transform as

$$\begin{aligned}\psi(\vec{x},t) &\to \gamma_0\psi(-\vec{x},t)\\ \bar{\psi}(\vec{x},t) &\to \bar{\psi}(-\vec{x},t)\gamma_0\\ U_0(\vec{x},t) &\to U_0(-\vec{x},t)\\ U_i^\dagger(\vec{x},t) &\to U_i(-\vec{x}-\hat{i},t)\end{aligned} \tag{2.6}$$

and under charge conjugation they transform as

$$\begin{aligned}\psi(\vec{x},t) &\to C^{-1}\psi(\vec{t},t)\\ \bar{\psi}(\vec{x},t) &\to -\bar{\psi}(\vec{x},t)C\\ U_\mu(\vec{x},t) &\to U_\mu(\vec{x},t)^*\end{aligned} \tag{2.7}$$

where γ_μ are the Euclidean Dirac matrices (see App. C for the conventions used in this work), C is a charge conjugation matrix satisfying $C\gamma_\mu C^{-1} = -\gamma_\mu^T$, γ_μ^T denotes the transpose of γ_μ and $U_\mu(\vec{x},t)^*$ is the complex conjugate of $U_\mu(\vec{x},t)$. Here

---

[1] $\hat{\mu}$ denotes the displacement vector of length a in direction μ

the time and position variables for the fields are written explicitly instead of in a single space-time variable x because time and space behave differently under the transformations being used. A final set of relevant transformations are those corresponding to rotations of 90° and axis reflections. These transformations are elements of the Lorentz group which can be realized on the lattice. For this work the most relevant transformations are those of space and time reversal and therefore only those will be explicitly presented, however the missing ones can be obtained by extending the presented ones appropriately. A rotation of 90° in the $\mu\nu$-plane corresponds to the change of space coordinates $x'_\mu = -x_\nu$, $x'_\nu = x_\mu$ such that the position vector $\vec{x} = (x_1, x_2, x_3)$ gets transformed into $\vec{x}' = (x'_1, x'_2, x'_3)$. The fields transform according to

$$\begin{aligned}
\psi(\vec{x},t) &\to \frac{1}{\sqrt{2}}\left(1+\gamma_\mu\gamma_\nu\right)\psi(\vec{x}',t) \\
\bar{\psi}(\vec{x},t) &\to \bar{\psi}(\vec{x}',t)\frac{1}{\sqrt{2}}\left(1-\gamma_\mu\gamma_\nu\right) \\
U_\rho(\vec{x},t) &\to \begin{cases} U_\nu(\vec{x}',t) & if\ \rho=\mu \\ U^\dagger_\mu(\vec{x}'-\hat{\mu},t) & if\ \rho=\nu \\ U_\rho(\vec{x}',t) & \text{otherwise} \end{cases}
\end{aligned} \tag{2.8}$$

A 3D axis reflection transforms the space coordinates as $x'_\mu = -x_\mu$ and the fields transform according to

$$\begin{aligned}
\psi(\vec{x},t) &\to \gamma_\mu\gamma_5\psi(\vec{x}',t) \\
\bar{\psi}(\vec{x},t) &\to \bar{\psi}(\vec{x}',t)\gamma_5\gamma_\mu \\
U_\nu(\vec{x},t) &\to \begin{cases} U_\nu(\vec{x}',t) & \nu\neq\mu \\ U^\dagger_\nu(\vec{x}'-\hat{\mu},t) & \nu=\mu \end{cases}
\end{aligned} \tag{2.9}$$

The previously presented parity transformation is a special case of such reflections where all 3 coordinates change sign. Finally, a temporal axis reflection, or time-reversal, transforms the temporal coordinate as $t' = -t$ and the fields transform according to

$$\begin{aligned}
\psi(\vec{x},t) &\to \gamma_0\gamma_5\psi(\vec{x}',t') \\
\bar{\psi}(\vec{x},t) &\to \bar{\psi}(\vec{x}',t')\gamma_5\gamma_0 \\
U_\nu(\vec{x},t) &\to \begin{cases} U_\nu(\vec{x},t') & \nu\neq 0 \\ U^\dagger_\nu(\vec{x},t'-a) & \nu=0 \end{cases}
\end{aligned} \tag{2.10}$$

These transformations form a representation of Lorentz group. A detailed treatment of such transformations in the continuum and using Minkowski space-time can be found in [29, 30] and the corresponding transformation rules in Euclidean space-time that can be realized on the lattice are taken from [31]. These transformations play an important role when defining the action of the theory. For the isotropic lattices considered in this work, the action must be invariant under all of these transformations. They are also important when one defines the different hadron operators that are relevant for this work, since these must have defined symmetries under these transformations.

2.1.2 The action on the lattice

The dynamics of the quark and gauge fields on the lattice can be encoded in an action $S[\psi,\bar{\psi},U]$, expressed as the sum of a fermionic action $S_F[\psi,\psi,U]$, which will describe the dynamics of the fermion fields and their coupling to the gauge field, and a gauge action $S_G[U]$ which describes the dynamics of the gauge field and its self-interaction. To build $S_G[U]$ one needs a functional of link variables $U_\mu(x)$ such that it is gauge invariant and the continuum pure gauge action is recovered in the the continuum limit. i.e $a \to 0$. Several choices of $S_G[U]$ satisfy these conditions. This work uses the Wilson gauge action given by

$$S_G[U] = \frac{2}{g^2} \sum_{x\in\Lambda} \sum_{\mu<\nu} Re\left[Tr\left(\mathbb{1} - U_{\mu\nu}(x)\right)\right], \tag{2.11}$$

where $U_{\mu\nu}(n)$ is the plaquette defined as

$$U_{\mu\nu}(x) = U_\mu(x)U_\nu(x+\hat{\mu})U^\dagger_\mu(x+\hat{\nu})U^\dagger_\nu(x). \tag{2.12}$$

The plaquette is the simplest non-trivial product of link variables along a closed path, and is related to the field strength tensor $F_{\mu\nu}$ as

$$U_{\mu\nu}(x) = e^{ia^2F_{\mu\nu}(x)+\mathcal{O}\left(a^3\right)}, \tag{2.13}$$

and therefore the Wilson gauge action is related to this same tensor as

$$S_G[U] = \frac{a^4}{2g^2} \sum_{x\in\Lambda} \sum_{\mu,\nu} Tr\left[F_{\mu\nu}(x)^2\right] + \mathcal{O}\left(a^6\right). \tag{2.14}$$

In the continuum limit $a^4 \sum_{x\in\Lambda}$ becomes the integral over space-time and the continuum Yang-Mills (YM) gauge action

$$S_{YM} = \frac{1}{2g^2} \int Tr\left[F_{\mu\nu}(x)F_{\mu\nu}(x)\right] dx, \tag{2.15}$$

is recovered. Since the plaquette is a product of link variables in a closed loop and from the cyclic property of the trace, this choice of $S_G[U]$ is invariant under a gauge transformation of the form shown in Eqn. (2.5). This choice also has the advantage of being local since for a fixed point on the lattice it only involves the neighbors that live in the hyper-cube of side $2a$ that enclose the point. Other choices of $S_G[U]$, such as the Lüscher-Weisz gauge action [32], are also based on Wilson loops but involve other beyond the plaquette for partial $\mathcal{O}(a^2)$ improvements. For the fermionic action similar considerations have to be taken into account regarding gauge invariance and the recovery of the continuum action. The choice of $S_F[\psi,\bar{\psi},U]$ used in this work corresponds to the clover-improved Wilson fermion action and is given by

$$S_F[\psi,\bar{\psi},U] = \sum_{i=1}^{N_f} a^4 \sum_{x\in\Lambda} \bar{\psi}^{(i)}(x)\left(D_{xy} + m_i\delta_{xy}\right)\psi^{(i)}(y), \tag{2.16}$$

where N_f is the number of quark flavors considered, m_i is the bare quark mass associated with the quark field $\psi^{(i)}$ and D is the clover-improved Wilson-Dirac operator, given by

$$\begin{aligned} D_{xy} = &\sum_{\mu=0}^{3} \gamma_\mu \left(\frac{U_\mu(x)\delta_{x+\hat{\mu},y} - U_\mu(x-\hat{\mu})^\dagger \delta_{x-\hat{\mu},y}}{2a} \right) \\ &- a \sum_{\mu=0}^{3} \frac{U_\mu(x)\delta_{x+\hat{\mu},y} - 2\delta_{x,y} + U_\mu(x-\hat{\mu})^\dagger \delta_{x-\hat{\mu},y}}{2a^2} \\ &+ \delta_{xy} c_{sw} a \sum_{\mu<\nu} \frac{1}{2} \sigma_{\mu\nu} \hat{F}_{\mu\nu}(x). \end{aligned} \tag{2.17}$$

The different terms in Eqn. (2.17) have different origins and serve different purposes. The first line corresponds to the naive gauge-covariant discretization of the Dirac operator using symmetric differences for the derivatives. The second line corresponds to the Wilson term and it is proportional to the discrete covariant Laplacian operator. This term decouples the fermion doublers that arise due to the discretization which can be explicitly found when considering the free massless case of the first line in Fourier space [25, 26] and are predicted by the Nielsen-Ninomiya no-go theorem [33]. The third line corresponds to the clover improvement [34], where $\sigma_{\mu\nu} = -\frac{i}{2}[\gamma_\mu, \gamma_\nu]$, and involves a discretized version of the field-strength tensor[35]

$$\hat{F}_{\mu\nu}(x) = \frac{-i}{8a^2} \left(Q_{\mu\nu}(x) - Q_{\nu\mu}(x) \right), \tag{2.18}$$

where $Q_{\mu\nu}(x)$ is the sum of the four plaquettes in the $\mu - \nu$ plane starting from point x, given by

$$Q_{\mu\nu}(x) = U_{\mu\nu}(x) + U_{\nu-\mu}(x) + U_{-\mu-\nu}(x) + U_{-\nu\mu}(x). \tag{2.19}$$

This term leads to an $\mathcal{O}(a)$ improvement of the action with an appropriate choice of the Sheikholeslami-Wohlert coefficient c_{sw}. Methods to determine c_{sw} depending on the action can be found in [36, 37]. This improvement follows from the Symanzik improvement program [38, 39] to eliminate lattice artifacts from the action and a complete derivation of this term can be found in [25]. Just as for $S_G[U]$ this choice of fermion action is local since it involves only nearest neighbors via the derivatives in D.

2.2 Hadron spectroscopy

A wide variety of states composed of quarks and gluons can be studied in lattice QCD. Hadron spectroscopy deals with the calculation of their masses. Two kinds are studied this work: mesons and glueballs. Mesons are hadrons composed of a quark and an anti-quark while glueballs are bound states of gluons. Despite their different composition, both have integer total angular momentum J and can be labeled by their quantum numbers J^{PC}, where $P = \pm$ corresponds to the symmetry under parity reversal and $C = \pm$ to the symmetry under charge conjugation. The latter symmetry is defined for unflavored mesons.

2.2.1 Angular momentum on the lattice

The total angular momentum quantum number J labels the irreducible representations (irreps) of the group of three-dimensional rotations, $SO(3)$. Once space-time is discretized into a lattice this group does not leave the lattice invariant. One is therefore restricted to the cubic group O, which has 24 elements that leave a cube, and therefore also a three-dimensional cubic lattice, invariant. This group has only 5 irreps which are labeled as A_1, A_2, E, T_1 and T_2 with dimensions 1, 1, 2, 3 and 3 respectively [40–42]. Due to this restriction there is a subduction of the different J into the irreps of O. This means that from an irrep of $SO(3)$ taking only the matrix elements corresponding to the elements of O will form a reducible representation of O. This representation can then be reduced into a direct sum of the mentioned irreps of O and this decomposition defines the relation between the irreps of $SO(3)$ and those of O which is clearly not one-to-one. The subduction relations are displayed in Table 2.1 up to $J = 4$ and are well-known in the literature. The different entries in this table can be found by following the procedure presented in [42] or group theory books such as [43, 44]. No consideration has been made yet regarding the parity and charge conjugation symmetries. Parity is included by extending the group O into O_h as $O \otimes \mathbb{C}_i$, where $\mathbb{C}_i$ is the group containing only the identity element and the spatial inversion. O_h has 48 elements and 10 irreps which are now labeled as $A_1^\pm$, $A_2^\pm$, $E^\pm$, $T_1^\pm$ and $T_2^\pm$ where the $\pm$ label denotes the parity symmetry [40]. Stating that an object transforms according to irrep $R^\pm$ means that it transforms according to R under the action of O and gains a factor ± 1 under the action of the spatial inversion, i.e the parity transformation. The characters of the irreps of O_h and other useful information of this group and O can be found in [40]. Since charge conjugation does not affect space its inclusion is not done via a modification of the symmetry group and will only be addressed once specific operators are built.

J	Irreps.
0	A_1
1	T_1
2	$E \oplus T_2$
3	$T_1 \oplus T_2 \oplus A_2$
4	$A_1 \oplus T_1 \oplus T_2 \oplus E$

TABLE 2.1: Subduction of J into the lattice irreps up to $J = 4$.

2.2.2 Operators on the lattice

An important step in hadron spectroscopy is to build operators that transform according to a chosen irrep under the action of the elements of O and that also have a fixed symmetry under parity reversal and charge conjugation. As previously presented, these irreps are directly linked to the J^{PC} quantum numbers of interest. However, due to the subduction it is more convenient to characterize operators via R^{PC}, with $R \in \{A_1, A_2, E, T_1, T_2\}$. To identify the correct J quantum number from operators that transform according to an irrep R one can count degeneracies in the obtained spectrum according to Table 2.1 or use the method described in [45] for the case of meson operators, which will be mentioned later when the construction of these operators is presented. To begin the discussion, consider a hadron[2] operator $\mathcal{O}(x)$ that depends on the quark and gauge fields. For the study of masses one is interested in the operator at zero spatial momentum, which can be introduced via a

---

[2] Keep in mind that in this work only hadrons with integer J will be considered, such as meson and glueballs.

spatial Fourier transform as

$$\mathcal{O}(\vec{p}=0,t) = \frac{1}{N_L^3} \sum_{\vec{x}\in\Lambda_{3D}} \mathcal{O}(\vec{x},t), \tag{2.20}$$

where Λ_{3D} denotes all 3D points of the lattice Λ with fixed time t. An appropriate choice of $\mathcal{O}(\vec{x},t)$ guarantees that $\mathcal{O}(\vec{p}=0,t)$ has a fixed R^{PC} behavior and the details for making this choice for meson and glueball operators will be explored later. The observable of interest is the temporal correlation of this zero momentum operator, defined as

$$C(t) = \frac{1}{Z} \int \mathcal{O}(t)\overline{\mathcal{O}}(0) e^{-S[\psi,\bar{\psi},U]} d\left[\psi\right] d\left[\bar{\psi}\right] d\left[U\right], \tag{2.21}$$

with

$$Z = \int e^{-S[\psi,\bar{\psi},U]} d\left[\psi\right] d\left[\bar{\psi}\right] d\left[U\right]. \tag{2.22}$$

Here the $\vec{p}=0$ label is omitted since it is to be understood from now on. Also, $d[U]$ is shorthand notation for

$$d[U] = \prod_{x\in\Lambda} \prod_{\mu=0}^{3} dU_\mu(x), \tag{2.23}$$

which is the product of integration measures for the link variables at each lattice site and in each direction. The individual measure $dU_\mu(x)$ is the Haar measure which characterizes the integration in SU(3)[25, 26]. Similarly, $d\left[\psi\right]$ stands for

$$d\left[\psi\right] = \prod_f \prod_{\alpha=0}^{3} \prod_{c=0}^{2} \prod_{x\in\Lambda} d\psi(x)^{(f)}_{\substack{\alpha \\ c}}, \tag{2.24}$$

and the same for $d\left[\bar{\psi}\right]$. The integrals involving these two measures are Grassmann integrals which can be solved analytically following the rules presented in [25, 26]. For doing so it is convenient to define the quantity

$$\left[\mathcal{O}(t)\overline{\mathcal{O}}(0)\right]_F = \frac{1}{Z_F[U]} \int d\left[\psi\right] d\left[\bar{\psi}\right] \mathcal{O}(t)\overline{\mathcal{O}}(0) e^{-S_F[\psi,\bar{\psi},U]}, \tag{2.25}$$

with

$$Z_F[U] = \int d\left[\psi\right] d\left[\bar{\psi}\right] e^{-S_F[\psi,\bar{\psi},U]}. \tag{2.26}$$

The correlation $C(t)$ can then be written as

$$\begin{aligned} C(t) &= \langle \left[\mathcal{O}(t)\overline{\mathcal{O}}(0)\right]_F \rangle_U \\ &= \frac{1}{Z} \int d\left[U\right] e^{-S_G[U]} Z_F[U] \left[\mathcal{O}(t)\overline{\mathcal{O}}(0)\right]_F. \end{aligned} \tag{2.27}$$

While $\left[\mathcal{O}(t)\overline{\mathcal{O}}(0)\right]_F$ is operator dependent, Z_F can be calculated directly as shown in [25, 26], yielding

$$Z_F[U] = \det\left(D\right) \tag{2.28}$$

for the case when only a single flavor of quark is used. $C(t)$ becomes

$$C(t) = \frac{1}{Z}\int d\left[U\right] e^{-S_G[U]} \det\left(D\right) \left[\mathcal{O}(t)\overline{\mathcal{O}}(0)\right]_F \tag{2.29}$$

and only the integral over the link variables remains. This issue will be addressed shortly and for now it should be assumed that $C(t)$ can be calculated. At this point it is useful to examine the spectral decomposition of this correlation function. In the Hilbert space where the chosen creation and annihilation operators can act this correlation function can be written as [25]

$$C(t) = \frac{Tr\left[e^{-(T-t)\hat{H}}\hat{O}e^{-t\hat{H}}\hat{O}^\dagger\right]}{Tr\left[e^{-T\hat{H}}\right]}, \tag{2.30}$$

where T denotes the temporal extent of the lattice in physical units and periodic boundary conditions in time for the link variables are assumed. The traces can be evaluated by using the energy eigenstates of the Hamiltonian, defined as

$$\hat{H}\left|n\right\rangle = E_n\left|n\right\rangle, \tag{2.31}$$

ordered such that $E_n \leq E_{n+1}$ and normalized such that $\langle n|n\rangle = 1$. The denominator in Eqn. (2.30) is evaluated as

$$\begin{aligned} Tr\left[e^{-T\hat{H}}\right] &= \sum_n e^{-TE_n} \\ &\approx e^{-TE_0} \end{aligned} \tag{2.32}$$

where in the second line the approximation of large T is taken such that only the term including the energy of the vacuum E_0, which is the lowest energy, contributes. The denominator is evaluated as

$$\begin{aligned} Tr\left[e^{-(T-t)\hat{H}}\hat{O}e^{-t\hat{H}}\hat{O}^\dagger\right] &= \sum_m\sum_n \left\langle m\right| e^{-(T-t)\hat{H}}\hat{O}\left|n\right\rangle \left\langle n\right| e^{-t\hat{H}}\hat{O}^\dagger\left|m\right\rangle \\ &= \sum_m\sum_n e^{-(T-t)E_m}\left\langle m\right|\hat{O}\left|n\right\rangle e^{-tE_n}\left\langle n\right|\hat{O}^\dagger\left|m\right\rangle \\ &= \sum_m\sum_n e^{-TE_m-t(E_n-E_m)}|\left\langle n\right|\hat{O}^\dagger\left|m\right\rangle|^2. \end{aligned} \tag{2.33}$$

In the case with periodic boundary conditions in time for the link variables and in the limit where both t and T are large and $T-t$ is close to t, the correlation function can be written as

$$C(t) = \sum_n |\left\langle n\right|\hat{O}^\dagger\left|0\right\rangle|^2\left(e^{-t(E_n-E_0)} + e^{-(T-t)(E_n-E_0)}\right), \tag{2.34}$$

where from now on the energy relative to the vacuum $E_n - E_0$ will be written simply as E_n. Among the energy eigenstates at zero spatial momentum there might be not only one-particle states but also multi-particle states with zero total spatial momentum, e.g two mesons with back-to-back momentum. In the case of the one particle state the energy would correspond to its mass but this will not be the case for a multi-particle state. This work focuses only in the low-lying one particle states and therefore from now on the energies will be denoted as m_n to denote masses, working under the assumption that the measured states correspond to one-particle states. This expression can be further simplified into

$$C(t) = \sum_n |\langle n| \hat{O}^\dagger |0\rangle|^2 2e^{-\frac{T}{2}m_n} \cosh\left(\left(\frac{T}{2} - t\right) m_n\right). \tag{2.35}$$

When t is close enough to $\frac{T}{2}$ only the term containing the energy of the ground state $|G\rangle$ of the fixed J^{PC} numbers, denoted as m_G, remains and one can use the functional approximation:

$$C(t) \approx |\langle G| \hat{O}^\dagger |0\rangle|^2 2e^{-\frac{T}{2}m_G} \cosh\left(\left(\frac{T}{2} - t\right) m_G\right), \tag{2.36}$$

to extract the mass m_G via the root-finding method suggested in [46]. As a final remark, in the case where the operator considered has vacuum quantum numbers, i.e transforms according to A_1^{++}, then one performs a vacuum expectation value subtraction as

$$C(t) = \left\langle \left[\mathcal{O}(t)\overline{\mathcal{O}}(0)\right]_F \right\rangle_U - \langle[\mathcal{O}(t)]_F\rangle_U \left\langle \left[\overline{\mathcal{O}}(0)\right]_F \right\rangle_U \tag{2.37}$$

to eliminate the time-independent term that would otherwise be included in the relevant spectral decomposition. This method for calculating the masses of particles comes with its own caveats, especially regarding the values of $|\langle G| \hat{O}^\dagger |0\rangle|^2$. This quantity represents the overlap of the created state with the true energy eigenstate and if it is not sufficiently large then Eqn. (2.36) only holds for values of t very close to $\frac{T}{2}$. At such values of t the correlation $C(t)$ can be severely affected by noise, making the extraction of m_G particularly difficult.

2.2.3 Accessing different energy levels

From the previous discussion it is clear that the energy of the ground state of a given symmetry channel is the easiest one to access. However one can also be interested in excited states of this same channel. In such cases a more sophisticated numerical tool must be used. The one chosen for this work corresponds to the generalized eigenvalue problem (GEVP) formulation [47, 48]. The starting point of this method is a set of N_B different operators $\mathcal{O}_i$ in the same symmetry channel and the main goal is to build a linear combination that has the largest overlap with a desired energy eigenstate $|e\rangle$. Such optimal operator, denoted as $\mathcal{O}^{(e)}$, can be written as

$$\mathcal{O}^{(e)} = \sum_{i=1}^{N_B} w_e^{(i)} \mathcal{O}_i, \tag{2.38}$$

and the coefficients $w_e^{(i)}$ must be found. As first presented in [47] and further elaborated in [48], the procedure is to build the correlation matrix involving the basis operators as

$$C_{ij}(t) = \left\langle \left[\mathcal{O}_i(t)\bar{\mathcal{O}}_j(0)\right]_F \right\rangle_U, \tag{2.39}$$

and then solve the GEVP given by

$$C(t) z_e(t, t_G) = \lambda_e(t, t_G) C(t_G) z_e(t, t_G), \tag{2.40}$$

with t_G is a reference time, $t_G < t < \frac{T}{2} - a$, $z_e(t, t_G)$ are the N_B different N_B-dimensional generalized eigenvectors and $\lambda_e(t, t_G)$ are the corresponding generalized eigenvalues. The generalized eigenvalues are related to the masses and the latter can be extracted by using the approximation

$$\lambda_e(t, t_G) \approx 2c_0 e^{-\frac{T}{2}m^{(e)}} \cosh\left(\left(\frac{T}{2} - t\right) m^{(e)}\right), \tag{2.41}$$

for the case with periodic boundary conditions in time for the link variables as shown in [46], where the constant c_0 includes the dependence on t_G. This approximation holds up to exponential corrections which decrease in time and depend on the difference $m_e - m_{e+1}$ of the energy eigenstates which are explored in detail in [48]. This same reference shows the generalized eigenvectors $z_e(t, t_G)$ are time-independent up to exponentially suppressed corrections and correspond to the coefficients w_e required in Eqn. (2.38). The presence of statistical noise further affects these approximations, mainly making the recommended choice of large t_G very numerically unstable. An issue that becomes important in the analysis of the generalized eigenvectors and that has been discussed in [49, 50] among others is the fact that there might occur flipping when the corresponding eigenvalues are too close to each other, particularly at large values of time where the GEVP is more sensitive to statistical fluctuations. This phenomenon is important in scenarios like string-breaking; in the region where the string breaks and avoided level-crossing happens the different energy levels yielded by the GEVP get considerably close to each other [51, 52]. In such cases sorting the generalized eigenvalues by magnitude might lead to wrong results and a better strategy is to sort them by the information contained in the generalized eigenvectors. One way to do so, which is used in [50], is to first choose a reference time t_r where the order of the generalized eigenvectors and eigenvalues is trusted. Then for each value $t \neq t_r$ all generalized eigenvectors of time t are compared with the ones of t_r by calculating the inner products $w_e(t_r, t_G)^\dagger C(t_G) w_{e'}(t, t_G)$ and the order is assigned based on the absolute value of these results. This method can nonetheless fail in some cases as discussed in [49] and in this same reference a more robust method for sorting the generalized eigenvectors is presented which is used in this work.

Two additional issues arise when using this GEVP formulation. The first one is related to the basis bias, i.e how the individual features of the N_B basis operators $\mathcal{O}_i$ define the features of the optimal operator $\mathcal{O}^*$. The individual $\mathcal{O}_i$ should create states with sufficient overlap with the energy eigenstate such that the one created by $\mathcal{O}^*$ has a considerable overlap with it as well [52]. The second one is related to the numerical stability of solving the GEVP for the matrix $C(t)$. As will be seen soon this solution involves either the inverse of $C(t_G)$ or of its Cholesky decomposition and the calculation of these matrices is very sensitive to small eigenvalues. Even though the operators are chosen to be different from each other they might be far from orthogonal and near degeneracies can lead to such unwanted small eigenvalues in $C(t_G)$. Statistical fluctuations can make the situation worse by turning the smallest eigenvalues negative, at which point the GEVP formulation is no longer well defined. The basis bias can be addressed by choosing operators with clearly different features, such as different number of lattice derivatives to sample different spatial structures, or by using different sets of operators and checking the consistency of the results obtained. The issue of numerical instability can be addressed by replacing the correlation matrix $C(t)$ in Eqn. (2.40) with a new correlation matrix $\tilde{C}(t)$ with entries given by

$$\tilde{C}_{ij}(t) = u_i^\dagger C(t) u_j, \tag{2.42}$$

where u_i are the N_s singular vectors of $C(t_s)$ with largest singular values at a fixed time t_s where the states of interest are assumed to dominate [53, 54]. This so-called pruning procedure yields a new correlation matrix built from orthonormal operators that contribute the most to the original correlation matrix. This can be seen by explicitly calculating $\tilde{C}(t)$ as follows:

$$\begin{aligned}\tilde{C}_{ij}(t) &= u_i^\dagger C(t) u_j \\ &= \sum_{m,n=1}^{N_B} u_i^{(m)*} C_{mn}(t) u_j^{(n)} \\ &= \sum_{m,n=1}^{N_B} u_i^{(m)*} \left\langle [\mathcal{O}_m(t)\bar{\mathcal{O}}_n(0)]_F \right\rangle_U u_j^{(n)} \\ &= \left\langle \left[\mathcal{Q}_i(t)\bar{\mathcal{Q}}_j(0)\right]_F \right\rangle_U,\end{aligned} \tag{2.43}$$

where $u_j^{(n)}$ is the n-th entry of u_j. The pruned operators are defined as

$$\mathcal{Q}_i(t) = \sum_{m=1}^{N_B} u_i^{(m)*} \mathcal{O}_m(t), \tag{2.44}$$

and are orthogonal in their coefficients thanks to the orthogonality of the singular vectors. Choosing $N_s < N_B$ effectively eliminates the operators corresponding to small singular values of $C(t_s)$ which in turn improves the conditioning of the matrix $\tilde{C}(t)$ and makes the GEVP more numerically stable since since the discarded operators are more sensitive to noise. The GEVP involving $\tilde{C}(t)$ is therefore a better starting point to extract the masses of the different energy eigenstates of interest. This resulting GEVP is solved by turning it into a standard eigenvalue problem via a Cholesky decomposition as shown in [45], which can be done given that $\tilde{C}(t_G)$ is guaranteed to be hermitian and positive definite up to statistical fluctuations. The remaining freedom of phase for these vectors is fixed by demanding that the first entry of each vector is real and positive.

A final issue related to the GEVP formulation is the presence of different time-reversal symmetries in the entries of the correlation matrix. Such a case can only happen in an off-diagonal entry $C_{ij}(t)$ if the operators $\mathcal{O}_i(t)$ and $\mathcal{O}_j(t)$ have opposite time-reversal symmetries and therefore

$$C_{ij}(t) = -C_{ij}(-t). \tag{2.45}$$

Such a case was studied in [55], showing that in the presence of periodic boundary conditions in time for the link variables the generalized eigenvalues no longer have a leading cosh() behavior from where effective masses can be extracted. To avoid the subtleties of such a case, all correlation matrices built in this work will be even under time-reversal.

2.2.4 Smearing of Gauge Fields

Many hadron operators in the lattice depend on the gauge links and these often suffer from short-range fluctuations that introduce noise in the calculations where the long distance behavior is of interest. To face this issue different methods of link smearing can be used. These methods replace each link with a function that relates said link and its close neighbors. This replacement not only suppresses short-range variations but if different smearing schemes are used then one can define multiple hadronic operators of the same symmetry channel to use in the GEVP formulation. Some examples of link smearing methods are APE smearing [56], improved APE smearing [12], HYP smearing [57], Stout smearing [58] and link Fuzzing [59]. In this work only 3D APE smearing will be used and therefore only this strategy will be briefly explained. 3D APE smearing proceeds with the following replacement:

$$\tilde{U}_\mu(\vec{x},t) = Proj_{SU(3)}\left[U_\mu(\vec{x},t) + \alpha_{APE}\sum_{\substack{\nu=1\\ \nu\neq\mu}}^{3} \mathcal{C}_{\mu\nu}(\vec{x},t)\right] \tag{2.46}$$

where α_{APE} is a real parameter generally taken between 0 and $\frac{2}{3}$ due to considerations explained in [60] and $\mathcal{C}_{\mu\nu}(\vec{x},t)$ is the sum of each pair of staples along perpendicular spatial directions defined as

$$\mathcal{C}_{\mu\nu}(\vec{x},t) = U_\nu(\vec{x},t)U_\mu(\vec{x}+\hat{\nu},t)U^\dagger_\nu(\vec{x}+\hat{\mu},t) \tag{2.47}$$

$$+ U^\dagger_\nu(\vec{x}-\hat{\nu},t)U_\mu(\vec{x}-\hat{\nu},t)U_\nu(\vec{x}-\hat{\nu}+\hat{\mu},t). \tag{2.48}$$

The projection back onto SU(3) is performed because the weighted sum of SU(3) elements is not an element of said group. This projection is not unique and the one used in qcdlib corresponds to the one presented in [15]. The smeared link variable $\tilde{U}_\mu(\vec{x},t)$ can be viewed as an average of neighboring paths that connect the sites $\vec{x}$ and $\vec{x}+\hat{\mu}$ at a fixed time t, suppressing the short-range fluctuations that might be present. The smearing step in Eqn. (2.46) can be repeated iteratively, yielding the smearing step

$$\tilde{U}^{(i+1)}_\mu(\vec{x},t) = Proj_{SU(3)}\left[U^{(i)}_\mu(\vec{x}) + \alpha_{APE}\sum_{\substack{\nu=1\\ \nu\neq\mu}}^{3} C^{(i)}_{\mu\nu}(\vec{x},t)\right], \tag{2.49}$$

where $C^{(i)}_{\mu\nu}(\vec{x},t)$ is built as in Eqn. (2.48) using the gauge field $U^{(i)}$. Different choices of smearing schemes together with different choices of smearing parameters (number of iterations N_{APE}, α_{APE}) can be used to build creation operators for the GEVP formulation. The choice of the smearing parameters must be done very carefully. On one hand, under-smearing must be avoided since failing to reduce short-distance fluctuations makes the additional work pointless. On the other hand, over-smearing can damage long-range features. As shown in [56, 60, 61] the 3D APE-smeared gauge links have a "footprint" given by $\langle r^2\rangle^{\frac{1}{2}} = \frac{\sqrt{N_{APE}\alpha_{APE}}}{\sqrt{2}}$ in units of a single lattice spacing. Unwanted scenarios include this quantity being close to or larger than half of the spatial extent of the lattice, since long-range features would be eliminated and wrapping around the periodic boundaries of the 3D lattice can also occur.

2.2.5 Monte-Carlo integration with link variables

The explicit calculation of the different correlation functions for hadron spectroscopy requires the computation of integrals over the gauge link variables with the form

$$C(t) = \frac{1}{Z}\int dU e^{-S_G[U]} det(D)\left[\mathcal{O}(t)\bar{\mathcal{O}}(0)\right]_F. \tag{2.50}$$

It is worth remembering that dU is shorthand notation for the product of all the involved group invariant measures

$$dU = \prod_{x\in\Lambda}\prod_{\mu=0}^{3} dU_\mu(x), \tag{2.51}$$

where $dU_\mu(x)$ is the Haar measure for the integration of the link variable connecting lattice point x with $x+\hat{\mu}$ over SU(3). Such integrals are only analytically solvable for very simple integrands and the integrand in Eqn. (2.54) is not one of these cases so it becomes necessary to numerically estimate the result. One case relevant for this work is that of 2 degenerate quark fields, which means that the factor $det(D)$ in Eqn. (2.54) must be replaced with $det(D^2)$. It can be shown that

$$det(D^2) = det(D^\dagger D) \tag{2.52}$$

using the γ_5-hermiticity of D and therefore $det(D^2)$ is a non-negative real number, which is of vital importance for the numerical estimation to be done. Namely, since the term

$$p(U) = \frac{1}{Z} e^{-S_G[U]} det(D^2) \tag{2.53}$$

is positive, normalized and a function of the link variables, it can be treated as a probability density function. With this in mind, the integral at hand is the expectation value of $[\mathcal{O}(t)\bar{\mathcal{O}}(0))]_F$. For the sake of clarity it is convenient to work for now with the expectation value of an observable $A[U]$ which depends only on the gauge links of the form

$$\langle A\rangle_U = \frac{1}{Z}\int dU e^{-S_G[U]} det(D^2) A[U]. \tag{2.54}$$

This expectation value can be approximated via Monte-Carlo estimation as

$$\langle A\rangle_U \approx \frac{1}{N_{MC}}\sum_{i=1}^{N_{MC}} A[U_i], \tag{2.55}$$

where U_i is a gauge configuration sampled according to Eqn. (2.53) and N_{MC} is the total number of configurations used. To do this estimation it is necessary to be able to sample gauge configurations according to the desired probability density function. In this work Markov Chain Monte Carlo (MCMC) is the method of choice for this sampling. In MCMC a chain of configurations U_1, U_2,... is created such that there is a value j such that the configurations U_j, U_{j+1}, ... can be considered to be sampled from the desired distribution and the chain is said to be thermalized. In this chain U_i is built from U_{i-1} and the initial configuration U_1 can be chosen arbitrarily (subjected to the restriction to SU(3)). There exist different ways of generating the chain of configurations and the ones used in this work were generated using the Hybrid

Monte Carlo (HMC) method first proposed in [62]. In this method a candidate for a new configuration is created from the previous one via the solution of Hamiltonian equations of motion that involve the link variables and artificially-introduced momenta variables. A detailed explanation of this method can be found in [25, 26], where the determinant involved in the calculations is often approximated via the pseudo-fermion approach [63].

Eqn. (2.55) has an statistical uncertainty associated to it. If the configurations used are independent from each other this error can be estimated as

$$\delta_A = \frac{\sigma_A}{\sqrt{N_{MC}}}, \tag{2.56}$$

where σ_A is the standard deviation of A. However, given the configurations generated in the MCMC method are part of a same Markov chain, and therefore may be correlated, one needs to take this so-called auto-correlation into account when estimating the error of the calculated average. The Γ-method described in [64, 65] is used for this purpose, as well as to take into account correlations between different observables analyzed on the same chain of configurations. The latter is of particular importance since the extraction of masses involves the correlation function at different values of time and the solution of the GEVP where the different entries of the relevant correlation matrices may be correlated. The *pyerrors* [66] implementation of the Γ-method in Python is used which employs automatic differentiation [67] for the calculation of all derivatives involved. This feature is of particular importance when analyzing quantities which can become very small and therefore the numerical evaluation of derivatives can become unstable without a fine tuning of the step-size used and automatic differentiation eliminates this problem.

2.3 Distillation

Quark smearing techniques seek to create a smoother, more extended field which better approximates the physical state of interest. Most methods available are iterative, similar to the case of the link variables. Notable examples are the *Wuppertal* smearing [68, 69], *Jacobi* smearing [69–71] and *Gaussian* smearing [70, 72–74]. The success of these techniques comes from the fact that simulate wave functions with extended spatial structure, better approximating the non point-like structure of realistic hadrons [25, 26, 75]. This is done by linearly and gauge covariantly combining the quark fields to avoid the appearance of new Wick contractions. A widely used non-iterative quark smearing scheme is distillation [23] and to better understand how it works it is useful to explore its relation to the iterative schemes. A good starting point is the explanation presented in [76] regarding the Jacobi. One can define a smeared field with a Gaussian profile of parameter σ^2 and no defined gauge symmetry as

$$\tilde{\psi}(\vec{x}, t; \sigma^2) \propto \int e^{-\frac{\vec{r}^2}{4\sigma^2}} \psi(\vec{x} + \vec{r}, t) d^3r, \tag{2.57}$$

where the normalization constant is ignored given that it is not immediately relevant for the discussion. With the initial condition $\tilde{\psi}(\vec{x}, t; \sigma^2 = 0) = \psi(\vec{x}, t)$ and the relation

$\sigma^2 = \kappa\tau$ the smeared field is a solution to the diffusion equation

$$\frac{\partial\tilde{\psi}(\vec{x},t;\sigma^2)}{\partial\tau} = \kappa\nabla^2\tilde{\psi}(\vec{x},t;\sigma^2), \tag{2.58}$$

where τ is a diffusion time and κ a diffusion constant. A discrete version of Eqn. (2.58) that describes a single step of this smearing, with κ fixed as a smearing parameter, is

$$\frac{\tilde{\psi}(\vec{x},t;\kappa(\tau+\Delta\tau)) - \tilde{\psi}(\vec{x},t;\kappa\tau)}{\Delta\tau} = \kappa\nabla^2\tilde{\psi}(\vec{x},t;\kappa\tau). \tag{2.59}$$

By setting a value $\sigma^2 = \kappa\tau_0$ of desired smearing and a number of smearing steps $n = \frac{\tau_0}{\Delta\tau}$, an expression for the smeared field in terms of the original field is given by

$$\tilde{\psi}(\vec{x},t;\sigma^2) = \left(\mathbb{I} + \frac{\sigma^2\nabla^2}{n}\right)^n \psi(\vec{x},t), \tag{2.60}$$

from where it is possible to identify the operator acting on the original quark field as the smearing function. The parameter σ^2 controls the width of the smeared quark field and should be chosen such that the field is smeared enough as to obtain a size comparable to the physical state of interest while not too much as to introduce significant finite-volume effects in the calculations. At this point it should be noted that for a gauge-covariant lattice formulation of this smearing it is necessary to use the gauge-covariant lattice 3D Laplacian operator $\nabla^2[t]$ which is given by

$$\nabla^2[t]_{\vec{x},\vec{y}} = -6\delta_{\vec{x},\vec{y}} + \sum_{k=1}^{3} U_k(\vec{x},t)\delta_{\vec{x}+\hat{k},y} + U_k^\dagger(\vec{x}-\hat{k},t)\delta_{\vec{x}-\hat{k},y}, \tag{2.61}$$

which is a hermitian negative-definite operator. As stated in [23, 76] the link variables used in Eqn. (2.61) should be appropriately smeared. Given this operator only acts on position and color space it is trivial in Dirac space and therefore any Dirac component of the original quark field can be written as a linear combination of the $3N_L^3$ eigenvectors $v_i[t]$ for a fixed time t as

$$\psi(\vec{x},t)_\alpha = \sum_{i=1}^{3N_L^3} c_i^\alpha v_i[t]_{\vec{x}}, \tag{2.62}$$

where $\alpha = 0, ..., 3$ is the Dirac component and c_i^α are the linear coefficients. Since in the limit of large n

$$\lim_{n\to\infty}\left(\mathbb{I} + \frac{\sigma^2\nabla^2[t]}{n}\right)^n = e^{\sigma^2\nabla^2[t]}, \tag{2.63}$$

the smeared field $\tilde{\psi}(\vec{x},t)_\alpha$ will exhibit an exponential suppression of the eigenvectors $v_i[t]$ with large negative eigenvalues. This indicates that eliminating the eigenvectors with high eigenvalues might serve as a good smearing strategy. Since these low modes correspond to long range contributions then it makes sense to keep them to determine properties like masses from the asymptotic behavior of correlation functions. The original distillation operator that acts on the quark fields is given by

$$\Box[t]_{\substack{\vec{x},\vec{y}\\ a,b\\ \alpha,\beta}} = \delta_{\alpha\beta}\sum_{i=1}^{N_v} v_i[t]_{\substack{\vec{x}\\ a}} v_i[t]^*_{\substack{\vec{y}\\ b}}, \tag{2.64}$$

which satisfies $\Box[t]^2 = \Box[t]$ however a more general one can be defined as

$$\tilde{\Box}[t]_{\substack{\vec{x},\vec{y}\\ a,b\\ \alpha,\beta}} = \delta_{\alpha\beta}\sum_{i=1}^{N_v} g(\lambda_i[t])\, v_i[t]_{\substack{\vec{x}\\ a}} v_i[t]^*_{\substack{\vec{y}\\ b}}, \tag{2.65}$$

where $g(\lambda_i[t])$, the quark distillation profile, is a function that can be freely chosen and N_v is the number of Laplacian eigenvectors that are kept when the eigenvalues are ordered from smallest to largest in magnitude [23]. This general distillation operator can be written in matrix form as

$$\tilde{\Box}[t] = V[t]J[t]V[t]^\dagger \otimes \mathbb{I}_S, \tag{2.66}$$

where $\mathbb{I}_S$ is the 4×4 identity, $V[t]$ has dimension $3N_L^3 \times N_v$ with the chosen Laplacian eigenvectors as columns and $J[t]$ is a $N_v \times N_v$ diagonal matrix with $g(\lambda)$ evaluated on each eigenvalue. The distilled quark fields are built by acting on the original quark fields with the distillation operator, yielding

$$\tilde{\psi}(\vec{x},t)_{\substack{\alpha\\ a}} = \sum_{i=1}^{N_v} g(\lambda_i[t])\, v_i[t]_{\substack{\vec{x}\\ a}} v_i[t]^*_{\substack{\vec{y}\\ b}} \psi(\vec{y},t)_{\substack{\alpha\\ b}}, \tag{2.67}$$

where Einstein's summation notation is used for repeated indices. The distilled quark field $\tilde{\psi}(\vec{x},t)$ will be used from now on for all calculations. These fields can be used to build a wide variety of operators for different kinds of particles however in this work only the ones corresponding to mesons will be of interest. Their use for building such operators will be explored in detail in Ch. 3. Distillation is a smearing technique which is not iterative and corresponds to a restriction of the quark fields to the span of the Laplacian eigenvectors chosen. These two features give rise to the advantages and disadvantages of this method which will be explored later. Nonetheless, two fundamental parts of it will be addressed here. First is the method for calculating the wanted eigenpairs relevant to build the distillation operators and second the method to numerically approximate a solution vector $x = D^{-1}b$ for a given vector b.

As mentioned before, $\nabla^2[t]$ as defined in Eqn. (2.61) is both hermitian and negative definite. Furthermore, when expressed in matrix form it has size $3N_L^3 \times 3N_L^3$ yet it is extremely sparse as it only involves local and nearest-neighbor interactions. These three features, together with the fact that only $N_v \ll 3N_L^3$ eigenpairs are needed, make the Lanczos algorithm the ideal tool to perform this calculation. First presented in [77] and explored in detail in [78, 79], the Lanczos algorithm is an iterative method to find extremal eigenvalues and corresponding eigenvectors of a hermitian matrix where it is not necessary to explicitly access all entries of the matrix but rather only its action on a vector. Details on its implementation and convergence can be found in [78–81]. The standard Lanczos algorithm is not free of complications: there is loss of orthogonality between the vectors it uses as basis for the subspace where the eigenvectors are approximated (explored in detail in [81–83]), the dependence of the convergence speed on how spread out the extremal eigenvalues are, memory limitations for the storage of the necessary vectors and finding an efficient algorithm to solve the resulting reduced tridiagonal problem. With these in mind, the algorithm of choice for this work is the Thick-Restart Lanczos [84, 85] with periodic reorthogonalization [86, 87] and Chebyshev acceleration [88] together with the method of Relatively Robust Representations [89–91] to solve the reduced eigenproblem, the latter being included in the Lapack library [92].

Finally, solving the linear system

$$Dx = b, \tag{2.68}$$

with D the Dirac operator defined in Eqn. (2.17) and b a given vector, from here on denoted as the right-hand side (RHS), is of major importance both in the HMC method and in distillation. For the latter case it will be shown in Ch. 3 that a total of $4 \times N_v \times N_t$ linear systems need to be solved per gauge configuration where the different RHS's are related to the eigenvectors of the 3D covariant Laplacian operator. For clarity the general form given in Eqn. (2.68) will be used for the current discussion, since most methods to approximate the solution vector $x = D^{-1}b$ can take as input any RHS b as long as the system is well-defined. Since D has size $12N_L^3N_t \times 12N_L^3N_t$ direct methods such as Gaussian elimination or LU-decomposition are not feasible and iterative methods are the preferred option. In such methods one builds a series of iterates $x^{(0)}, x^{(1)}, ...$, such that each new iterate is a better approximation to the true solution x of Eqn. (2.68). Since D is also a very sparse matrix, such that its action on a vector can be cheaply calculated, a family of iterative methods often used is the Krylov subspace methods [93, 94], which build each iterate $x^{(n)}$ from the Krylov subspace $\mathcal{K}_n(D, b)$ defined as

$$\mathcal{K}_n(D, r^{(0)}) = span\left(r^{(0)}, Dr^{(0)}, D^2r^{(0)}, ..., D^{n-1}r^{(0)}\right), \tag{2.69}$$

where $r^{(0)} = b - Dx^{(0)}$ is the residual corresponding to the initial guess $x^{(0)}$. Methods such as the Generalized Minimum Residual (GMRES) [95] and Generalized Conjugate Residual (GCR) [96] belong to this family and build the iterates $x^{(n)}$ such that the 2-norm of the residual at every iteration $r^{(n)} = b - Dx^{(n)}$ is minimized. There exist several improvements to these methods, such as preconditioning to replace the system with an equivalent yet better conditioned one [93, 94], and these often depend on the properties of the matrix D that defines the system. These improved variants can also be used together with multi-grid schemes, e.g. [97]. In this work the algorithm used to solve the linear systems, from now on denoted as the solver, corresponds to the deflated GCR together with the Schwarz alternating procedure (SAP) and even-odd (EO) preconditioning available in the openQCD library [98]. Details on SAP, EO preconditioning and the deflation used can be found in [99, 100] and these different building blocks are put together to define a two-grid multi-grid solver as explained in [97].

2.4 Ensembles

In this work a total of 4 different ensembles of gauge configurations are used. They correspond to three different models of QCD: $N_f = 2$, $N_f = 3 + 1$ and $N_f = 0$. The $N_f = 2$ ensembles are used as a simplified model to test the method developed in this work for the improvement of the distillation method while the $N_f = 3 + 1$ ensemble corresponds to a more physical setup, as will be explained shortly, and is used for a first approach to test the method for the measurement of quantities that can be compared to the physical world. Finally, the $N_f = 0$ ensemble is used to measure the glueball spectrum in absence of dynamical quarks to have a reference point to compare the corresponding spectrum in the presence of $N_f = 2$ dynamical quarks and the effect these have in terms of excited-state contamination. The details of the different cases are now presented separately.

2.4.1 $N_f = 2$

For the case of $N_f = 2$ there are two different ensembles labeled as Em1 (composed of 4080 gauge configurations) and Nm1 (composed of 480 gauge configurations). Both have periodic boundary conditions in all directions except for anti-periodic ones for the quark fields in time, are tuned such that the two degenerate quarks are at half the physical charm quark mass and come from the standard Wilson fermion action with a clover improvement term [37] and the Wilson plaquette gauge action. Em1 has a bare coupling $g_0^2 = \frac{6}{5.3}$, hopping parameter $\kappa = 0.13270$ and lattice size 48×24^3. These input parameters lead to a lattice spacing $a = 0.0658(10)$ fm [101, 102] and a flow scale [103] $\frac{t_0}{a^2} = 1.8486(7)$. Nm1 has a bare coupling $g_0^2 = \frac{6}{5.5}$, $\kappa = 0.13383$ and lattice size 96×48^3. These lead to a lattice spacing $a = 0.0486(6)$ [104, 105] and $\frac{t_0}{a^2} = 4.867(12)$. The main reason for using these two ensembles as testing ground for this work is the absence of light quarks. This simplifying feature makes the low-lying charmonia states stable since no decay into $D\bar{D}$ pairs can happen. Furthermore, the absence of iso-scalar mesons composed purely of light quarks guarantees that any possible mixing with glueball states is via the iso-scalar charmonium states. The latter isolates this mixing phenomenon and facilitates its study. Since one of the goals of this work is to develop a method to study this mixing then these two ensembles are a very convenient starting point. Furthermore, since the two ensembles have different physical volumes they allow the study of the volume scaling property of the distillation method and how the method proposed in this work performs in this regard. As a final remark, since the two degenerate charm quarks are still sufficiently heavy then the solution of the multiple linear systems involving the Dirac operator D is a feasible task for the two different numbers of configurations available.

2.4.2 $N_f = 0$

For the case of $N_f = 0$ the ensemble used in this work is labeled as qE, using a total of 9000 configurations. It has periodic boundary conditions in all directions and was generated using the Wilson plaquette gauge action. Its bare coupling is $g_0^2 = \frac{6}{5.85}$ and has a flow scale [103] $\frac{t_0}{a^2} = 1.844(3)$. The bare coupling was chosen such that $\frac{t_0}{a^2}$ matches the one from the Em1 ensemble.

2.4.3 $N_f = 3 + 1$

For the case of $N_f = 3 + 1$ the single ensemble studied in this work is labeled as B, using a total of 500 configurations. It has periodic boundary conditions except for Dirichlet (Schrödinger Functional) ones for the quark fields in the time direction and open boundary conditions for the link variables also in the time direction to avoid topological freezing [106]. The masses of the three degenerate light quarks are taken at the symmetric point such that their sum is as in nature and the mass of the charm quark is at its physical value. This ensemble was generated with an action involving the Wilson fermion action with a suitably chosen clover improvement and the Lüscher-Weisz action for the gauge field. The bare coupling is given by $g^2 = \frac{6}{3.43}$ and the hopping parameters from the light and charm quarks are $\kappa_l = 0.13599$ and $\kappa_c = 0.13088$ respectively. These parameters result in $a = 0.04292(52)$ fm and the flow scale $\frac{t_0}{a^2} = 11.573(36)$ [103]. Details of these actions and the tuning of the corresponding input parameters can be found in [107] and references therein. This ensemble is used for a number of reasons in this work. First of all, unlike ensembles Em1 and Nm1, it includes light quarks and contains a single charm quark at its physical mass. This brings the resulting charm physics close to the physical point, meaning that the corresponding results obtained can be compared with those from nature. Furthermore, choosing to work at the symmetric point for the light quark masses provides an additional improvement for masses coming from operators that do not contain valence light quarks. As shown in [107], the relationship between the physical mass $m_{\eta_c}^{\text{phys.}}$ of the η_c and the one measured in this ensemble $m_{\eta_c}^{\text{sym.}}$ is given by

$$m_{\eta_c}^{\text{phys.}} = m_{\eta_c}^{\text{sym.}} + \sum_{i=u,d,s} \frac{\partial m_{\eta_c}}{\partial m_i}|_{\text{sym.}} \left(m_i^{\text{phys.}} - m_i^{\text{sym.}} \right) + \mathcal{O}\left(\Delta m^2\right), \tag{2.70}$$

where the partial derivatives are evaluated at the symmetric point and therefore are equal to each other. The second term in Eqn. (2.70) becomes

$$\frac{\partial m_{\eta_c}}{\partial m_i}|_{\text{sym.}} \times \left(\sum_{i=u,d,s} \left(m_i^{\text{phys.}} - m_i^{\text{sym.}} \right) \right) \tag{2.71}$$

$$= \frac{\partial m_{\eta_c}}{\partial m_i}|_{\text{sym.}} \times \left(\sum_{i=u,d,s} m_i^{\text{phys.}} - \sum_{i=u,d,s} m_i^{\text{sym.}} \right) \tag{2.72}$$

$$= 0 \tag{2.73}$$

and therefore the leading correction term goes as the square of the mass differences. Finally, the inclusion of light quarks allows for decays and mixing that were not possible with ensembles Em1 and Nm1, such as the appearance of $D\bar{D}$ pairs and the mixing charmonia and light mesons via quark-anti-quark annihilation loops. The latter in particular leads to a more dense energy spectrum in the singlet sector and highlights one of the current obstacles that modern hadron spectroscopy in lattice QCD must overcome.

Chapter 3

Charmonium

> It is only slightly overstating the case to say that physics is the study of symmetry.
>
> Philip Anderson

This chapter focuses on the development of the optimal meson profile formalism within the distillation framework and its application to study flavor-neutral meson operators. First, the construction of these operators based on their transformation under the action of the cubic group together with parity and charge conjugation is briefly discussed. Afterwards the calculation of temporal correlation functions between these operators in the framework of distillation is explored and culminates in the introduction of optimal meson distillation profiles which is shown to yield an improvement over the standard distillation method. Implementation considerations that make all of the required calculations considerably efficient are also discussed. Finally the charmonium iso-vector spectrum results obtained using these profiles for a selected set of J^{PC} in ensembles Em1 and Nm1 are presented, based on which the advantages and limitations of the proposed method of optimal profiles are discussed.

3.1 Meson operators on the lattice

Meson operators can be built by gauge-invariantly combining quark fields. A generic flavor-neutral meson operator projected to zero spatial momentum can be defined as [1]

$$\mathcal{O}(t) = \sum_{\vec{x}\in\Lambda_{3D}} \sum_{\alpha,a} \bar{\psi}(\vec{x},t)_{\substack{\alpha\\a}} \sum_{\beta,\vec{y},b} \Gamma(\vec{x},\vec{y},t)_{\substack{\alpha\beta\\ab}} \psi(\vec{y},t)_{\substack{\beta\\b}}, \tag{3.1}$$

where Γ is an operator that can can depend on the gauge field U and act on spin, position and color space. This meson operator is associated with a meson annihilation operator in the corresponding Hilbert space. The one associated with a meson creation operator in this space is its hermitian conjugate, given by

$$\overline{\mathcal{O}}(t) = \sum_{\vec{x}\in\Lambda_{3D}} \sum_{\alpha,a} \bar{\psi}(\vec{x},t)_{\substack{\alpha\\a}} \sum_{\beta,\vec{y},b} \overline{\Gamma}(\vec{x},\vec{y},t)_{\substack{\alpha\beta\\ab}} \psi(\vec{y},t)_{\substack{\beta\\b}}, \tag{3.2}$$

where $\overline{\Gamma} = \gamma_0\Gamma^\dagger\gamma_0$. There is considerable freedom in the choice of the Γ operator and it is dictated by the J^{PC} quantum numbers of interest. Examples of Γ operators are the Dirac matrices, or products of them, such as γ_5, γ_i, $\gamma_5\gamma_i$, etc... or covariant

---

[1] Convention is chosen such that no division by N_L^3 is done in the spatial Fourier transform.

symmetric lattice derivatives ∇_i. These are ultimately chosen such that the resulting meson operator transforms as a given irrep R^{PC} of the cubic group O including parity and charge conjugation and can therefore be associated with a given total angular momentum J as dictated by Table 2.1. The simplest choice of only Dirac matrices leads to operators that transform according to A_1^{++}, A_1^{-+}, T_1^{--}, T_1^{++} and T_1^{+-} [25]. The list of accessible irreps can be extended by including covariant lattice derivatives, which are not local, in the sense that they involve the quark fields at different spatial points, and allow to sample more complex spatial structures that might better resemble physical states [23, 50, 108, 109] as well as to build operators which explicitly contain gluonic degrees of freedom and therefore are suitable to study spin-exotic states such as 1^{-+} not allowed in the quark model [45, 110, 111]. This extension is based on calculating the product of irreps $R_1 \otimes R_2$ generated by the Dirac matrices or lattice derivatives and decomposing it into a direct sum of irreps [43, 44, 112]. New operators involving both Dirac matrices and lattice derivatives can then be built by calculating the corresponding Clebsch-Gordan coefficients [113]. This procedure is well known in the literature: the decompositions of all products of irreps of the cubic group can be found in [40] and the explicit operators that transform according to all irreps containing up to two lattice derivatives can be found in [45, 114, 115] together with the J^{PC} to which they couple in the continuum limit. An alternative construction based on the continuum $SO(3)$ counterparts of the operators can also be found in [50].

For this work the irreps of interest are A_1^{++}, A_1^{-+}, T_1^{++}, T_1^{--}, T_1^{+-}, T_1^{-+}, E^{++} and T_2^{++}, which allow to access values of $J = 0, 1, 2$ with the corresponding PC numbers. The connection between the obtained spectrum results of each irrep and the different values of J^{PC} must be done carefully due to the subduction mentioned in Sect. 2.2.1. In principle one could count mass degeneracies across the different irreps when approaching the continuum limit and compare this result with the different subduction results in Table 2.1. With this strategy a degeneracy in the E^{++} and T_2^{++} could be identified with a 2^{++} state. The problem with such a method is that it requires a very high precision to avoid the appearance of near degeneracies that would lead to a wrong identification of the correct continuum quantum numbers. This is explained in [111] with the example of the χ_{c0} (0^{++}), χ_{c1} (1^{++}) and χ_{c2} (2^{++}) charmonium states whose mass is almost degenerate in nature [4]. Without sufficient precision to clearly distinguish the results from the A_1^{++}, T_1^{++}, E^{++} and T_2^{++} irreps then one might wrongly assign them to a single 4^{++} state. To avoid this problem an alternative method is presented in [50, 111] based on the overlaps $\langle 0| \hat{\mathcal{O}} |n\rangle$ between the created states and the actual energy eigenstates. By starting from meson operators that have a fixed J in the continuum and projecting them onto the different irreps of interest it can be shown that the overlaps obtained from the latter are related to the continuum J and therefore these operators "remember" from which J they were subduced. By following the procedure presented in [50, 111] one can explicitly build these overlaps that exhibit the same degeneracies across irreps as the masses for a fixed J and which can be used to assign the correct values of J to the resulting spectrum. As explained in [50] there are two main advantages to this technique over the counting of mass degeneracies: no approach to the continuum limit via calculations in ensembles at different lattice spacings is necessary and the near-degeneracies of the masses for some sets of values of J^{PC} do not lead to near-degeneracies in the overlaps that would require very high precision to disentangle.

A detailed identification of the continuum quantum numbers of the obtained spectrum is not the main goal of this work so whenever it is done it will be by counting mass degeneracies. As will be seen later on in the results, this approach provides sufficiently reliable results for the ground states of the irreps analyzed.

As a final consideration it is important to discuss how the different J^{PC} that can be analyzed are related to the quark model. In this framework the meson states are assumed to have the form $\bar{q}q$ with no explicit gluonic degrees of freedom. By fixing the total orbital angular momentum L and total spin S of the state the parity and charge conjugation symmetries are restricted to [5]

$$\begin{aligned} P &= (-1)^{L+1} \\ C &= (-1)^{L+S}. \end{aligned} \tag{3.3}$$

Since the quark and anti-quark have total spin $\frac{1}{2}$ the only possible values for S are 0 and 1. The choice $S = 0$, corresponding to the spin-singlet case, has $P \times C = -1$ and some examples are 0^{-+} for $L = 0$, 1^{+-} for $L = 1$, etc.. For $S = 1$, the spin-triplet case, one has $P \times C = 1$ and some examples are 1^{--} for $L = 0$, $(0, 1, 2)^{++}$ for $L = 1$, etc... A state with quantum numbers 1^{-+} is not allowed in this model and is therefore referred to as exotic [5]. Nonetheless such a state can be studied on the lattice and a possible way to account for its quantum numbers is to allow an additional gluonic degree of freedom with its own $J_g^{P_g C_g}$ apart from the quark degrees of freedom [110, 116]. If $J_g^{P_g C_g} = 1^{+-}$ then its combination with a $\bar{q}q$ state with 1^{--} can yield the wanted 1^{-+} state. This is the so-called hybrid interpretation of the state 1^{-+} since it mixes the $\bar{q}q$ one with a gluonic excitation and gives an indication that a suitable choice of meson operator to study this state in the lattice should explicitly contain a gluonic excitation in the form of the field-strength tensor $F_{\mu\nu}$. An example of such choice of hybrid operator is [45, 114]

$$\Gamma_i = \epsilon_{ijk}\gamma_j\mathbb{B}_k, \tag{3.4}$$

with $\mathbb{B}_i$ given by

$$\mathbb{B}_i = \epsilon_{ijk}\nabla_j\nabla_k. \tag{3.5}$$

In the continuum limit one has

$$\mathbb{B}_i = -\frac{i}{2}\epsilon_{ijk}F_{jk} \tag{3.6}$$

which explicitly contains the field-strength tensor. If the gauge field vanishes then this hybrid operator vanishes as well, which indicates its sensitivity to the gluonic degrees of freedom. A gluonic excitation carrying quantum numbers $J_g^{P_g C_g} = 1^{+-}$ combined with a 1^{--} state yields not only the 1^{-+} exotic state but also the non-exotic 0^{-+} and 2^{-+} states. This means that among the tower of excited states of these two channels one expects to find hybrid excitations. Again, the use of operators in these symmetry channels that explicitly involve the field-strength tensor would have the best overlap with these hybrid states. Examples of such operators can be found in [45, 114] while a table containing some hybrid supermultiplets of interest calculated via a gluonic excitation can be found in [110].

3.2 Meson correlation functions in the lattice using distillation

For the temporal correlations of mesons the quantity $\left[\mathcal{O}(t)\overline{\mathcal{O}}(0)\right]_F$ is given by

$$\left[\mathcal{O}(t)\overline{\mathcal{O}}(0)\right]_F = \frac{1}{Z_F[U]}\int d\psi d\bar{\psi} \sum_{\vec{x},\vec{y}\in\Lambda_{3D}} \bar{\psi}(\vec{x},t)\Gamma\psi(\vec{x},t)\bar{\psi}(\vec{y},0)\bar{\Gamma}\psi(\vec{y},0). \tag{3.7}$$

Since distilled quark fields will be used it is necessary to perform the replacement

$$\psi(\vec{x},t)_{\substack{\alpha\\ c}} \to \sum_{i=1}^{N_v} f(\lambda_i[t])v_i[t]_{\substack{\vec{x}\\ c}}v_i[t]^*_{\substack{\vec{n}\\ e}}\psi(\vec{n},t)_{\substack{\alpha\\ e}}, \tag{3.8}$$

before performing the Grassmann integration. This integration for the iso-vector case results in

$$\left[\mathcal{O}(t)\overline{\mathcal{O}}(0)\right]_F = -Tr\left(\Phi[t]\tau[t,0]\bar{\Phi}[0]\tau[0,t]\right), \tag{3.9}$$

and the temporal correlation of interest can be written as

$$C(t) = \langle -Tr\left(\Phi[t]\tau[t,0]\bar{\Phi}[0]\tau[0,t]\right)\rangle_U. \tag{3.10}$$

To define the elementals $\Phi[t]$, write the factorization $\Gamma = \mathcal{HD}$ where $\mathcal{H}$ acts only in Dirac space while $\mathcal{D}$ acts only in color and position space

$$\Phi[t]_{\substack{ij\\ \alpha\beta}} = \mathcal{H}_{\alpha\beta}g^*(\lambda_i[t])v_i[t]^\dagger\mathcal{D}v_j[t]g(\lambda_j[t]). \tag{3.11}$$

The perambulators are defined as

$$\tau[t,0]_{\substack{ij\\ \alpha\beta}} = v_i[t]^\dagger D^{-1}[t,0]_{\alpha\beta}v_j[0], \tag{3.12}$$

and just like the elementals they are matrices of size $4N_v \times 4N_v$. Three observations should be made about how they make distillation a very versatile technique. First, calculations of the elementals and perambulators are completely independent. Once all necessary perambulators are ready one can combine them with elementals coming from different choices of Γ so their calculation cost is fixed. Second, both the elementals and perambulators are relatively small matrices compared to the quark propagator D^{-1} which makes their calculation and storage feasible. Third, for different choices of $g(\lambda)$ it is not necessary to completely recalculate the elementals; it is enough to calculate them once with $g(\lambda) = 1$ and then multiply them by the desired choice of $g(\lambda)$ on the fly. However these advantages do not come for free and there is a notable disadvantage to distillation: the high number of inversions of D that must be performed to build the perambulators. For a fixed gauge configuration one needs to perform $4 \times N_t \times N_v$ inversions. On one hand, N_t can be around 48 or 92 for typical lattices. On the other hand, N_v scales with the physical volume of the lattice if one wants to keep a fixed threshold for the Laplacian eigenvalues in physical units and for larger lattices around 200 or more Laplacian eigenvectors are needed to avoid over-smearing. These two conditions can lead to a considerable number of inversions per gauge configuration ($\approx 73.6 \times 10^3$). Taking into account that one needs order thousands gauge configurations to get good statistical estimates of the correlation functions the total number of inversions easily enters the realm of millions.

To deal with this issue the method of stochastic distillation was first introduced in [117]. This method uses noise vectors in distillation space to stochastically estimate the correlation functions of interest without having to perform all $4 \times N_t \times N_v$ inversions but rather a smaller number that can then be kept approximately constant even when the lattice volume increases. However one must also be careful in controlling the error this stochastic estimation introduces and dilution schemes must be tuned. This method will not be discussed any further since this work focuses on the exact calculation of perambulators. This leaves the number of inversions unchanged yet seeks to answer a different question: are the available eigenvectors being used in the best way possible?

3.3 Optimizing the distillation operator for meson operators

The choice $g(\lambda) = 1$ is the most often used for studies that employ distillation [50, 110, 118, 119], with the exception of [50] where a Gaussian is also used. This keeps the distillation operator $\Box[t]$ as an orthogonal projector onto the space spanned by the Laplacian eigenvectors corresponding to small eigenvalues. The success of distillation indicates that this subspace is the right one, yet two issues arise:

- How to choose N_v to make sure no over-smearing is done by taking N_v too small while not incurring excessive computational work when N_v is too large?
- Is an orthogonal projector the best mapping to take the original quark fields into the distillation subspace?

The first one is related to the size of the perambulators and elementals while the second one is related to the matrix $J[t]$ and how each Laplacian eigenvector is used to build the distilled quark fields. Due to computational effort, trial and error is not a feasible method to estimate the optimal value of N_v and the physical volume scaling remains the preferred method to estimate it. However this scaling is independent of the operators being studied and it is not unreasonable to think that different operators might require more or less contributions from different Laplacian eigenvectors. In other words, it is not enough to find a value of N_v such that relevant information is not lost by over-smearing but one also needs to find a suitable choice of $g(\lambda)$ to make sure the operator resembles the physical state as much as possible. Since the physical state is probably different for different quantum numbers J^{PC} and their corresponding excitations then different choices of N_v and $g(\lambda)$ will probably be necessary to better approximate them.

The method to approach the issue of finding an appropriate N_v and exploit the freedom of choice of $g(\lambda)$ was first presented in [120] and the main idea will be outlined here. The building blocks of this approach are distilled quark fields based on N_B different quark distillation profiles $g_k(\lambda)$ with $k = 1, ..., N_B$. By choosing a Γ operator each distilled quark field can be used to build a meson operator $\mathcal{O}_k(t)$, appropriately projected to zero spatial momentum, which in turn give rise to different elementals defined as

$$\Phi^{(k)}[t] = J_k[t]^\dagger V[t]^\dagger \Gamma V[t] J_k[t]. \tag{3.13}$$

By using the factorization $\Gamma = \mathcal{H}\mathcal{D}[t]$, where $\mathcal{H}$ acts on spin indices and $\mathcal{D}[t]$ acts on color and spatial indices, the entries of these elementals are given as [2]

$$\begin{aligned}\underset{\alpha\beta}{\Phi^{(k)}_{ij}}[t] &= \mathcal{H}_{\alpha\beta} g_k(\lambda_i[t]) v_i[t]^\dagger \mathcal{D}[t] v_j[t] g_k(\lambda_j[t]) \\ &= \mathcal{H}_{\alpha\beta} v_i[t]^\dagger \mathcal{D}[t] v_j[t] f_k(\lambda_i[t], \lambda_j[t]), \qquad (3.14)\end{aligned}$$

where the meson distillation profile $f_k(\lambda_i[t], \lambda_j[t]) = g(\lambda_i[t])g(\lambda_j[t])$ has been defined. Note this profile is the only thing distinguishing these N_B different elementals and, compared to the explicit calculation of derivative-based operators that might be included in $\mathcal{D}[t]$, its inclusion is extremely cheap. The goal is to find a way to linearly combine the meson operators $\mathcal{O}_k(t)$ to obtain one which most resembles the physical state of interest. Such an operator will have the form

$$\tilde{\mathcal{O}}(t) = \sum_{k=1}^{N_B} a_k \mathcal{O}_k(t), \qquad (3.15)$$

where the linear coefficients a_k are yet to be determined. One could be tempted to build such an optimal operator to have the form

$$\tilde{\mathcal{O}}(t) = \bar{\psi}(t) V[t] \tilde{J}[t] V[t]^\dagger \Gamma V[t] \tilde{J}[t] V[t]^\dagger \psi(t) \qquad (3.16)$$

such that for a choice of Γ and energy level of the corresponding symmetry channel there is an optimal quark distillation profile contained in $\tilde{J}[t]$. However such a factorization is not always possible. This can be shown by explicitly writing down the elemental corresponding to the operator $\tilde{\mathcal{O}}(t)$ as

$$\begin{aligned}\underset{\alpha\beta}{\tilde{\Phi}_{ij}}[t] &= \sum_{k=1}^{N_B} a_k \underset{\alpha\beta}{\Phi^{(k)}_{ij}}[t] \\ &= \sum_{k=1}^{N_B} a_k \mathcal{H}_{\alpha\beta} v_i[t]^\dagger \mathcal{D}[t] v_j[t] f_k(\lambda_i[t], \lambda_j[t]) \\ &= v_i[t]^\dagger \mathcal{D}[t] v_j[t] \sum_{k=1}^{N_B} a_k f_k(\lambda_i[t], \lambda_j[t]) \\ &= v_i[t]^\dagger \mathcal{D}[t] v_j[t] \tilde{f}(\lambda_i[t], \lambda_j[t]), \qquad (3.17)\end{aligned}$$

where

$$\tilde{f}(\lambda_i[t], \lambda_j[t]) = \sum_{k=1}^{N_B} a_k f_k(\lambda_i[t], \lambda_j[t]) \qquad (3.18)$$

is the optimal meson profile. For a factorization as the one shown in Eqn. (3.16) to exist then it must be possible to write

$$\tilde{f}(\lambda_i[t], \lambda_j[t]) = g(\lambda_i[t])g(\lambda_j[t]), \qquad (3.19)$$

and for $N_B > 1$ such a factorization is in general not possible. Furthermore, even if it were possible to factorize $\tilde{f}(\lambda_i[t], \lambda_j[t])$ in the form

$$\tilde{f}(\lambda_i[t], \lambda_j[t]) = g_1(\lambda_i[t])g_2(\lambda_j[t]), \qquad (3.20)$$

---

[2] The profiles $g_k(\lambda)$ are assumed to be real so $g^*(\lambda) = g(\lambda)$.

the case where $\tilde{f}(\lambda_i[t], \lambda_j[t])$ changes sign for some $\lambda_i[t] = \lambda_j[t]$ would necessarily mean that $g_1(\lambda_i[t]) \neq g_2(\lambda_i[t])$ and therefore the wanted factorization is impossible. Such change of sign is possible and dictated by the coefficients a_k. These considerations are an indication that it is necessary to remain at "meson level" when working with optimal distillation profiles. This means that instead of aiming at a construction as the one shown in Eqn. (3.16) one must work with one given by

$$\tilde{\mathcal{O}}(t) = \bar{\psi}(t) V[t] \tilde{\Phi}[t] V[t]^{\dagger} \psi(t), \tag{3.21}$$

where, rather than assigning an individual quark distillation profile to the ψ and $\bar{\psi}$ fields separately, the optimal meson distillation profile cannot be decoupled and affects both fields. One can go a step further and write the operator as

$$\tilde{\mathcal{O}}(t) = \bar{\psi}(t) \tilde{\Gamma}[t] \psi(t), \tag{3.22}$$

where

$$\tilde{\Gamma}[t] = V[t] \tilde{\Phi}[t] V[t]^{\dagger}, \tag{3.23}$$

can be considered as an optimal Γ operator which includes the original Γ plus the action of the optimal meson distillation profile and therefore is not restricted to a quark-level smearing. This construction leads to a further feature of the proposed method. The $\tilde{\Gamma}[t]$ operator acts on spin, position and color indices and one can be interested in particular in its spatial behavior. A first step to access this property is to find a way to "integrate out" the spin indices. As proposed in [120], this can be done for the spin-singlet J^{PC} for different values of angular momentum by calculating the spin-projected operator as

$$\tilde{\Gamma}_S[t] = Tr\left(\gamma_5 \tilde{\Gamma}[t]\right), \tag{3.24}$$

where the trace is taken over spin indices and spin-singlet S- and P-wave operators subjected to this spin-projection are chosen to have only a γ_5 in their definition for setting the spin structure, i.e $\Gamma = \gamma_5$ for 0^{-+} and $\Gamma = \gamma_5 \nabla_i$ for 1^{+-}. The second step is to define a 3D point-like vector

$$\phi_{\substack{\vec{x} \\ c}} = h_0 \delta_{\vec{x},\vec{z}}, \tag{3.25}$$

where $h_0 \in \mathbb{C}^3$ with $||h_0||_2 = 1$ and $\vec{z}$ an arbitrary fixed position $\vec{z}$, such that $\tilde{\Gamma}_S[t]$ can act on it and the spatial profile of the resulting 3D vector can be used to visualize the spatial smearing effect of $\tilde{\Gamma}_S[t]$. With the resulting vector for each value of time t given as

$$\tilde{\phi}^{(\Gamma,e)}[t]_{\substack{\vec{x} \\ b}} = \sum_{\vec{y},c} \tilde{\Gamma}_S[t]_{\substack{\vec{x}\vec{y} \\ bc}} \phi_{\substack{\vec{y} \\ c}}, \tag{3.26}$$

the spatial profile of the created state can be defined as

$$\Psi^{(\Gamma,0)}(\vec{x}) = \frac{1}{N_t} \sum_{t=0}^{N_t-1} ||\tilde{\phi}^{(\Gamma,e)}[t]||_2^2, \tag{3.27}$$

where the 2-norm $|| \cdot ||_2$ is taken over color space only. A similar construction of spatial wave functions based on Wuppertal smearing was presented in [121].

Finally one needs to calculate the coefficients a_k and this is done via the previously explained GEVP formulation. The relevant correlation matrix is given by

$$C_{ij}(t) = \langle \mathcal{O}_i(t)\bar{\mathcal{O}}_j(0)\rangle = \left\langle -Tr\left(\Phi^{(i)}[t]\tau[t,0]\bar{\Phi}^{(j)}[0]\tau[0,t]\right)\right\rangle_U, \tag{3.28}$$

for the iso-vector case. As shown in Sect. 2.2.3 the generalized eigenvectors together with the pruning vectors grant access to the coefficients a_k for a fixed Γ and energy level of interest. As will be seen in the results presented later on, not only do different choices of Γ yield different optimal meson distillation profiles but also different energy levels for a single choice of Γ have different optimal meson distillation profiles. This variety of profiles is an added advantage of the method since it allows to tailor the optimal elemental to better approximate the state of interest. The method can also be extended to the case where the GEVP includes not only different choices of quark distillation profiles but also different choices of Γ operators with the same quantum numbers. Considering N_Γ Γ operators and N_P quark distillation profiles the elemental corresponding to the m-th Γ structure and the n-th quark profile is given by

$$\Phi^{(m,n)}_{\substack{ij\\ \alpha\beta}}[t] = \mathcal{H}^m_{\alpha\beta} v_i[t]^\dagger \mathcal{D}^m[t] v_j[t] f_n(\lambda_i[t],\lambda_j[t]) \tag{3.29}$$

such that the resulting optimal elemental is given by

$$\begin{aligned}\tilde{\Phi}_{\substack{ij\\ \alpha\beta}}[t] &= \sum_{m,n} a_{mn}\Phi^{(m,n)}_{\substack{ij\\ \alpha\beta}}[t]\\ &= \sum_{m,n} a_{mn}\mathcal{H}^m_{\alpha\beta} v_i[t]^\dagger \mathcal{D}^m[t] v_j[t] f_n(\lambda_i[t],\lambda_j[t])\\ &= \sum_{m} \mathcal{H}^m_{\alpha\beta} v_i[t]^\dagger \mathcal{D}^m[t] v_j[t] \sum_n a_{mn} f_n(\lambda_i[t],\lambda_j[t])\\ &= \sum_{m} \mathcal{H}^m_{\alpha\beta} v_i[t]^\dagger \mathcal{D}^m[t] v_j[t] \tilde{f}^{(m)}(\lambda_i[t],\lambda_j[t]),\end{aligned} \tag{3.30}$$

where

$$\tilde{f}^{(m)}(\lambda_i[t],\lambda_j[t]) = \sum_n a_{mn} f_n(\lambda_i[t],\lambda_j[t]), \tag{3.31}$$

is the optimal meson profile associated with the m-th Γ operator. The inclusion of multiple Γ operators further expands the basis for the GEVP formulation and is expected to improve on the results obtained when a single Γ operator is used. Note the coefficients a_{mn} that here would be determined from a GEVP starting from the $N_\Gamma N_P \times N_\Gamma N_P$ temporal correlation matrix are not expected to coincide with those from solving N_Γ different GEVPs each one starting with an $N_P \times N_P$ correlation matrix. This is due to the fact that the former considers the mixing between the different Γ operators and their profiles while the latter only considers the mixing among different profiles for a fixed Γ structure. For this reason it would also be preferable to solve the GEVP from the $N_\Gamma N_P \times N_\Gamma N_P$ correlation matrix to build the corresponding optimal elemental instead of solving N_Γ different GEVPs of size $N_P \times N_P$ to build N_Γ optimal elementals that could then be used to formulate an $N_\Gamma \times N_\Gamma$ GEVP.

A final remark to keep in mind is that the optimal profiles can be built and used in more general cases than the one presented in this work. The spectrum of flavored mesons can be studied with this method, where the difference in masses of the flavors used can lead to using a different value of N_v for each flavor. This would be mainly motivated by the higher computational effort involved in the solution of linear systems involving the D operator with light quark mass. In this situation the resulting elementals would be rectangular matrices yet the introduction of the quark profiles and construction of the optimal profiles via a GEVP can be done as presented in this work. The case with non-zero spatial momentum can also be studied in this formalism; a non-trivial complex exponential that fixes the momentum of the meson must be introduced in the elemental calculation however the introduction and optimization of the profiles remain unchanged. The formalism can also be extended to baryon operators, where the elementals will have three distillation indices and therefore a product of three quark distillation profiles defines the basic baryon profile. The applicability to these examples also holds within the framework of stochastic distillation; since the elementals and perambulators are independent from each other, the profiles can be introduced no matter if the perambulator is calculated exactly or stochastically. The latter way of calculation the perambulators introduces an additional error to the correlation functions via which the profiles are optimized, however a careful tuning of the relevant parameters allows to keep said error under control. The extension to the study of static potentials is also possible and was first presented in [122], where the optimal profiles are built to improve so-called Laplace trial states that represent a static color-anti-color source pair from whose temporal correlation function one can measure the static potential. As mentioned in this same reference, this strategy can also be extended to the study of static-light mesons.

3.4 Charmonium spectrum using the optimal meson distillation profiles

Now that the theoretical foundations of the method for building optimal meson distillation profiles have been presented it is possible to test the method and observe the improvements it brings to the distillation framework. However it is important to first discuss technical details regarding how each of the different steps of the calculations are performed. There a total of four steps which must always be performed sequentially:

1. Calculate the N_v lowest eigenvalues and eigenvectors for each value of t.

2. Calculate the elementals for the different choices of Γ of interest, which involves an explicit calculation only if Γ is a derivative based operator.

3. Calculate the perambulators $\tau[t_1, t_2]$ for all time pairs (t_1, t_2).

4. Calculate the correlation functions of interest which involve products of the appropriate elementals and perambulators.

Each step might seem straightforward yet there are several details to be considered to make sure calculations are done in an efficient manner. All calculations apart from the data analysis are performed using the *qcdlib* library, written by Dr. Tomasz Korzec and based on C and MPI.

3.4.1 Eigenpair calculation

The Thick-Restart Lanczos with Chebyshev acceleration and periodic reorthogonalization used in this work relies on different input parameters that must be tuned. Not only this, but its implementation for the case of the 3D covariant Laplacian operator as defined in Eqn. (2.61) must be done carefully as to guarantee efficiency. This is done by exploiting different properties of this operator and will be briefly explained here. The different input parameters for the calculation of the desired eigenvectors and eigenvalues can be separated into two categories: those of the Chebyshev acceleration and those of the Thick-Restart method including the periodic reorthogonalization. For the Chebyshev acceleration one defines a re-scaled Chebyshev polynomial of the form

$$P_n(x) = \gamma T_n(\alpha x + \beta), \tag{3.32}$$

where $T_n(x)$ is the Chebyshev polynomial of type 1 with degree n. These $T_n(x)$ are bounded by $[-1, 1]$ when $x \in [-1, 1]$ and the choice of coefficients α, β and γ is made such that $P_n(x)$ is bounded when $x \in [a, b]$ where the interval $[a, b]$ must contain all unwanted eigenvalues of $-\nabla^2[t]$ larger than a. Demanding $P_n(0) = 1$, $P_n(b) = \gamma T_n(1)$ and $P_n(a) = \gamma T_n(-1)$ the following definitions are obtained:

$$\begin{aligned} \alpha &= \frac{2}{b-a} \\ \beta &= 1 - \frac{2}{1-\frac{a}{b}} \\ \gamma &= \frac{1}{T_n(\beta)}, \end{aligned} \tag{3.33}$$

where the normalization is chosen such that $P_n(x)$ is positive and decreasing in the interval $[0, a]$. With these coefficients all eigenvalues $\lambda_i[t]$ of $-\nabla^2[t]$ smaller than a get mapped to $P_n(\lambda_i[t])$ and become more spread out without allowing for ambiguities due to unwanted eigenvalues being mapped outside of the range $[-1, 1]$. This means that the operator $P_n(-\nabla^2[t])$ will exhibit better convergence when used in the Lanczos algorithm. For a total of N_v eigenpairs it is not known a priori what the corresponding eigenvalues will be in order to choose the values of a and b. To find suitable values for these parameters it is useful to note that if all link variables are set to the unit matrix then $\nabla^2[t]$ becomes the free 3D Laplacian operator with an additional degree of freedom due to the color index. The spectrum of this free operator is known to be contained in the interval $[0, 12]$ in lattice units and the introduction of non-trivial link variables leads to perturbations of this spectrum that are nonetheless not significantly large. This means that a good choice for the value of b is a value sufficiently above 12. Numerical experiments with a small 8×4^3 lattice revealed that a value of $b = 15$ is appropriate. No unwanted eigenvalues from the upper side of the spectrum appeared in the calculation performed in the ensembles used in this work which means that this choice of b works well for the values of N_v considered. To find a suitable value of a one can choose a sufficiently large initial guess and look at the total number of eigenpairs that converge to the desired precision. As long as this number is larger than N_v the choice of a is acceptable and $a = 4$ was found to work well for all calculations in this work where $N_{APE} = 20$ APE smearing iterations using $\alpha_{APE} = 0.5$ were used for ensemble Em1 and same α_{APE} but $N_{APE} = 40$ for Nm1 to take into account the larger 3D volume. These parameters were tuned in a separate study of ensemble Em1[3]. A final consideration regarding the polynomial $P_n(x)$ is the choice of the degree n. Large values of n require several applications of $\nabla^2[t]$ and therefore can lead to a significant increase in the overall computational cost. Furthermore, on a more technical note, since the polynomials $T_n(x)$ are defined via a recursion relation then its implementation can lead to stack-expensive functions for deep recursions at large n. To counter this technical issue the function that defines the recursion is written in a tail-recursive manner [123]. This only leaves open the issue of the computational cost and the choice $n = 8$ was found to work well in terms of balancing cost and convergence for the ensembles used in this work.

For the Thick-Restart algorithm the input parameters are the size of the restart subspace, the maximum number of restarts, the thickness in each restart, the wanted residual threshold and the threshold for the periodic reorthogonalization procedure. The choice for the size of the restart subspace is based on the general rule of thumb for the Lanczos algorithm to use $\sim 3N_v$ or $\sim 4N_v$ vectors to allow N_v Ritz vectors to converge to the desired precision. The thickness of the restart as defined in [84, 85]is chosen as a function of N_v and the total number of converged Ritz vectors per restart as recommended in the references. The maximum number of restarts is chosen as 30 throughout this work. Since in all cases a single run of the algorithm was enough to obtain the wanted N_v vectors, no further tuning is required for the thickness or the maximum number of restarts. The residual threshold is chosen as 10^{-8} which reduces the computational work required to achieve convergence. This is in principle allowed since using a strict threshold would mean the obtained vectors are closer to the actual eigenvectors there is no reason to believe vectors which slightly deviate from them would damage the properties of the distillation operator. Finally, the threshold for the periodic reorthogonalization method is set to 10^{-10}. This value is safer than the $\sim 10^{-8}$ one that has been argued to already be a sufficiently good choice [86, 87, 124]. A very similar algorithm for the calculation of the eigenvalues and eigenvectors of $\nabla^2[t]$ was used in [117] with a very similar set of parameters which indicates they are suitable for this calculation. As a final note, an important property of the 3D covariant Laplacian operator is it is block-diagonal in time. This means that $\nabla^2[t_1]$ and $\nabla^2[t_2]$, together with their corresponding eigenvalues and eigenvectors, can be computed independently. This leads to a trivial parallelization in time so eigenvalues and eigenvectors of the operator at different times can be calculated and written to disk simultaneously. This is done in the framework of MPI which the library qcdlib uses such that there is parallelization along the 3 spatial dimensions and also the temporal one.

3.4.2 Elemental calculation

The elementals are a fundamental building block for the distillation framework. These matrices only require explicit calculations when the operator Γ is not trivial in position/color space. The only cases of this kind in this work are those with one or two covariant 3D derivatives. Just like the 3D covariant Laplacian $\nabla^2[t]$ each of the three spatial derivatives $\nabla_i[t]$ act only on 3D spinor components for a given value of time t. The same trivial parallelization in time used for the Lanczos algorithm can be used to calculate the elementals of different times simultaneously. Considering up to two derivatives there is a total of 12 different elementals of size $N_v \times N_v$ that must

---

[3] Special thanks to Roman Höllwieser for help with this tuning of parameters.

in principle be calculated per value of t: 3 for the single derivative case and 9 for the two derivative case. However it is possible to get away with fewer calculations. Single derivative elementals can be written as anti-hermitian matrices

$$\Phi^{(k)}_{ij}[t] = v_i[t]^\dagger \nabla_k[t] v_j[t]. \tag{3.34}$$

This means that one only needs to calculate and store the $\frac{1}{2}N_v(N_v+1)$ entries of the upper or lower triangular section of $\Phi^{(k)}[t]$ and the remaining ones can be calculated when needed. This reduces by roughly half the number of inner products required. Double derivative elementals can be written as

$$\Phi^{(k,l)}_{ij}[t] = v_i[t]^\dagger \nabla_k[t] \nabla_l[t] v_j[t] \tag{3.35}$$

and are hermitian with respect to all indices including the directions of the derivatives, i.e $\left(\Phi^{(k,l)}[t]\right)^\dagger = \Phi^{(l,k)}[t]$. The covariant derivatives $\nabla_i[t]$ do not commute for different directions in the presence of a non-trivial gauge field so all N_v^2 entries of a fixed combination of directions (k,l) must be calculated however once these are known, the entries of the elemental corresponding to combination (l,k) can be obtained. This reduces the number of required elemental calculations from 12 to 9. Furthermore, thanks to the anti-hermiticity of the 3 corresponding to the single derivatives and the hermiticity of the 3 double derivative ones with repeated direction indices, 6 of these 9 elementals only require approximately half of their entries to be explicitly calculated and stored.

3.4.3 Perambulator calculation

Just as the elementals, the perambulators are a fundamental building block of the distillation framework and their calculation is the main computational cost of this framework. For a fixed pair (t_1,t_2) the $4N_v \times 4N_v$ perambulator matrix is given by

$$\tau[t_1,t_2]_{\substack{ij\\ \alpha\beta}} = v_{i,\alpha}[t_1]^\dagger D^{-1} v_{j,\beta}[t_2], \tag{3.36}$$

so one needs to perform $4N_v$ inversions and $16N_v^2$ inner products involving spinors with time, position, color and spin indices. However the cost related to the inner products can be straightforwardly reduced by noting $v_{i,\alpha}[t]$ is non-zero only in time index t_1 and spin index α where it is equal to the 3D vector $v_i[t_1]$ which means that one only needs to calculate the 3D inner product between $v_i[t_1]$ and the 3D component of $D^{-1}v_{j,\beta}[t_2]$ in time index t_1 and spin index α. Furthermore, since these 3D inner products are independent when different values of time indices are used, one can use the same trivial parallelization in time used for the Lanczos algorithm and elemental calculation. Once the vector $D^{-1}v_{j,\beta}[t_2]$ has been built different inner products corresponding to Laplacian eigenvectors of different times can be calculated simultaneously to build the entries of the perambulator $\tau[t_1,t_2]$ for all relevant values of t_1 and save them to files. Doing so for all pairs (t_1,t_2) can lead to considerable storage cost which can be reduced roughly by half by noting that the perambulators inherit the γ_5-hermiticity from D^{-1}. This γ_5-hermiticity means that only $\frac{1}{2}N_t(N_t+1)$ perambulators must be calculated and stored.

One final consideration is related to the way the perambulator calculations are organized. As mentioned before, the cost is divided between the inversions required and the corresponding inner products. The former have an approximately fixed cost which depends on the solver used while the latter can be done in an efficient manner by organizing the calculation as follows. One needs to solve the linear system

$$Dx^{(i,\alpha,t)} = v_{i,\alpha}[t], \tag{3.37}$$

for $i = 1, ..., N_v$, $\alpha = 0, ..., 3$ and $t = 0, ..., N_t - 1$. To avoid repeating the calculation of the different solution vectors $x^{(i,\alpha,t)}$ one can calculate all entries of the perambulator that involve $x^{(i,\alpha,t)}$ via the corresponding inner products, i.e

$$\begin{aligned} \tau[t_1, t]_{\substack{ij \\ \beta\alpha}} &= v_{j,\beta}[t_1]^\dagger D^{-1} v_{i,\alpha}[t] \\ &= v_{j,\beta}[t_1]^\dagger x^{(i,\alpha,t)} \end{aligned} \tag{3.38}$$

for all $j = 1, ..., N_v$, $\beta = 0, ..., 3$ and $t_1 = 0, ..., N_t - 1$. Given the large number of inner products required it is convenient to not perform the communication to calculate $\tau[t_1, t]_{\substack{ij \\ \beta\alpha}}$ but only have each MPI process calculate its local part of the inner product as

$$\tau^{(\mathrm{loc})}[t_1, t]_{\substack{ij \\ \beta\alpha}} = \sum_{\vec{x} \in \Lambda_{3D}^{loc}} \sum_{a=1}^{3} v_{j,\beta}[t_1]^*_{\substack{\vec{x} \\ a}} x^{(i,\alpha,t)}_{\substack{\vec{x} \\ a}}, \tag{3.39}$$

where Λ_{3D}^{loc} is the local 3D lattice contained in the MPI process. All $16N_v^2$ entries of each local perambulator for a fixed t and $t_1 = 0, ..., N_t - 1$ are calculated without communication except for the one involved in the solver. Once all local perambulators $\tau^{\mathrm{loc}}[t_1, t]$ for the fixed t and all t_1 are ready one can start a non-blocking communication routine to calculate the corresponding perambulators $\tau[t_1, t]$. Immediately after, the calculation for the next set of local perambulators $\tau^{\mathrm{loc}}[t_1, t + 1]$ can begin. Since this new calculation will involve the solution of $4N_v$ inversions and the corresponding local inner products, the communication required to build $\tau[t_1, t]$ can be hidden behind these calculations [4].

3.4.4 Correlation calculation

Two-point temporal correlation functions calculated in the distillation framework are traces of products involving elementals and perambulators. From Eqn. (3.10) it follows the relevant traces correspond to

$$A(t_1, t_2) = Tr\left(\Phi[t_1]\tau[t_1, t_2]\bar{\Phi}[t_2]\tau[t_2, t_1]\right), \tag{3.40}$$

and

$$B(t) = Tr\left(\Phi[t]\tau[t, t]\right). \tag{3.41}$$

It is clear for a fixed pair (t_1, t_2) the trace $A(t_1, t_2)$ only depends on the elementals and perambulators of these times just as $B(t)$ only depends on the ones at time t. This means that for two distinct pairs (t_1, t_2) and (t_3, t_4) the traces $A(t_1, t_2)$ and $A(t_3, t_4)$ can be calculated simultaneously, just as the traces $B(t_1)$ and $B(t_2)$ can be calculated separately for $t_1 \neq t_2$. The final step is the averaging of the correlation

---

[4] Special thanks to Gustavo Ramirez for this observation.

function for all available time sources given a fixed time separation t to exploit translation invariance in time. Once the $A(t_1, t_2)$ is known for all values of t_1, t_2 then the correlation function $C(t)$ is calculated as

$$C(t) = \frac{1}{N_t} \sum_{s=0}^{N_t-1} A(as+t, as), \tag{3.42}$$

and a similar calculation follows for the disconnected contribution. This averaging over the entire temporal extent of the lattice is only valid when periodic boundary conditions in time are used for the link variables, as with the Em1 and Nm1 ensembles. The case with open boundary conditions for ensemble B, which is explained in Chapter 6, relies on translation invariance in a time interval sufficiently far away from the temporal boundaries. As a final note, the elementals are sparse in the spin indices since these only involve Dirac matrices. This sparsity can be exploited when performing contractions over these indices in the products between elementals and perambulators. The pattern of sparsity depends on the choice of Γ operator however it is always possible to set up the matrix-matrix multiplication to avoid unnecessary operations that would result in just adding up zeros.

3.4.5 Iso-vector spectrum results in $N_f = 2$

The method presented in Section 3.3 is now applied to study different channels of symmetry J^{PC} in the iso-vector case, without the disconnected contribution. The first step is to choose which J^{PC} are of interest and the corresponding Γ operators that can be used to access them. Table 3.1 displays those studied in this work. The local operators are taken from [25] and the derivative-based ones are taken from [111]. Local operators are used in all channels where possible due to their ease of computation. Derivative-based operators are used to access a wider range of J^{PC} such as the 2^{++} and 1^{-+} and also to sample more complex spatial structure and dependence on link variables. All local and derivative-based Γ operators used in this work are displayed in Table 3.1, where the local ones are taken from [25] and the derivative-based ones from [111, 114]. The Clebsch-Gordan coefficients $\mathcal{Q}_{ijk}$ can be found in [111, 114] for the E component from the decomposition of the $T_1 \otimes T_1$ representation. They are used to build a basis of E^{++} from the operators γ_i and ∇_i for the 2^{++} channel, where the subduction yields the direct sum $E^{++} \oplus T_2^{++}$. The T_2^{++} basis is given by the $|\epsilon_{ijk}|\gamma_j \nabla_k$. For all operators in irreps with dimension larger than 1 only one of the components is used, e.g γ_1 from the three-dimensional γ_i.

J^{PC}	Γ	Particle
0^{-+}	γ_5 $\gamma_0\gamma_5\gamma_i\nabla_i$ $\gamma_i\mathbb{B}_i$	η_c
1^{--}	γ_i ∇_i $\gamma_5\mathbb{B}_i$	J/Ψ
0^{++}	$\mathbb{I}$ $\gamma_i\nabla_i$	χ_{c0}
1^{++}	$\gamma_5\gamma_i$ $\epsilon_{ijk}\gamma_j\nabla_k$	χ_{c1}
1^{+-}	$\epsilon_{ijk}\gamma_j\gamma_k$ $\gamma_5\nabla_i$	h_c
2^{++}	$\lvert\epsilon_{ijk}\rvert\gamma_j\nabla_k$ $\mathbb{Q}_{ijk}\gamma_j\nabla_k$	χ_{c2}
1^{-+}	$\epsilon_{ijk}\gamma_j\mathbb{B}_k$ $\gamma_0\nabla_i$	...

TABLE 3.1: Quantum numbers J^{PC} together with the Γ operators used and the corresponding name of the particle in nature.

There is freedom in the choice of basis for the quark profiles, both in the number of profiles and how each one is defined yet there are also guiding criteria that help narrow it down. First, distillation is based on the intuition that low eigenmodes of the 3D covariant Laplacian provide the largest contributions for hadron spectroscopy since they correspond to low-energy modes. It makes sense to consider quark profiles which give more importance to the low eigenvalues compared to the higher available ones. Furthermore, since the threshold where remaining eigenvalues give sufficiently small contributions is not known a priori, the different profiles should allow for different degrees of suppression of the higher eigenvalues. It is expected the resulting optimal meson profile will show precisely where this threshold is. Finally, one can in principle find an arbitrarily large number of functions which satisfy these conditions yet that does not mean one should use a basis that is too big. If the chosen profiles do not lead to sufficiently different, or more specifically linearly independent, meson operators, the resulting correlation matrix in the GEVP can be ill-conditioned and make the problem numerically unstable. Based on these considerations the choice for this work is a total of 7 different Gaussian profiles with different widths defined as

$$g_k(\lambda) = e^{-\frac{\lambda^2}{2\sigma_k^2}}, \tag{3.43}$$

where the widths σ_k are chosen to allow for a wide range of suppression levels in the interval of the eigenvalues. For ensemble Em1 a total of $N_v = 200$ eigenvectors and eigenvalues are calculated and Fig. 3.1 shows the average over all 4080 gauge configurations of the three largest and smallest ones. The corresponding errors are very small compared to the values so there is no crossing or ambiguities between successive eigenvalues. The eigenvalues of the Nm1 ensemble display the same features. Based on these values the widths σ_k of the Gaussian profiles are chosen equally spaced between $\sigma_1 = 0.05$ and $\sigma_7 = 0.28666667$ so there is enhancement or suppression over the whole range of eigenvalues. It is very important to note the 3D covariant Laplacian defined in Eqn. (2.61) assumes that distance is measured in units of the lattice spacing a and therefore this quantity is not explicitly included. This means the obtained eigenvalues are given as λa^2, consistent with the fact that the physical eigenvalues have units of inverse distance squared in natural units. The distinction between lattice and physical eigenvalues is not of immediate importance for this work and the simplified notation λ will be used. The resulting quark profiles from the chosen values of σ_k can be seen in Fig. 3.2, where the minimum and maximum eigenvalues found in the analyzed configurations are marked by the dashed lines. As wanted, the different Gaussian profiles cover a wide range of suppressions of the eigenvalues. Since ensemble Nm1 has a different 3D lattice volume and lattice spacing, the number of Laplacian eigenvectors required for the same level of smearing as the Em1 case can be calculated via the 3D volume scaling rule as

$$N_v = 200\frac{(48 \times 0.049)^3}{(24 \times 0.0658)^3} \approx 660. \tag{3.44}$$

This calculation shows one would need to roughly triple the number of eigenvectors used with respect to Em1, however this value of N_v would lead to computational and storage costs that are not available for this work. To avoid such costs but still use more vectors than in Em1, the value $N_v = 325$ is used for this ensemble which roughly corresponds to 100 in Em1 and the corresponding widths for the Gaussian profiles are scaled with the squared ratio of the lattice spacings of both ensembles.

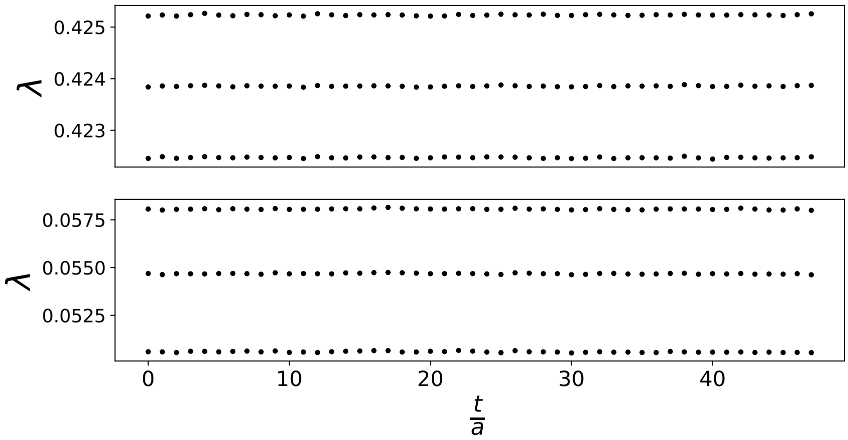

FIGURE 3.1: Three smallest and largest eigenvalues of the 3D covariant Laplacian as a function of time calculated in ensemble Em1.

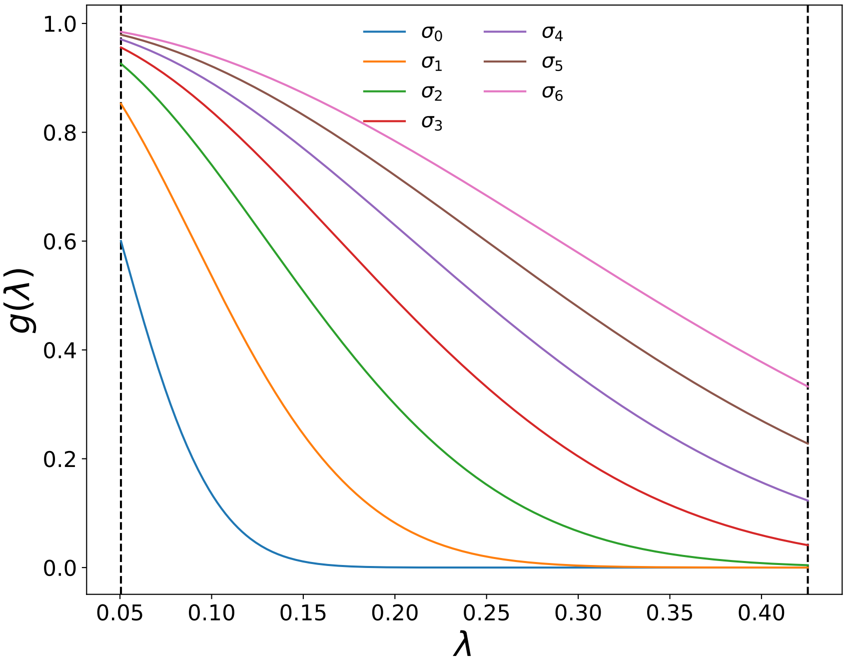

FIGURE 3.2: Quark smearing profiles used for the Em1 ensemble as a function of the Laplacian eigenvalues. Dashed lines mark the minimum and maximum eigenvalues over all the analyzed configurations.

3.4.5.1 Local Γ operators

For the sake of clarity the different steps of the calculation with $\Gamma = \gamma_5$ will be explicitly presented here for the Em1 ensemble and all other Γ operators, both local and derivative-based for both ensembles, will be analyzed in the same manner. The first step is the construction of the correlation matrix and its subsequent pruning as explained in Section 2.2.3. One should choose a pruning time t_s where the correlation matrix is dominated by the states of interest and then extract the singular vectors corresponding to the largest singular values at that time. An important detail is the correlation matrix is symmetric and positive definite, the latter up to statistical fluctuations which can become significant at large values of time. This means with large enough statistics and at not too large values of time the singular value decomposition of the correlation matrix is equivalent to its eigendecomposition. With this in mind it is possible to devise a strategy to determine a suitable value of t_s. As shown in [47], the correlation matrix $C(t)$ can be sufficiently well approximated by

$$C^0(t)_{ij} = \sum_{n=1}^{N_B} \langle\Omega|\,\hat{\mathcal{O}}_i\,|n\rangle\,\langle n|\,\hat{\mathcal{O}}_j^\dagger\,|\Omega\rangle\, e^{-m_n t} \tag{3.45}$$

and the remaining terms of the infinite sum are treated as a perturbation. It follows then that the eigenvalues of $C^0(t)$ are given by

$$\lambda_n(t) = e^{-m_n t} \tag{3.46}$$

and the eigenvectors are related to the overlaps $\langle n|\,\hat{\mathcal{O}}_j^\dagger\,|\Omega\rangle$. These vectors are time-independent up to exponentially suppressed excited-state contamination [48], so if one finds an interval of time where the eigenvectors are time-independent then t_s

should be chosen from this interval. Note that one has access to $C(t)$ and not $C^0(t)$ to perform this decomposition, however when the time-independence of the vectors appears both matrices should be sufficiently similar. Fig. 3.3 shows the different entries for the first six singular vectors corresponding to the largest singular values as a function of time. The actual values of the different entries are not of importance, only their behavior with respect to time, and therefore no labels in the y axis are included. Three features are of interest in this plot. First, the early time-dependent contamination is more significant for the vectors of largest singular values yet it tends to disappear as time increases. Second, the time-independent expected behavior of the vectors is eventually exhibited. How fast the early contamination disappears seems to be different for every vector, with the ones corresponding to smaller singular values having the fastest convergence and clearest signal. Finally, for large enough values of time the different entries of each vector fluctuate more. This is related to the crossing that also happens in the GEVP formulation and which was explained previously. At sufficiently large times the singular values become very close and when sorting the vectors by the magnitudes of these values such crossings can occur. This is specially significant for the vectors of larger singular values and beyond $t = 6a$ the fluctuations and crossings make this ordering unreliable. It is convenient to choose $t_s = 4a$ and use only the first $N_S = 4$ singular vectors for the pruning of the correlation matrix. Here these N_S vectors are in a region where the time-independence can be seen. The singular values obtained with this choice of t_s are given in Table 3.2, where the first four singular values display a sufficiently clear dominance.

Index	Singular Value
1	13.1092(44)
2	0.057368(58)
3	0.0009372(22)
4	0.00002428(21)
5	0.000000832(25)
6	0.00000000901(58)
7	0.0000000000134(20)

TABLE 3.2: Singular values of the correlation matrix at $t_s = 4a$ using $\Gamma = \gamma_5$ and the seven Gaussian basis profiles in the Em1 ensemble.

The resulting pruning vectors are used to define the meson profile basis onto which the original correlation matrix will be projected and these profiles are displayed in Fig. 3.4, where they have been normalized so the initial value is positive. The first aspect to note is the pattern of nodes in the different profiles; the first one has no nodes, the second one has one node, the third one has two nodes and the fourth one has three nodes. This feature introduces additional non-trivial structure in distillation space and can be attributed to the relative negative signs in the entries of the pruning vectors. This will in turn lead to non-trivial spatial structure when the spatial profile of the meson operators is built from the corresponding optimal profiles, which are linear combinations of these pruned profiles. A second aspect is the suppression of larger eigenvalues is still conserved in these pruned profiles, which further indicates the importance of this feature.

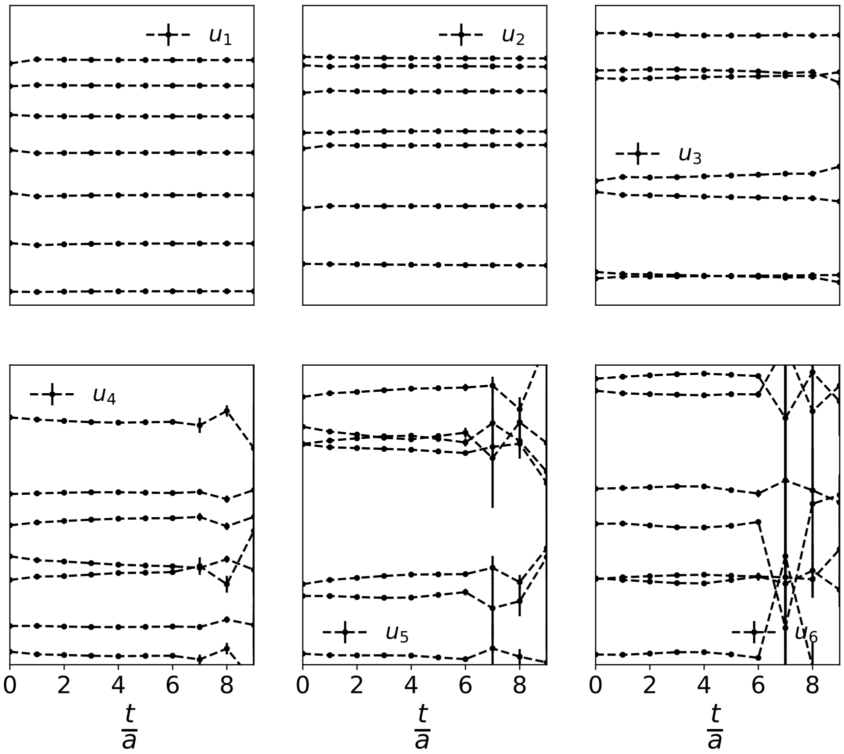

FIGURE 3.3: Entries of the six singular vectors corresponding to the six largest singular values of the 7×7 correlation matrix $C(t)$ for the $\Gamma = \gamma_5$ iso-vector operator in ensemble Em1. Dashed lines connecting the points serve to guide the eye.

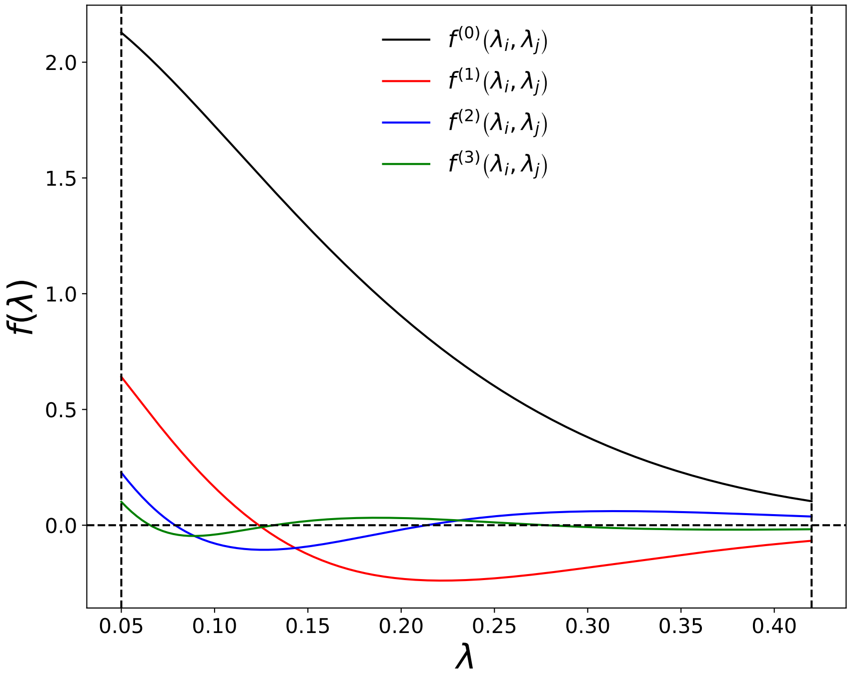

FIGURE 3.4: Pruned profiles built from the original basis of gaussian quark profiles and the selected pruning vectors for the $\Gamma = \gamma_5$ iso-vector operator in ensemble Em1.

With the chosen pruning vectors the pruned correlation matrix can now be constructed and used to solve the GEVP. The value of t_G chosen corresponds to the same value of t_S as it is recommended in [53, 54]. Since the dominance of the relevant states was shown to be acceptably established at $t = t_s$ and since t_G should be chosen under this same criterion then $t_G = t_S$ should work well. From the resulting GEVP the effective masses corresponding to the ground state are extracted from the generalized eigenvalues $\lambda_e(t, t_G)$ with $e = 0$. Remember the ordering of these eigenvalues and corresponding eigenvectors for a fixed t is done not necessarily by magnitude of the eigenvalue but rather by the similarity between the eigenvectors and those of a reference time t_r taken as $t_r = 8a$. To determine if such choice is appropriate one can look at the entries of the eigenvectors as a function of time. This is precisely what can be seen in Fig. 3.5, where $v_{i,j}$ denotes the j-th entry of the i-th vector, i.e the entries of $\omega_0(t, t_G)$. Up to excited-state contamination at early times for the entry $v_{1,4}$ all entries remain approximately constant. This allows to approximate the time-independent vector as an average over a suitably chosen time interval. The colored bands for the different entries show the chosen plateau interval for these vectors.

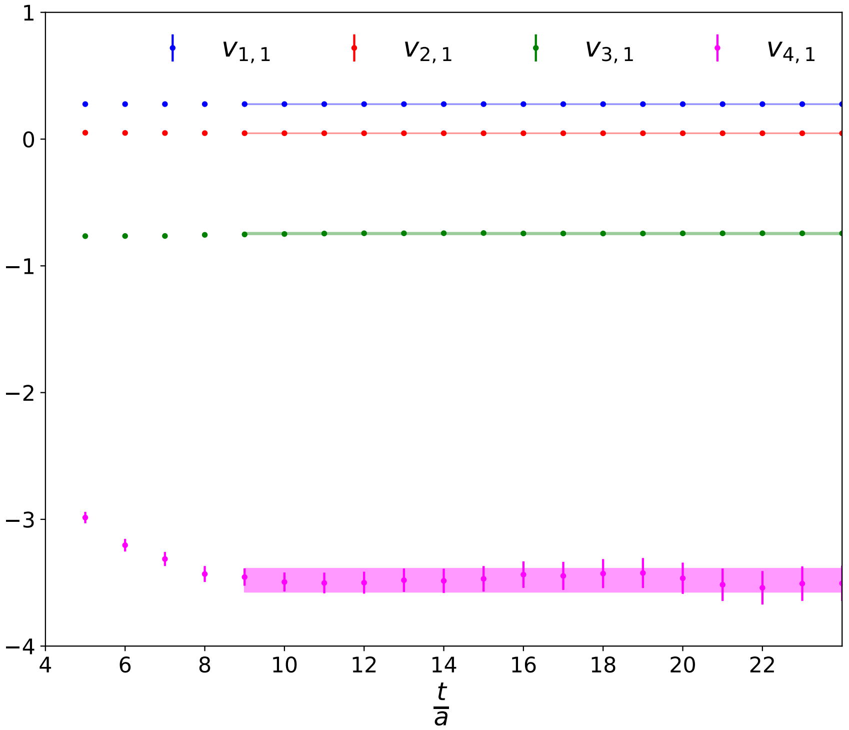

FIGURE 3.5: Entries of the GEVP vector corresponding to the ground state using the $\Gamma = \gamma_5$ iso-vector operator in ensemble Em1.

Neglecting contamination from other states, the vector of the plateau averages displayed in Fig. 3.5 should have unit $C(t_G)$-norm and be $C(t_G)$-orthogonal to excited states. These conditions are shown up to statistical fluctuations in App. B and numerically checked in the calculations. At this point the time independence of what is considered to be the ground state for the iso-vector $\Gamma = \gamma_5$ is expected, nonetheless it is necessary to verify that this assignment by extracting the effective masses from the obtained eigenvalues. These masses can be compared with standard distillation, i.e a quark profile $g(\lambda) = 1$ and therefore a meson profile $f(\lambda_i, \lambda_j) = 1$. Two things are expected. First, both should arrive at a same plateau value corresponding to the ground state mass. Second, the effective masses obtained from this GEVP should arrive considerably faster to this plateau value since they should correspond to a meson operator built from the optimal meson distillation profile. Fig. 3.6 shows this comparison for both ensembles. At sufficiently large values of time both sets of effective masses converge to the same value which confirms that both operators can access the ground state. It is also clear from comparing the effective masses at early times that excited-state contamination is considerably suppressed when the optimal meson distillation profile is used. This gives rise to an earlier mass plateau. The red and black bands displayed in the plot correspond to the plateau average and error which is calculated via a weighted average of the masses in the plateau region using the inverse squared errors as weights. It is important to note that just by looking at the data points it is clear that whatever the chosen plateau interval is for both sets the one for the case of the optimal meson profile should start earlier, however the strategy for choosing a precise starting and ending point for a mass plateau is something that varies from study to study. One would like to find a systematic method to determine an appropriate plateau region for arbitrary choice of Γ operators but this must be done in a very careful way. As presented in [125] one can set a fit-based criterion for the effective masses from a GEVP however the one presented there relies on constraints for the values of t and t_G that are not imposed in this work. As mentioned in [25] one should always visually verify any automatically determined plateau to avoid failure or bias. The mass plateaus in this work will always be determined via the visual inspection so that it is chosen when the masses are considered to reach a plateau region within errors. The starting point is chosen so there is no longer a decrease in the value of the effective masses but at most oscillations around an approximately constant point. The final point must be chosen with care, since the numerical instability of the GEVP at larger times can translate into mass points with considerable error. This final point is then fixed so no point before it deviates too much from the plateau.

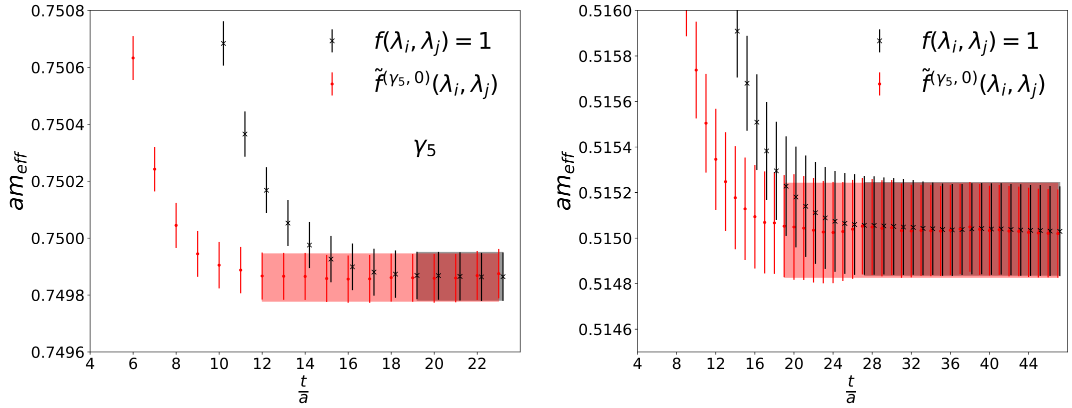

(A) In ensemble Em1.

(B) In ensemble Nm1.

FIGURE 3.6: Ground state effective masses of the iso-vector $\Gamma = \gamma_5$ operator using standard distillation ($f(\lambda_i, \lambda_j) = 1$) and distillation with the optimal meson distillation profile for the ground state $\left(\tilde{f}^{(\gamma_5,0)}(\lambda_i, \lambda_j)\right)$.

The mentioned important features seen in Fig. 3.6 can also be numerically quantified. First, both mass plateau averages for each ensemble are consistent, a fact reflected in the values $am = 0.749866(84)$ using standard distillation and $am = 0.749862(83)$ using the optimal profile in ensemble Em1 and $am = 0.51504(20)$ and

$am = 0.51503(21)$ correspondingly in ensemble Nm1. Second, the approach to the plateau region of both sets can be quantified by defining the *fractional overlap* of the operator used as presented in [120]. This quantity lies between 0 and 1 and the closer it is to 1 the more suppression of excited-state contamination there is. Fig. 3.7 shows how the effective overlaps of both standard distillation and the optimal profile behave as a function of time and their approximately flat behavior in the mass plateau region. From here a plateau average of this quantity can be defined in the same way as for the masses. The resulting plateau averages are $0.95711(31)$ for standard distillation and $0.99344(19)$ for the one with the optimal profile, which shows the significant shift towards 1 when the optimal profile is used. Even though the use of the optimal profile for the $\Gamma = \gamma_5$ operator brings a significant improvement the case with standard distillation already exhibits a fractional overlap larger than 0.9, which indicates this choice of Γ for this symmetry channel is already a good one.

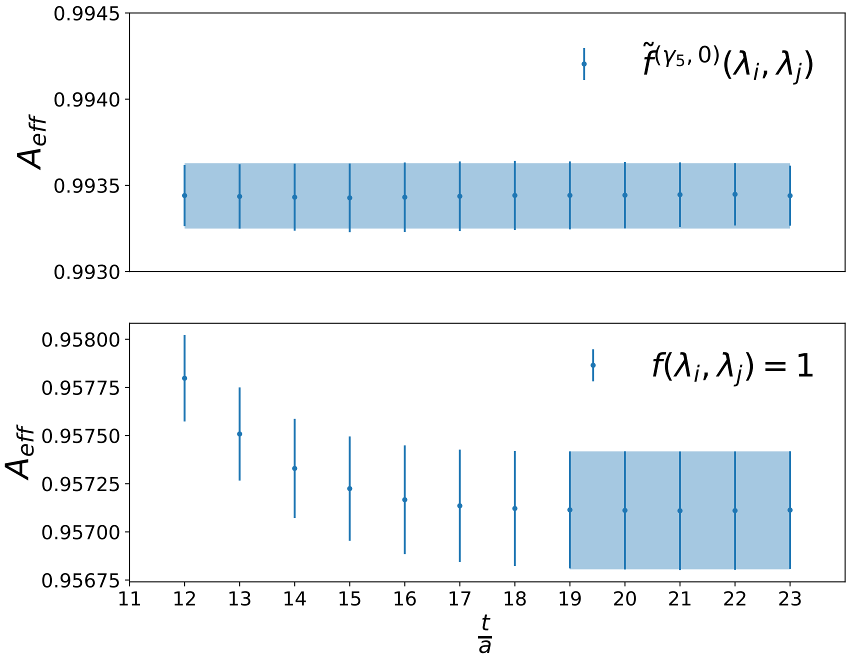

FIGURE 3.7: Ground state effective fractional overlaps of the iso-vector $\Gamma = \gamma_5$ operator using standard distillation ($f(\lambda_i, \lambda_j) = 1$) and distillation with the optimal meson distillation profile for the ground state $\left(\tilde{f}^{(\gamma_5,0)}(\lambda_i, \lambda_j)\right)$ in ensemble Em1.

At this point the improvement yielded by using the optimal meson distillation has been both qualitatively and quantitatively shown for the iso-vector $\Gamma = \gamma_5$ operator for the A_1^{-+} channel. The significantly earlier access to the mass plateau region is of particular importance for the iso-scalar operator of this channel. One can now check how well the masses of radial excitations can be measured using the corresponding optimal profiles. Fig. 3.8 shows the effective masses corresponding to the first excited state of this channel in both ensembles, from where somewhat clear mass plateaus can be defined. Access to a first excited state purely through the inclusion of an optimal profile for a fixed Γ operator, even if the signal is not as clear as for the ground state, is yet another advantage of the use of these profiles. Measurements of excited states in other works that employ distillation are achieved by the use of different Γ operators for a same symmetry channel, however the inclusion of a basis of different profiles introduces an additional degree of freedom for a GEVP formulation which can be based on a single Γ operator. The use of different Γ operators with different profiles in a single GEVP will be considered later on in this work.

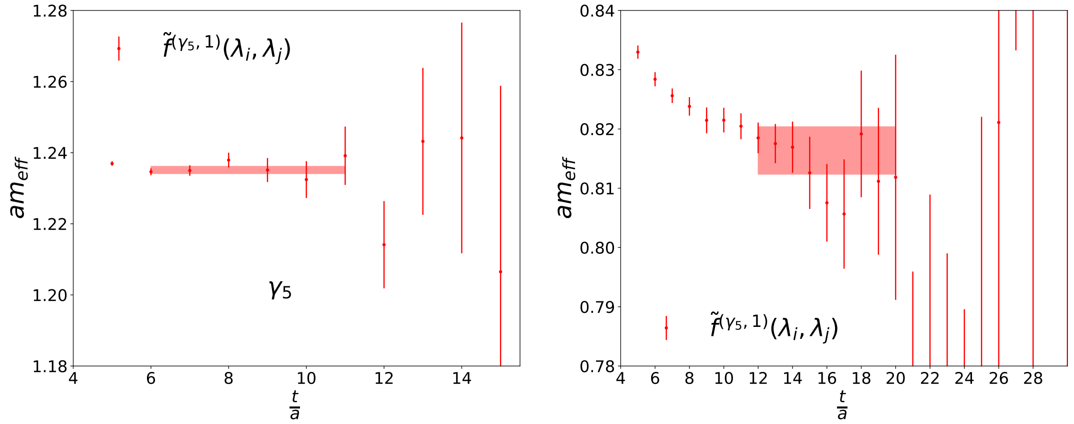

(A) In ensemble Em1.

(B) In ensemble Nm1.

FIGURE 3.8: First excited state effective masses of the iso-vector $\Gamma = \gamma_5$ operator using standard distillation ($f(\lambda_i, \lambda_j) = 1$) and distillation with the corresponding optimal meson distillation profile $\left(\tilde{f}^{(\gamma_5,1)}(\lambda_i,\lambda_j)\right)$.

One last issue is the use of different choices of N_v. Via the scaling with the physical volume of the lattice [23] one can get an initial estimate of an appropriate choice of N_v for standard distillation and then introduce the optimal profiles. One expects different choices of N_v can lead to different levels of excited-state contamination in standard distillation, given the additional vectors are not used in the optimal way, while use of optimal profiles should guarantee all available vectors are being used in the best way possible. This expectation is confirmed by the effective masses displayed in Fig. 3.9 calculated in the Em1 ensemble. Using a sample of 1500 gauge configurations, the case of standard distillation with the choice of $N_v = 200$ brings considerably more excited-state contamination compared to $N_v = 100$. This is of particular importance since, compared to the total of 3×24^3 possible eigenvectors, both 100 and 200 would seem equally small in order of magnitude and feasible for the calculations. If one were to use $N_v = 200$ instead of $N_v = 100$ in standard distillation thinking that including the additional 100 vectors could help improve the resulting effective masses then the completely opposite effect is obtained. Nonetheless, the corresponding optimal profiles show the excited-state contamination is almost equally suppressed, i.e the additional 100 vectors are used so no additional contamination is introduced. Nonetheless one can still observe a slight difference between $N_v = 100$ and $N_v = 200$ with the optimal profiles in the contamination at early times. This is expected, since using 100 additional vectors in an optimal manner should give rise to an improvement as long as the corresponding value of the profile for those eigenvectors is not 0. These observations indicate that as long as the optimal profile is used then the choice of $N_v = 325$ for ensemble Nm1 yield very similar results to having used the 660 that the volume scaling suggests at least for the ground state effective masses.

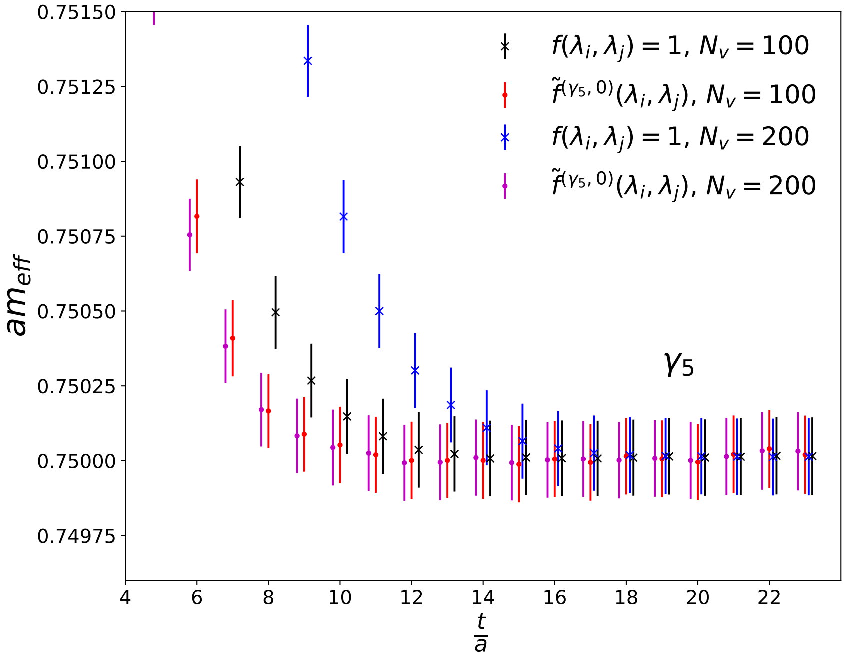

FIGURE 3.9: Ground state effective masses of the iso-vector $\Gamma = \gamma_5$ operator using both standard distillation and the optimal profiles for $N_v = 100$ and $N_v = 200$ in ensemble Em1.

All other local Γ operators are now analyzed in the same manner as $\Gamma = \gamma_5$ was. The ground state effective masses for these operators are displayed in Fig. 3.10 for ensemble Em1 and Fig. 3.11 for ensemble Nm1 including the corresponding mass plateaus. The use of the optimal profile leads to a suppression of excited-state contamination as with the $\Gamma = \gamma_5$ case. The resulting fractional overlaps are given in Table 3.3 including the first excited. All operators are improved to some degree. The level of improvement is different for different choices of Γ, with γ_i and $\epsilon_{ijk}\gamma_j\gamma_k$ displaying the largest shift towards 1. Note that regardless of the improvement achieved via optimal profiles for a chosen Γ this operator might by itself not be the best one to use to study a given symmetry channel. This is seen for the $\Gamma = \epsilon_{ijk}\gamma_j\gamma_k$ and serves as an additional motivation to use derivative-based operators. Nonetheless these local operators with optimal profiles already provide clear access to the ground state of interest.

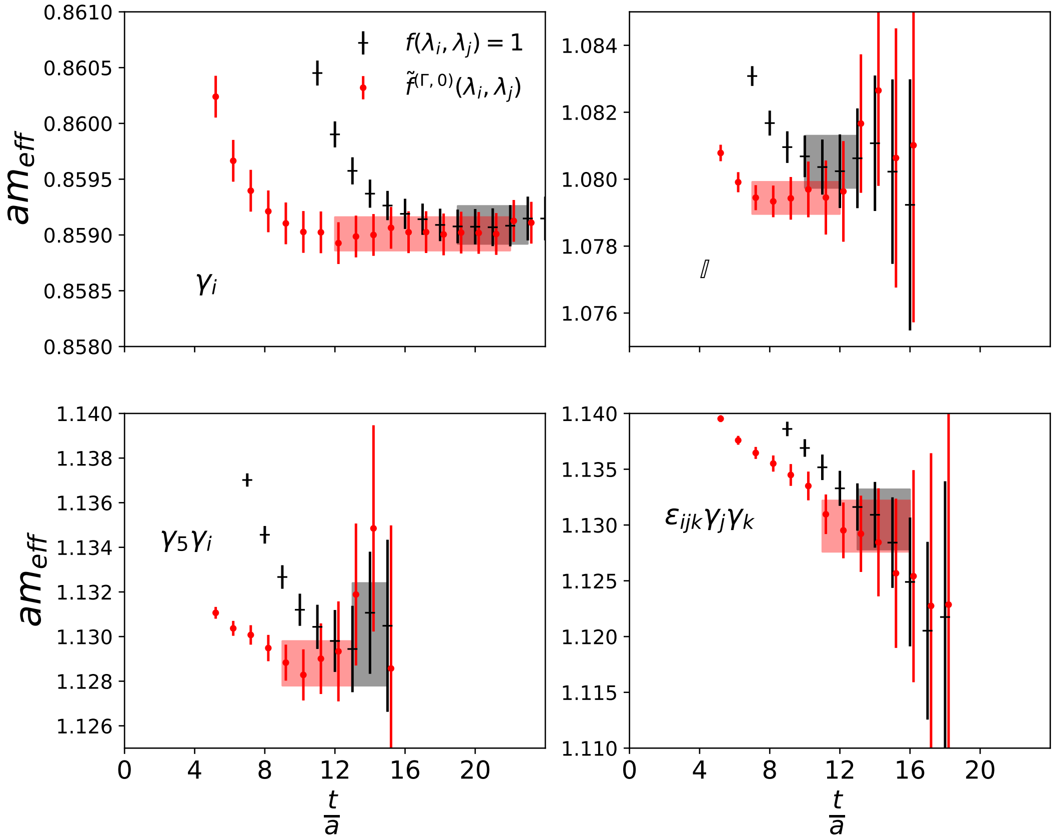

FIGURE 3.10: Ground state effective masses of the iso-vector operators built from local Γ not including the $\Gamma = \gamma_5$ case in ensemble Em1.

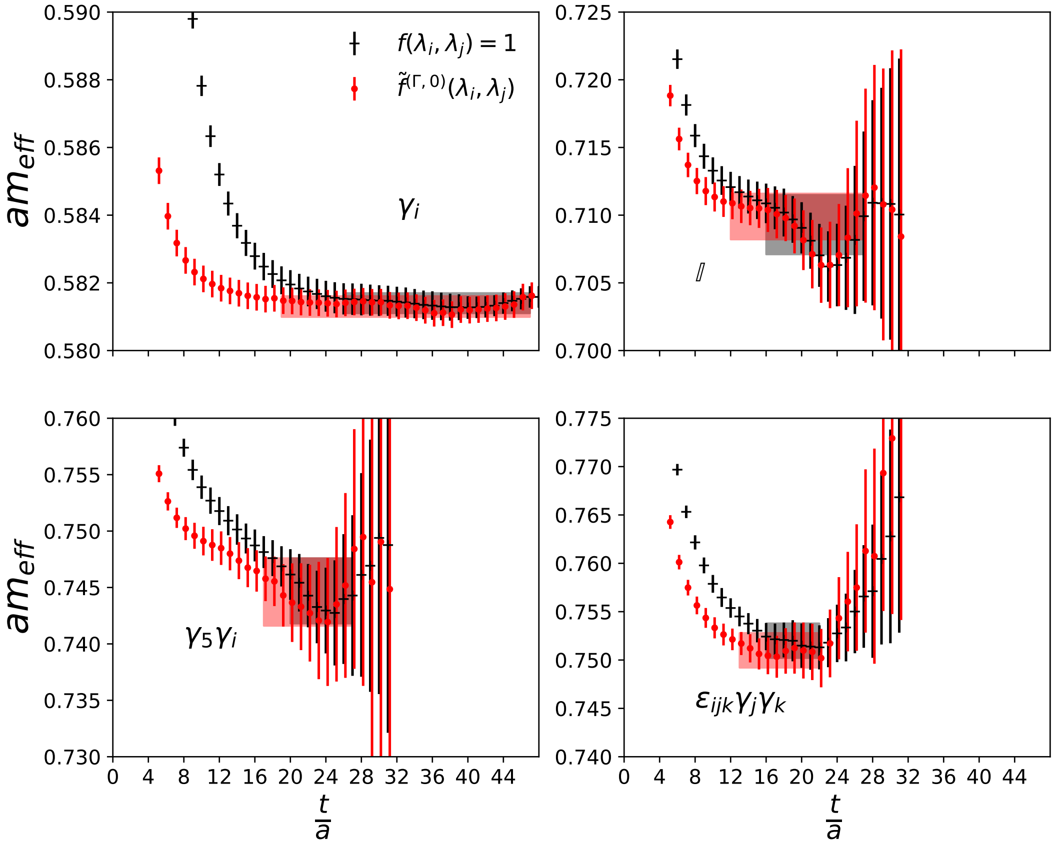

FIGURE 3.11: Ground state effective masses of the iso-vector operators built from local Γ not including the $\Gamma = \gamma_5$ case in ensemble Nm1.

		γ_5	γ_i	$\mathbb{I}$	$\gamma_5\gamma_i$	$\epsilon_{ijk}\gamma_j\gamma_k$
Em1	$f(\lambda_i,\lambda_j)=1$	0.95711(31)	0.9181(14)	0.9689(38)	0.939(18)	0.892(18)
	$\tilde{f}^{(\Gamma,0)}(\lambda_i,\lambda_j)$	0.99344(19)	0.99498(67)	0.99470(85)	0.9907(41)	0.953(13)
	$\tilde{f}^{(\Gamma,1)}(\lambda_i,\lambda_j)$	0.9914(17)	0.99632(76)	0.9795(52)	0.968(17)	0.9689(70)
Nm1	$f(\lambda_i,\lambda_j)=1$	0.91439(72)	0.8669(38)	0.913(15)	0.846(34)	0.881(13)
	$\tilde{f}^{(\Gamma,0)}(\lambda_i,\lambda_j)$	0.97225(56)	0.9784(36)	0.9650(54)	0.933(24)	0.9406(88)
	$\tilde{f}^{(\Gamma,1)}(\lambda_i,\lambda_j)$	0.928(18)	0.935(22)	0.894(32)	0.874(32)	0.816(38)

TABLE 3.3: Fractional overlaps of the local Γ operators using standard distillation and the optimal meson profiles in ensembles Em1 and Nm1.

Radial excitations can be accessed via the corresponding optimal profiles for these local operators. The effective masses can be seen in Fig. 3.12 from ensemble Em1 and Fig. 3.13 for ensemble Nm1 with their corresponding plateaus, from where two observations can be made. First, there is a signal with all operators, so the use of the optimal profile already yields operators that create states similar to the wanted excited energy eigenstates. Second, even though the plateaus displayed give a first indication of the mass of the state, the signal is not as clear as the ground state. This is expected, since excited states probably contain more complex spatial structure that local Γ operators might not appropriately sample. Furthermore, the quality of the signal in the effective masses is operator dependent, which relates to the previously mentioned innate quality of the Γ operator. A first glimpse would indicate the $\Gamma=\gamma_i$ operator with its optimal profile has the best access to its corresponding excited state however no definitive statements about the overall structure of these excitations can be made until more operators are used.

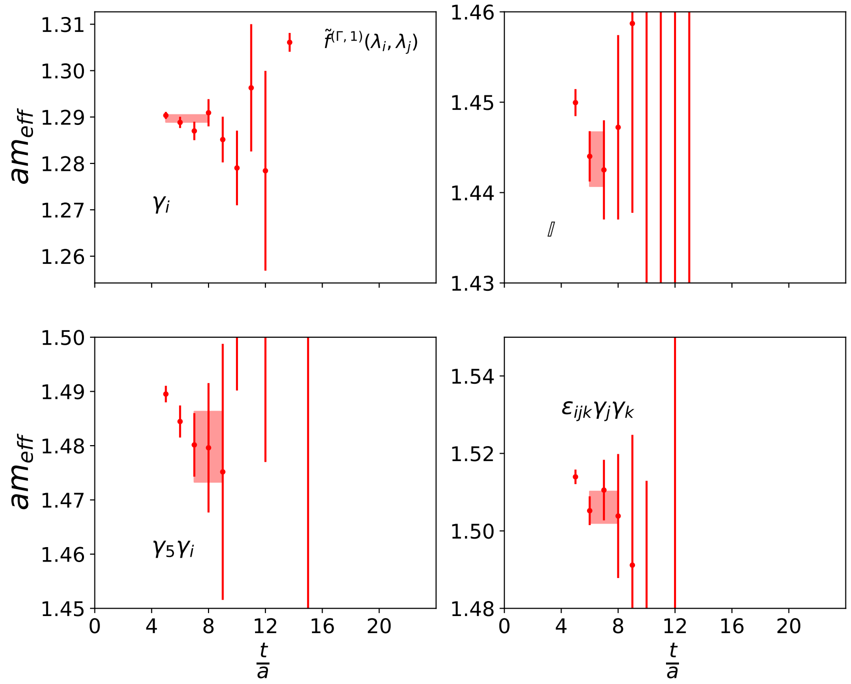

FIGURE 3.12: First excited state effective masses of the iso-vector operators built from local Γ not including the $\Gamma=\gamma_5$ case in ensemble Em1.

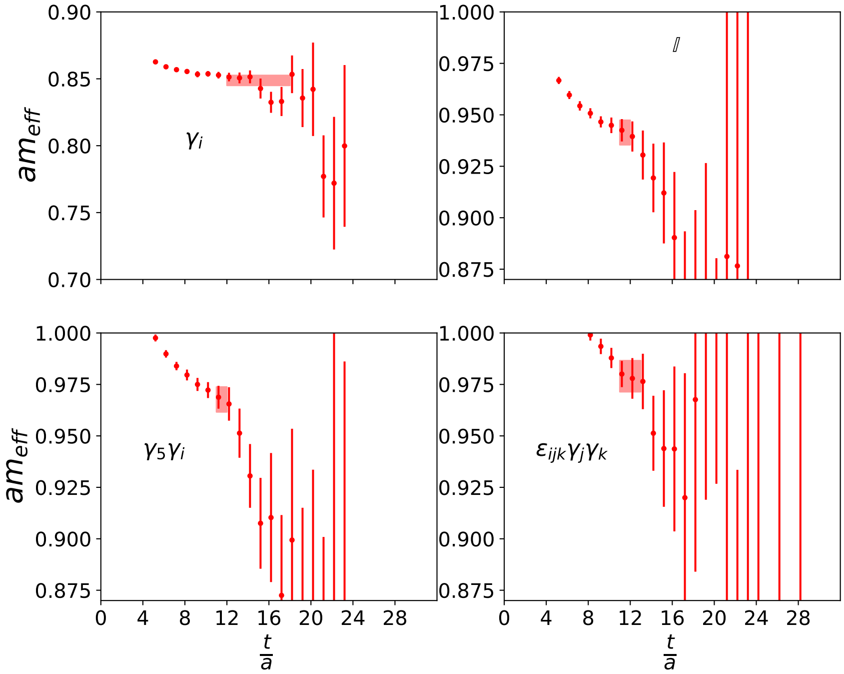

FIGURE 3.13: First excited state effective masses of the iso-vector operators built from local Γ not including the $\Gamma = \gamma_5$ case in ensemble Nm1.

The resulting mass spectrum in lattice units from the local operators is presented in Table 3.4. For each operator the first two rows correspond to the plateau average of the ground state using standard distillation and the optimal profile respectively while the third row corresponds to the plateau average of the first excited state using the optimal profile. Next to each average is the plateau interval used. Good agreement between standard distillation and the optimal profile is observed for the ground state, with the main difference being the location of each plateau and its length. In all cases the plateau using the optimal profile is located earlier in time and is longer. This clearly displays the main advantage of using the profiles. Note even when the plateau averages are identical within errors, such as for the cases $\Gamma = \gamma_5\gamma_i$, having a longer and earlier plateau is preferable for the inclusion of the disconnected piece of the temporal correlation function relevant for the iso-scalar operators which will be considered later.

Ensemble	Γ	Plateau masses	Plateau intervals
Em1	γ_5	0.749866(84)	19-23
		0.749862(83)	12-22
		1.2351(10)	6-11
	γ_i	0.85909(17)	19-23
		0.85901(15)	12-22
		1.28969(78)	5-8
	$\mathbb{I}$	1.08052(78)	10-13
		1.07944(48)	7-12
		1.4437(30)	6-7
	$\gamma_5\gamma_i$	1.1301(23)	13-15
		1.1288(10)	9-13
		1.4798(65)	7-9
	$\epsilon_{ijk}\gamma_j\gamma_k$	1.1305(27)	13-16
		1.1299(23)	11-16
		1.5061(41)	6-8
Nm1	γ_5	0.51504(20)	27-47
		0.51503(21)	19-47
		0.8164(40)	12-20
	γ_i	0.58140(31)	26-47
		0.58130(31)	19-47
		0.8488(38)	12-18
	$\mathbb{I}$	0.7093(22)	16-27
		0.7099(17)	12-27
		0.9414(60)	11-12
	$\gamma_5\gamma_i$	0.7447(29)	20-27
		0.7446(30)	17-27
		0.9677(61)	11-12
	$\epsilon_{ijk}\gamma_j\gamma_k$	0.7520(18)	16-22
		0.7510(18)	13-22
		0.9790(76)	11-13

TABLE 3.4: Plateau average masses for the ground and first excited states using local Γ operators in both ensembles. For a fixed Γ the first row corresponds to the ground state obtained via standard distillation, the second row for this same state but using the optimal profile and the third row with the first excited state using the optimal profile.

3.4.5.2 Derivative-based Γ operators

The same analysis used for the local Γ operators can now be applied to different choices of derivative-based Γ operators. The main difference is the elementals are no longer diagonal in distillation space yet the overall steps to extract the effective masses remains the same. As mentioned before, this kind of operators accesses irreps that local operators cannot, e.g E^{++}, T_2^{++} and T_1^{-+}, as well as to sample more complex spatial structure and explicit dependence on link variables that local operators cannot. The first operators analyzed correspond to the E^{++} and T_2^{++} irreps whose ground state in the continuum limit becomes the 2^{++}. Fig. 3.14 shows the effective masses and corresponding plateaus of the ground state for the $\Gamma = \mathbb{Q}_{ijk}\gamma_j\nabla_k$ (E^{++}) and $\Gamma = |\epsilon_{ijk}|\gamma_j\nabla_k$ (T_2^{++}) operators using both standard distillation and the corresponding optimal meson profiles in both ensembles. As expected the effective masses from both operators are very similar, more so in Nm1 than in Em1 due to the smaller lattice spacing. This similarity is present for both standard distillation and the optimal profiles particularly at early values of time. At later values of time both operators become dominated by statistical noise and their values drift apart from each other. Just as for the local operators using the optimal profiles leads to a considerable suppression of excited-state contamination, leading to earlier mass plateaus. The plateaus obtained for both operators using standard distillation agree quite well while the ones from the optimal profiles display a small tension in the case of Em1. This could be attributed to the propagation of the statistical error in the non-linear solution of the GEVP or the non-zero lattice spacing. Since in Nm1 this tension is not present the latter effect is probably the dominant cause.

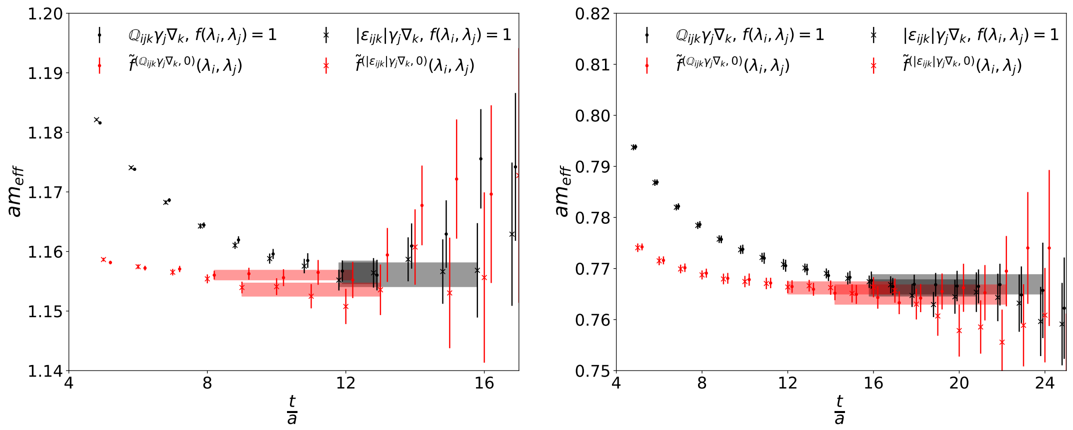

(A) In ensemble Em1. (B) In ensemble Nm1.

FIGURE 3.14: Ground state effective masses of the iso-vector $\Gamma = \mathbb{Q}_{ijk}\gamma_j\nabla_k$ and $\Gamma = |\epsilon_{ijk}|\gamma_j\nabla_k$.

The next case of interest is the A_1^{-+} derivative-based operators, i.e $\Gamma = \gamma_0\gamma_5\gamma_i\nabla_i$, $\gamma_i\mathbb{B}_i$. Fig. 3.15 shows the ground state effective masses for the iso-vector case for both operators using standard distillation and the optimal profiles with their corresponding plateaus in both ensembles. Using standard distillation both operators eventually reach a plateau consistent within errors but the $\gamma_i\mathbb{B}_i$ operator exhibits considerably less excited-state contamination. This speaks in favor of including explicit gluonic excitations via the $\mathbb{B}_i$ chromo-magnetic operator. The second thing to note is the use of the optimal profile leads to a significant improvement for the $\Gamma = \gamma_0\gamma_5\gamma_i\nabla_i$ operator, reducing its excited-state contamination below the $\Gamma = \gamma_i\mathbb{B}_i$ one with standard distillation without significantly increasing the noise of the effective masses. The final thing to note is such significant improvement is not observed for the $\Gamma = \gamma_i\mathbb{B}_i$. Although there is a suppression of excited-state contamination at very early times, both effective masses from standard distillation and optimal profile quickly become very similar. A possible explanation, as mentioned in [120], is either the contribution from the ground energy eigenstate in the state created by this meson operator cannot be sufficiently enhanced by the inclusion of a profile or the contributions from excited states, particularly with hybrid states high up the ladder of excitations expected from the use of the $\mathbb{B}_i$ operator, cannot be sufficiently suppressed. This issue will have to be handled with tools different from the meson profiles and such study is outside the scope of this work, nonetheless this shows the limitations of the optimal profiles. Since the case of $\Gamma = \gamma_0\gamma_5\gamma_i\nabla_i$ gains a significant improvement from the optimal profile, there is further indication that explicit gluonic excitations in the meson operators have to be improved with a method different than the optimal profiles.

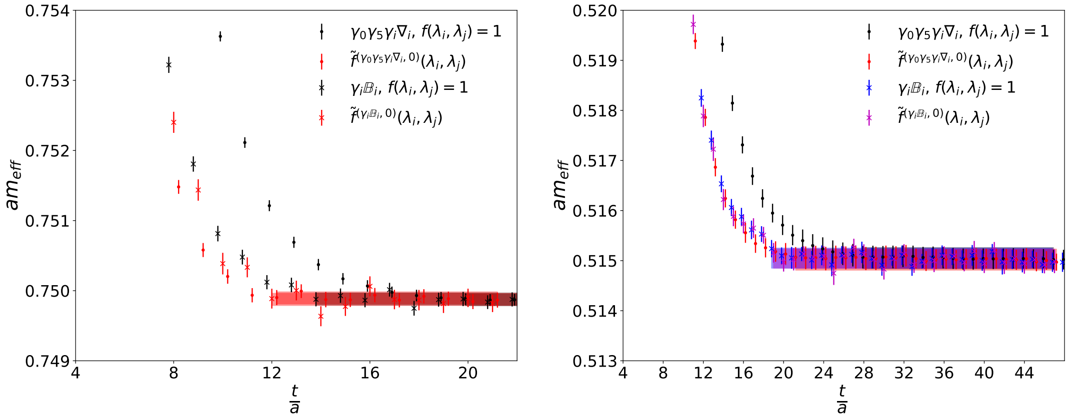

(A) In ensemble Em1.

(B) In ensemble Nm1.

FIGURE 3.15: Ground state effective masses of the iso-vector $\Gamma = \gamma_0\gamma_5\gamma_i\nabla_i$ and $\Gamma = \gamma_i\mathbb{B}_i$.

One can now look at the T_1^{--} derivative-based operators given by $\Gamma = \nabla_i$ and $\Gamma = \gamma_5\mathbb{B}_i$. Fig. 3.16 shows the resulting ground state effective masses for the iso-vector case for both operators using standard distillation and the optimal profiles with their corresponding plateaus in both ensembles. Similar features as for the A_1^{-+} case are observed. Using standard distillation the operator with the chromomagnetic component $\mathbb{B}_i$ exhibits less excited-state contamination compared to the operator with a single derivative, however the inclusion of the optimal profile yields a much clearer improvement for the former than for the latter. The reason for this is probably the same as it was for the A_1^{-+} case. This further indicates the $\mathbb{B}_i$ must be handled with care and improved in a different manner. For the remaining symmetry channels a single derivative-based operator was used. These mass plateau averages and corresponding intervals are presented in Table 3.5 for ensemble Em1 and Table 3.6 for ensemble Nm1. As with local operators, the optimal profiles lead to a significant suppression of excited-state contamination at early times while also yielding earlier plateaus compatible with their standard distillation counterparts.

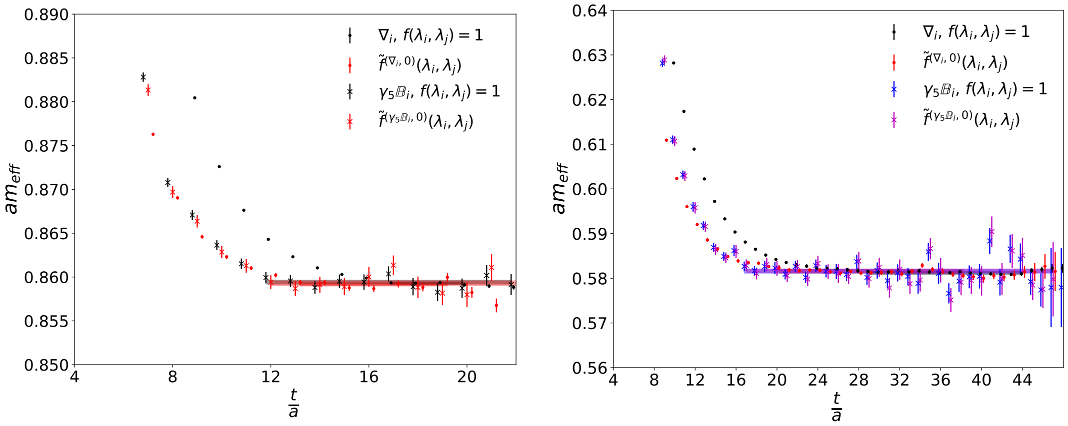

(A) In ensemble Em1.

(B) In ensemble Nm1.

FIGURE 3.16: Ground state effective masses of the iso-vector $\Gamma = \nabla_i$ and $\Gamma = \gamma_5 \mathbb{B}_i$.

The effective masses for the first excited state of these symmetry channels using the optimal profiles with their corresponding plateaus are also given in Table 3.5 together with the fractional overlaps to compare the ground state with and without the use of the optimal profile. In the case of the A_1^{-+} and T_1^{--} irreps, the one-derivative operators provide a clearer access to the first excited state than the two-derivative ones involving the chromo-magnetic component. This relates to the previously discussed issue of the latter operators having overlaps with hybrid states up the ladder of excitations which are not sufficiently suppressed by the use of a profile. Nonetheless the plateaus for these operators, although they have a larger error, appear to be in agreement with the one-derivative operators. As stated before, further improvements to these two-derivative operators on top of an optimal profile might result in clearer and longer plateaus.

A final channel of interest is T_1^{-+} which is only accessible via derivative-based operators. As was previously explained these quantum numbers cannot be realized by a $\bar{q}q$ state in the quark model and an additional gluonic excitation serves as a possible explanation. Fig. 3.17 displays the ground state effective masses and corresponding plateaus for the iso-vector operators $\Gamma = \gamma_0 \nabla_i$ and $\Gamma = \epsilon_{ijk} \gamma_j \mathbb{B}_k$ using both standard distillation and the optimal profiles for both ensembles, where the former operator is not used for ensemble Nm1. The operator involving the chromo-magnetic component $\mathbb{B}_i$ is of special relevance since the ground state is expected to have a significant contribution from a gluonic excitation. Three observations can be made from these two operators. First, using standard distillation both display a very similar degree of excited-state contamination, which would not lead to a preference toward either of them. Second, the use of the optimal profile does not lead to a significant improvement in the $\Gamma = \gamma_0 \nabla_i$ operator, reflected in completely consistent plateaus, possibly indicating the operator by itself does not create a state resembling the energy eigenstate and the profile cannot enhance the corresponding overlap sufficiently. For this reason it was not used for the Nm1 ensemble. Third, the optimal profile leads to an improvement for operator $\Gamma = \epsilon_{ijk} \gamma_j \mathbb{B}_k$, albeit with a slight increase in the error, and therefore to a slightly earlier plateau with a small tension with standard distillation. No clear signal for the first excited state of either operators of this irrep is observed and therefore no plots are presented.

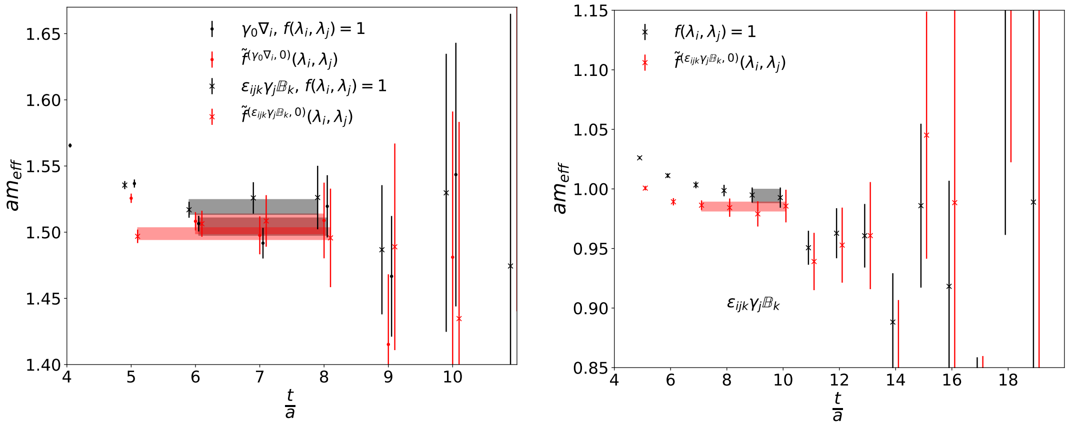

(A) In ensemble Em1.

(B) In ensemble Nm1.

FIGURE 3.17: Ground state effective masses of the iso-vector $\Gamma = \gamma_0\nabla_i$ and $\Gamma = \epsilon_{ijk}\gamma_j\mathbb{B}_k$.

Γ	Plateau masses	Fractional overlaps	Plateau intervals
$\gamma_0\gamma_5\gamma_i\nabla_i$	0.749869(84)	0.95749(30)	20-23
	0.749897(86)	0.99405(20)	12-21
	1.2367(25)	0.9900(30)	8-12
$\gamma_i\mathbb{B}_i$	0.749879(86)	0.90701(51)	14-23
	0.74984(11)	0.92701(81)	12-23
	1.220(18)	0.56(11)	10-12
∇_i	0.85929(14)	0.80353(89)	17-20
	0.85916(18)	0.9337(11)	13-19
	1.3134(60)	0.896(16)	9-12
$\gamma_5\mathbb{B}_i$	0.85942(22)	0.7240(14)	12-22
	0.85931(25)	0.7343(18)	12-22
	1.356(23)	0.684(51)	7-8
$\gamma_i\nabla_i$	1.07920(46)	0.9716(20)	9-13
	1.07924(35)	0.99218(88)	7-13
	1.431(13)	0.916(48)	8-9
$\epsilon_{ijk}\gamma_j\nabla_k$	1.1293(16)	0.908(11)	13-16
	1.12915(71)	0.9866(30)	9-13
	1.4788(19)	0.9929(19)	5-8
$\gamma_5\nabla_i$	1.1344(16)	0.894(13)	13-15
	1.13459(91)	0.9829(37)	9-14
	1.4790(25)	0.9909(13)	5-8
$\mathbb{Q}_{ijk}\gamma_j\nabla_k$	1.1565(19)	0.896(12)	12-13
	1.15604(81)	0.9911(27)	8-12
	1.4965(22)	0.9927(22)	5-7
$\lvert\epsilon_{ijk}\rvert\gamma_j\nabla_k$	1.1561(20)	0.894(13)	12-16
	1.1536(11)	0.9801(45)	9-13
	1.4940(24)	0.9917(24)	5-7
$\gamma_0\nabla_i$	1.5042(66)	0.913(11)	6-8
	1.5063(75)	0.942(13)	6-8
$\epsilon_{ijk}\gamma_j\mathbb{B}_k$	1.5191(56)	0.946(11)	6-8
	1.4989(45)	0.9799(50)	5-8

TABLE 3.5: Plateau average masses and fractional overlaps for the ground and first excited states using derivative-based Γ operators in ensemble Em1. For a fixed Γ the first row corresponds to the ground state using standard distillation, the second row to the ground state using the optimal profile and the third row to the first excited state using the optimal profile.

Γ	Plateau masses	Fractional overlaps	Plateau intervals
$\gamma_0\gamma_5\gamma_i\nabla_i$	0.51505(21)	0.6425(11)	28-47
	0.51502(21)	0.80242(86)	21-47
	0.8240(31)	0.788(15)	11-14
$\gamma_i\mathbb{B}_i$	0.51505(20)	0.73818(54)	19-47
	0.51504(19)	0.75430(59)	19-47
	0.8255(70)	0.595(32)	10-14
∇_i	0.58123(38)	0.4146(20)	29-44
	0.58158(43)	0.6413(19)	20-38
	0.8651(51)	0.664(29)	11-15
$\gamma_5\mathbb{B}_i$	0.58160(45)	0.4247(19)	17-47
	0.58165(43)	0.4401(31)	17-47
	0.855(26)	0.348(64)	10-14
$\gamma_i\nabla_i$	0.7108(10)	0.9326(42)	12-24
	0.7106(11)	0.9535(42)	12-24
	0.9393(85)	0.833(51)	12-16
$\gamma_5\nabla_i$	0.7526(17)	0.873(14)	17-27
	0.7528(13)	0.9619(51)	11-24
	0.9789(41)	0.9574(94)	8-14
$\mathbb{Q}_{ijk}\gamma_j\nabla_k$	0.7669(19)	0.868(16)	16-24
	0.7649(19)	0.952(12)	14-22
	0.9855(67)	0.949(18)	9-15
$\|\epsilon_{ijk}\|\gamma_j\nabla_k$	0.7662(16)	0.862(14)	16-21
	0.7662(12)	0.9654(77)	12-17
	0.9747(78)	0.901(37)	10-14
$\epsilon_{ijk}\gamma_j\mathbb{B}_k$	0.9941(57)	0.892(24)	9-10
	0.9852(38)	0.957(11)	7-10
	1.2136(94)	0.9580(96)	6-9

TABLE 3.6: Plateau average masses for the ground and first excited states using derivative-based Γ operators in ensemble Nm1. For a fixed Γ the first row corresponds to the ground state using standard distillation, the second row to the ground state using the optimal profile and the third row to the first excited state using the optimal profile.

A final calculation of interest are the mass splittings given by [126]

$$\begin{aligned}
\Delta m_{HF} &= m_{J/\Psi} - m_{\eta_c} \\
\Delta m_{1P-1S} &= m_{\overline{1P}} - m_{\overline{1S}} \\
\Delta m_{SO} &= \frac{1}{9}\left(5m_{\chi_{c2}} - 3m_{\chi_{c1}} - 2m_{\chi_{c0}}\right) \\
\Delta m_{tensor} &= \frac{1}{9}\left(3m_{\chi_{c1}} - m_{\chi_{c2}} - 2m_{\chi_{c0}}\right) \\
\Delta m_{1PHF} &= m_{\overline{1P}} - m_{h_c},
\end{aligned} \tag{3.47}$$

where Δm_{HF} is the $1S$ hyperfine splitting, Δm_{1P-1S} is the spin-average $1P-1S$ splitting, Δm_{SO} is the spin-orbit splitting, Δm_{tensor} is the tensor splitting, Δm_{1PHF} is the

P-wave hyperfine splitting and

$$m_{\overline{1S}} = \frac{1}{4}\left(m_{\eta_c} + 3m_{J/\Psi}\right)$$
$$m_{\overline{1P}} = \frac{1}{9}\left(m_{\chi_{c0}} + 3m_{\chi_{c1}} + 5m_{\chi_{c2}}\right) \tag{3.48}$$

are the spin-averaged masses of the S- and P-waves respectively. These splittings are measured for both ground and first excited states using the iso-vector operators that yield the clearest signal in each channel and the results are presented in Table 3.7 for both ensembles. Relatively good precision is achieved in all the splittings thanks to the earlier and most of the times longer plateaus from where the masses are extracted. These mass splittings are converted to physical units since the lattice spacing of each ensemble is known, however the differences of the $N_f = 2$ model used with respect to nature makes a straightforward comparison impossible. Additionally, the error of the lattice spacing would dominate the final propagated error. Nonetheless this is not a problem since the main goal is to show that the proposed method of optimal profiles leads to effective masses with much less excited-state contamination, something that is independent of the scale-setting procedure. Fig. 3.18 shows the spectrum for both ensembles with this separation of uncertainty sources. The solid rectangles represent the masses converted to physical units neglecting the error of the lattice spacing while the light rectangles containing them represent the total error including lattice spacing error.

Ensemble	Splitting	Ground state	1^{st} excited state
Em1	Δm_{HF}	0.10911(10)	0.0532(22)
	Δm_{1P-1S}	0.30683(57)	0.2083(16)
	Δm_{SO}	0.02599(42)	0.0176(11)
	Δm_{tensor}	0.00806(21)	0.00582(76)
	Δm_{1PHF}	0.00398(83)	0.0057(22)
Nm1	Δm_{HF}	0.06627(21)	0.0325(17)
	Δm_{1P-1S}	0.1873(18)	0.1341(34)
	Δm_{SO}	0.0190(10)	0.0157(29)
	Δm_{tensor}	0.00546(70)	0.0039(10)
	Δm_{1PHF}	-0.0007(13)	-0.0042(55)

TABLE 3.7: Mass splittings for ground and first excited states in ensembles Em1 and Nm1.

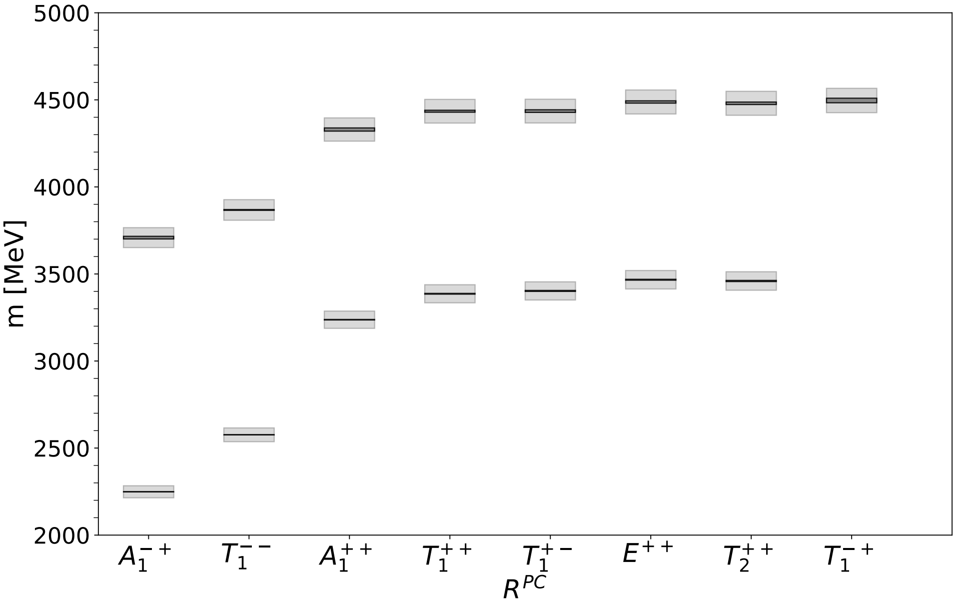

(A) In ensemble Em1.

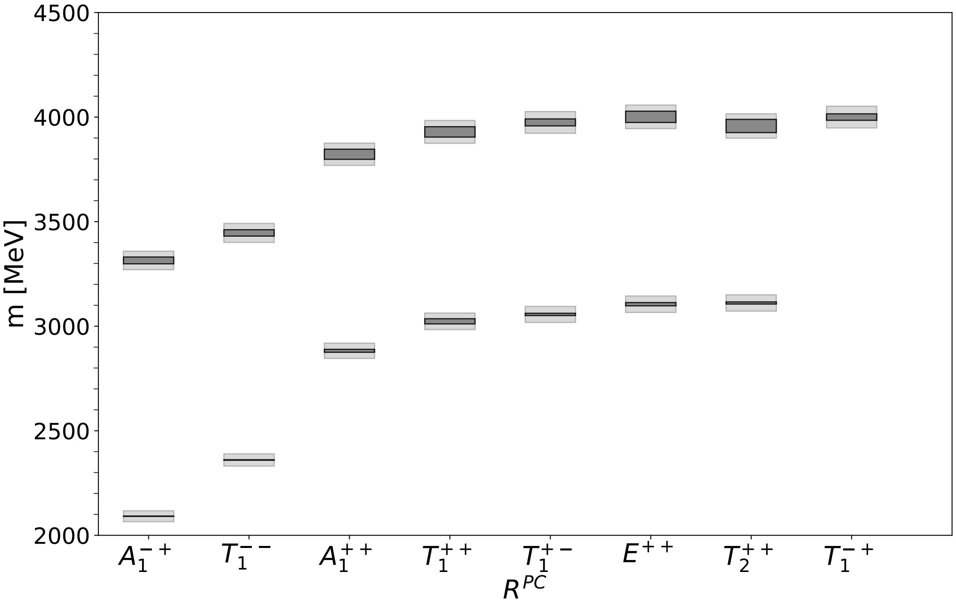

(B) In ensemble Nm1.

FIGURE 3.18: Charmonium spectrum obtained in the $N_f = 2$ ensembles. Solid rectangles ignore the error from the lattice spacing while the light rectangles take it into account.

3.4.5.3 Mixed Γ operators

The use of the optimal profiles yields a substantial gain when accessing the mass of the different states compared to standard distillation for a fixed Γ operator. Nonetheless this is not the last improvement that can be introduced. As explained in Sect. 3.3, it is also possible to build a correlation matrix which involves not only multiple profiles but also multiple Γ operators for a fixed symmetry channel. This approach can help further exploit the properties of different Γ operators already enhanced by different distillation profiles. A first calculation is the comparison of the effective masses obtained from an optimal profile for a fixed Γ operator with the effective masses obtained from a GEVP including different Γ operators using standard distillation. This comparison shows the profiles optimize the resulting meson operator in a way not equivalent to the inclusion of different Γ operators and lead to a larger improvement. This calculation uses operators that transform according to T_1^{--}, namely $\Gamma = \gamma_i, \nabla_i$. The first step is building a 2×2 correlation matrix involving both operators using standard distillation and solving the GEVP. The resulting effective masses for the ground state are shown in Fig. 3.19 together with the ones obtained individually from each operator using standard distillation and from using only $\Gamma = \gamma_i$ with its optimal profile. A slight improvement at early times can be observed from the optimal combination of both operators using standard distillation compared to the one using only $\Gamma = \gamma_i$, which means the inclusion of $\Gamma = \nabla_i$ helps suppress excited-state contamination. However, this improvement is not nearly as significant as using the optimal profile for the $\Gamma = \gamma_i$ operator alone. This further highlights the benefit of using the optimal profile. Keep in mind the $\Gamma = \nabla_i$ operator by itself with standard distillation was shown to not be a particularly good choice for the ground state of this channel and this most likely affects how much its inclusion in the 2×2 GEVP will help.

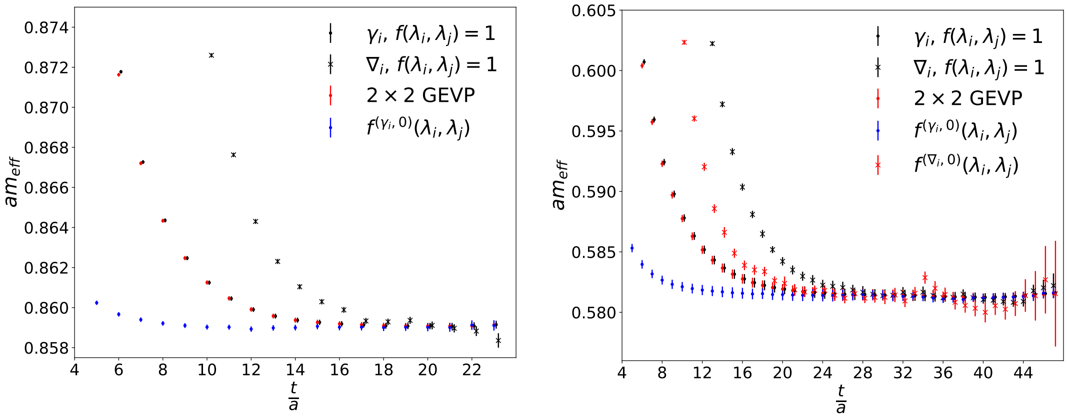

(A) In ensemble Em1.

(B) In ensemble Nm1.

FIGURE 3.19: Effective masses for the ground state of the T_1^{--} channel using the iso-vector operators $\Gamma = \gamma_i$ with standard distillation, $\Gamma = \nabla_i$ with standard distillation, the optimal linear combination of the two as dictated by the GEVP and $\Gamma = \gamma_i$ with its optimal profile.

The next step is to introduce the 7 meson profiles for each of the two Γ operators, which turns the 2×2 correlation matrix into a 14×14 one. Since this matrix involves the correlations between all possible profiles for the two Γ operators it is expected to yield better results than if only one Γ operator is used. Not only the degree of freedom of the profile is exploited but also the spatial properties of the different Γ operators. The resulting effective mass from solving the corresponding GEVP, together with the one obtained from using $\Gamma = \gamma_i$ with its optimal profile can be seen in Fig. 3.20. A slight suppression of excited-state contamination can be seen at early times from the inclusion of the $\Gamma = \nabla_i$ operator with a corresponding profile. There is a clear improvement, graphically seen to be larger than the one from including $\Gamma = \gamma_i$ and $\Gamma = \nabla_i$ in a 2×2 correlation matrix, indicating that one certainly gains something when including the $\Gamma = \nabla_i$ operator with the 7 basis profiles. However it is not nearly as significant as the improvement obtained when comparing the case of standard distillation with $\Gamma = \gamma_i$ with the optimal profile. For these operators this is not unexpected since the operator ∇_i both with standard distillation and with its optimal profile did not grant particularly good access to the ground state. This can be seen from the values of the corresponding fractional overlaps in Table 3.4. On the other hand, the $\Gamma = \gamma_i$ operator in both cases has a relatively high fractional overlap. This indicates that the not so suitable $\Gamma = \nabla_i$ operator is not the best choice to significantly improve on the $\Gamma = \gamma_i$ operator. Larger improvements might be achieved by including other operators with better individual overlaps with the ground state however this is already evidence of the advantage from extending the method of optimal profiles to multiple Γ operators. As a final result for this channel one can also look at the first excited state obtained from mixing the $\Gamma = \gamma_i$ and $\Gamma = \nabla_i$ operators with and without the optimal profiles. The resulting effective masses can be seen in Fig. 3.21, together with the second excited state obtained from the combination of both Γ operators using the corresponding optimal profile. The first thing to note is that the effective masses from the 2×2 GEVP involving operators $\Gamma = \gamma_i, \nabla_i$ is considerably higher than the ones yielded by $\Gamma = \gamma_i$ with its optimal profile and the combination of $\Gamma = \gamma_i, \nabla_i$ with its corresponding optimal profile. They are also consistent with the mass of the second excited state from the combination of $\Gamma = \gamma_i, \nabla_i$ with the optimal profile. This indicates this 2×2 GEVP misses the first excited state and only accesses the second one and the reason is not clear. Since the ground state effective masses from the 2×2 GEVP are almost identical to the $\Gamma = \gamma_i$ operator alone then the next excited state is most likely dominated by the ∇_i operator which, without an optimal profile, might have a large overlap with the second excited state that the GEVP with both Γ operators and profiles see. The second thing is the effective masses of the first excited state from the expanded GEVP are almost identical within errors to the first excited state of the $\Gamma = \gamma_i$ operator alone with the corresponding optimal profile. This supports the idea that the $\Gamma = \nabla_i$ contributes mostly to higher excited states and only very slightly to this first excitation even with an optimal profile.

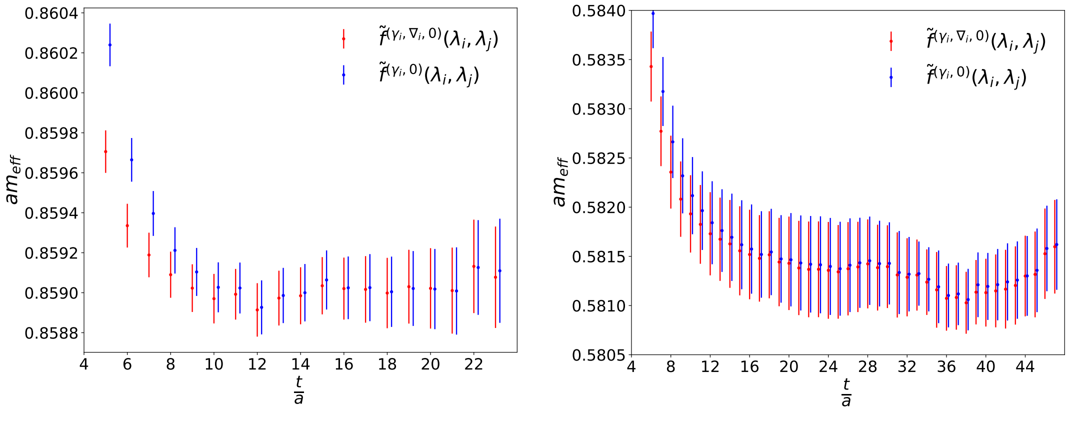

(A) In ensemble Em1.

(B) In ensemble Nm1.

FIGURE 3.20: Effective masses for the ground state of the T_1^{--} channel using the iso-vector operator $\Gamma = \gamma_i$ with its optimal profile and a linear combination of the operators $\Gamma = \gamma_i, \nabla_i$ with its corresponding optimal profile.

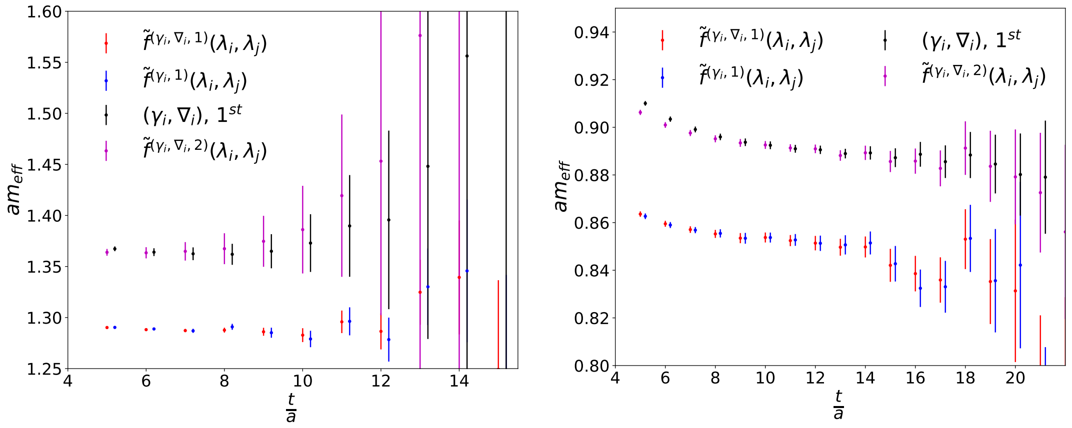

(A) In ensemble Em1.

(B) In ensemble Nm1.

FIGURE 3.21: Effective masses for the first excited state of the T_1^{--} channel using the iso-vector operator $\Gamma = \nabla_i$ with its optimal profile, an optimal linear combination of the operators $\Gamma = \gamma_i, \nabla_i$ with its corresponding optimal profile and an optimal linear combination of the operators $\Gamma = \gamma_i, \nabla_i$ with standard distillation.

3.4.5.4 Optimal meson distillation profiles

The optimal meson distillation profiles for the different operators studied in this work can be built as shown in Eqn. (3.18). Fig. 3.22 displays the ground state optimal profiles for the local Γ operators and Fig. 3.23 displays the ones of the first excited state for these same operators. The first feature seen is that none is a constant which would be the case for standard distillation. This further supports the observation that an orthogonal projection onto the range of the chosen Laplacian eigenvectors is not the optimal way to build meson operators with good overlap with the low energy eigenstates. A second feature of these profiles is the lack of nodes in the ground state profiles and the presence of one in the profiles corresponding to the first radial excitations. This points to the need of introducing structure in the space of the Laplacian eigenvalues and therefore, as will be seen later, in coordinate space to better resemble the wanted energy eigenstates. A third feature is while all profiles shown retain a suppression of larger eigenvalues the ones corresponding to the first radial excitations still allow for non-negligible contributions from larger eigenvalues in comparison to the ground states. This suggests higher energy states require more eigenvectors. A fourth feature is both cases exhibit non-zero contributions from the largest eigenvalue so if one increased the value of N_v these additional vectors would still contribute to the optimal meson operator. Finally, a distinction can be made between the profiles of the $\Gamma = \gamma_5, \gamma_i$ and $\Gamma = \mathbb{I}, \gamma_5\gamma_i, \epsilon_{ijk}\gamma_j\gamma_k$ operators based on both their general shape and the degree of suppression of higher eigenvalues, with the latter suppressing the higher eigenvalues less than the former. Whether this distinction is related to the S- and P-wave classification of the J^{PC} in the quark model remains to be confirmed, however the free-field explanation presented in [50] for states with larger L requiring contributions from eigenvectors with higher eigenvalues would favor this connection.

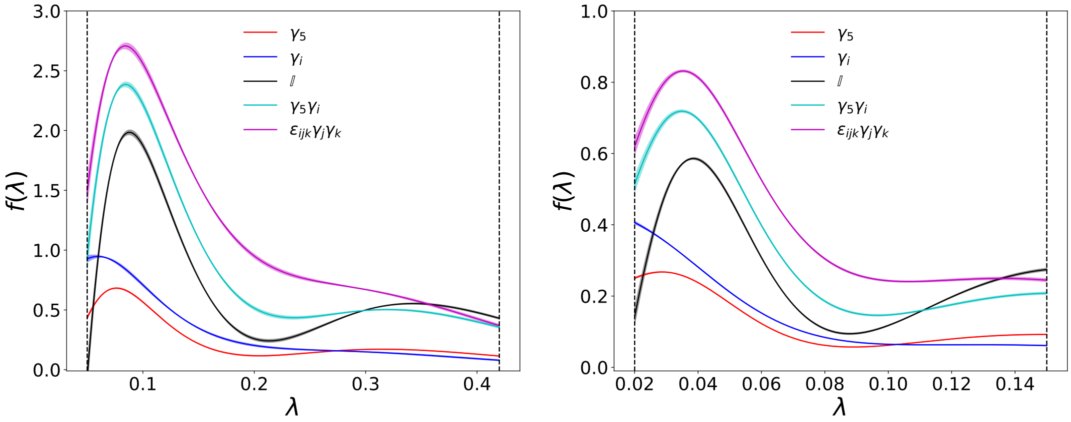

(A) In ensemble Em1.

(B) In ensemble Nm1.

FIGURE 3.22: Optimal meson distillation profiles for the ground state of the local Γ operators.

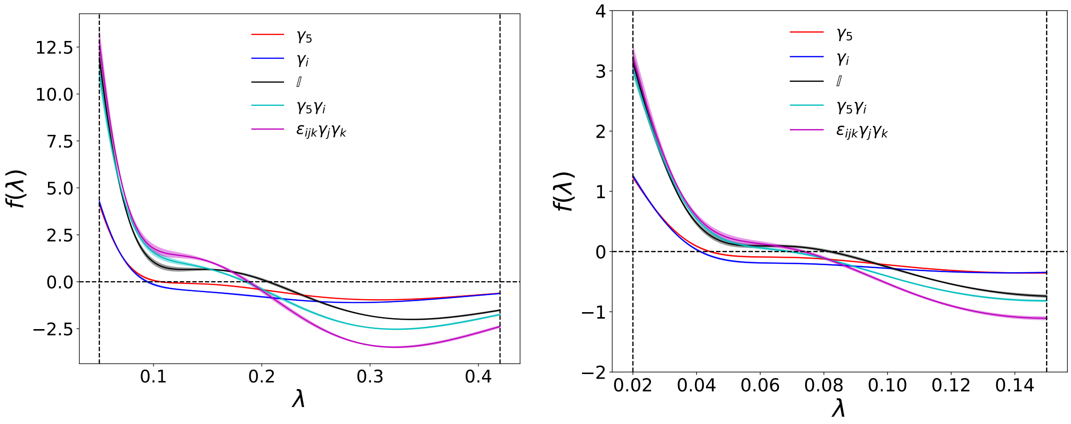

(A) In ensemble Em1.

(B) In ensemble Nm1.

FIGURE 3.23: Optimal meson distillation profiles for the first excited state of the local Γ operators.

For the derivative-based operators the relevant optimal profiles are a function of two eigenvalues λ_i and λ_j, unlike the local operators where only the case $\lambda_i = \lambda_j$ is relevant. Fig. 3.24 shows the optimal profile for the ground state of the $\Gamma = \mathbb{Q}_{ijk}\gamma_j\nabla_k$ and $\Gamma = |\epsilon_{ijk}|\gamma_j\nabla_k$ operators from the E^{++} and T_2^{++} irreps in ensemble Em1. Both display a preference for small eigenvalues while larger ones are relatively suppressed in an approximately radially symmetric manner, consistent with the profiles of the ground state of the local operators. These same profiles were found to be qualitatively identical in the Nm1 ensemble and therefore the latter are not shown. Fig. 3.25 shows the optimal profile for the first excited state of these same operators in ensemble Em1, where the presence of an approximately radially symmetric node can be seen, again in agreement with the local operators. Further examples of derivative-based Γ operators are shown in Fig. 3.26 which display these same features, suggesting tthe approximately radial suppression of eigenvalues and pattern of nodes is present along the different operators as for the local Γ operators.

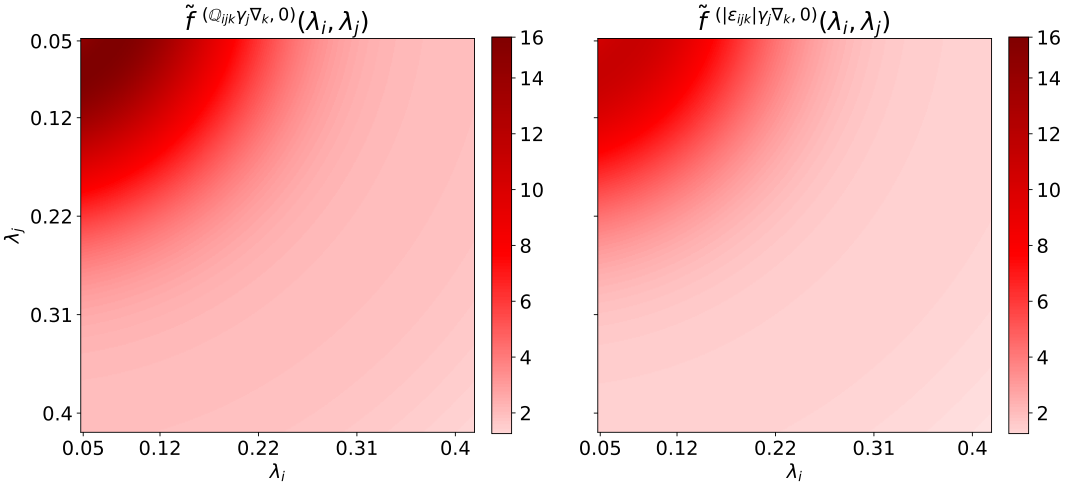

FIGURE 3.24: Optimal meson distillation profiles for the ground state of the $\Gamma = \mathbb{Q}_{ijk}\gamma_j\nabla_k, |\epsilon_{ijk}|\gamma_j\nabla_k$ operators in ensemble Em1.

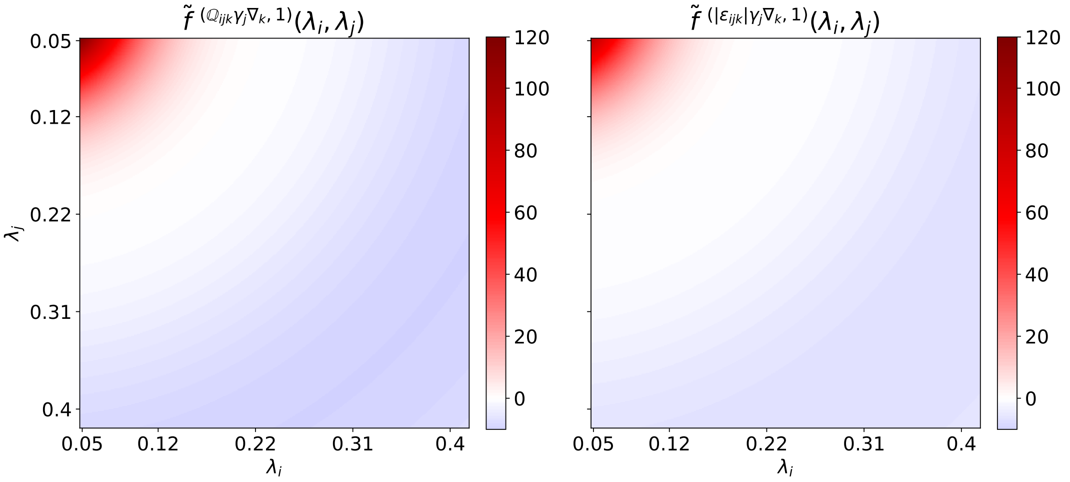

FIGURE 3.25: Optimal meson distillation profiles for the first excited state of the $\Gamma = \mathbb{Q}_{ijk}\gamma_j\nabla_k, |\epsilon_{ijk}|\gamma_j\nabla_k$ operators in ensemble Em1.

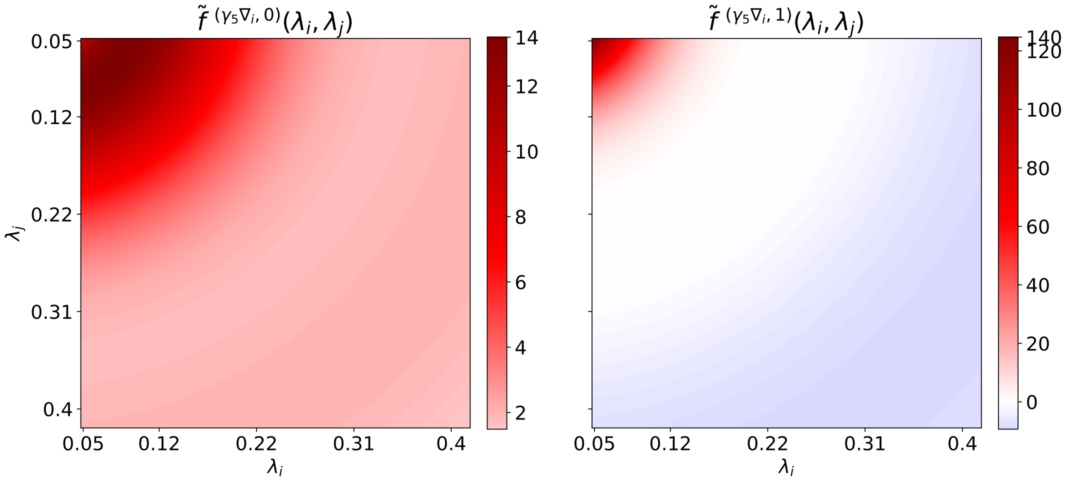

FIGURE 3.26: Examples of optimal profiles for derivative-based Γ operators in ensemble Em1.

3.4.5.5 Spatial profiles via the optimal meson distillation profiles

The spatial profiles of the corresponding optimal meson operators built via the optimal meson distillation profiles are shown in Eqn. (3.27). It is worth remembering this is done only for the operators which correspond to spin-singlets in the quark model and have a γ_5 as the only spin structure in their definition, i.e $\Gamma = \gamma_5$ and $\Gamma = \gamma_5\nabla_i$ which correspond to 0^{-+} and 1^{+-}. The 3D point-source used is set at $\vec{z} = (12a, 12a, 12a)$ for ensemble Em1 and $\vec{z} = (24a, 24a, 24a)$ for ensemble Nm1. The spatial profiles for the ground and first excited states of the $\Gamma = \gamma_5$ operator are shown in Fig. 3.27 for both ensembles calculated in a single gauge configuration. The ground states display a radially symmetric decay while the first excited states show a radially symmetric node, hinting at a more complex spatial structure. Both features are consistent with the expected S-wave behavior as well as with the wave functions calculated in [121]. It is clear that ensemble Nm1 provides a better resolution for the spatial profiles in both cases thanks to the smaller lattice spacing and larger physical volume. The latter is particularly important, since one can see the first excited state is better contained in this lattice and therefore finite-volume effects are more under control.

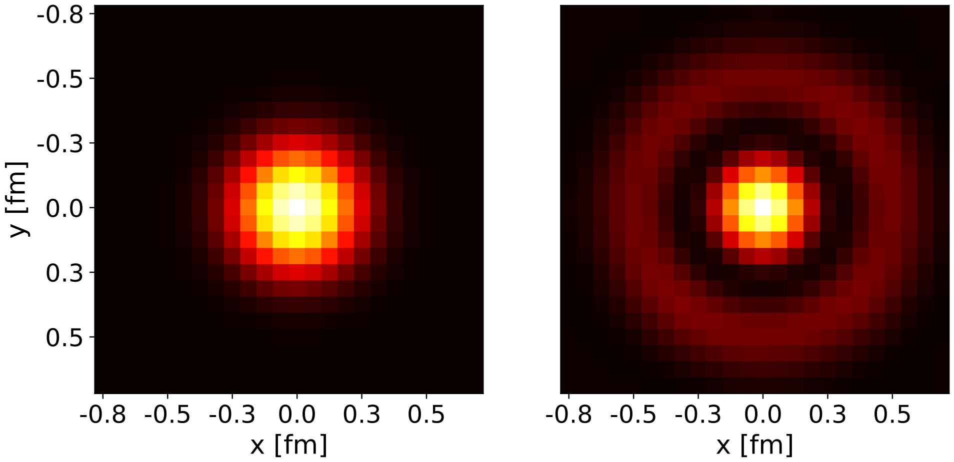

(A) In ensemble Em1.

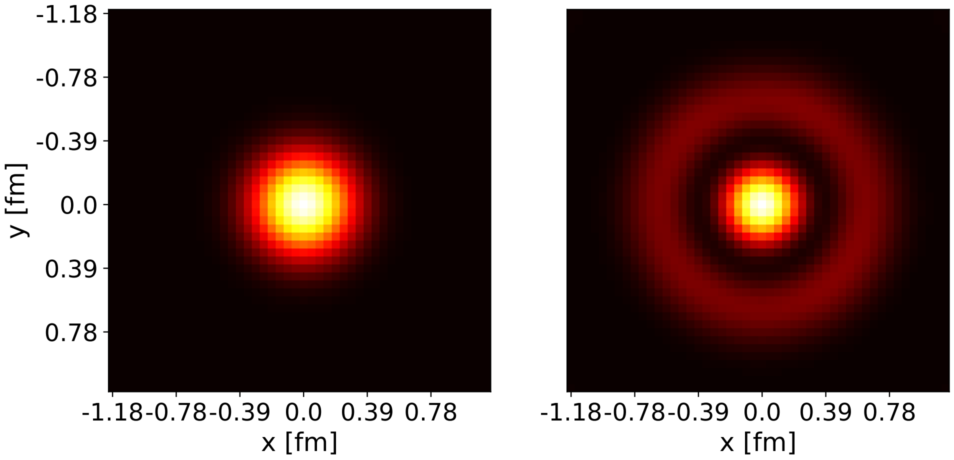

(B) In ensemble Nm1.

FIGURE 3.27: Spatial profiles for the ground and first excited states of the iso-vector $\Gamma = \gamma_5$ operator

The spatial profiles for ground and first excited state of the $\Gamma = \gamma_5 \nabla_i$ operator for both ensembles are displayed in Fig. 3.28 calculated in a single gauge configuration where a fixed direction was chosen for the derivative. The dumbbell-like structure expected from a P-wave behavior is clearly observed along the direction of the derivative. The inclusion of the optimal profile for the first excited state introduces additional non-trivial spatial structure along the y direction which is non-negligible close to the boundaries. Just as for the S-waves, the larger physical volume and smaller lattice spacing of ensemble Nm1 leads to a better-contained spatial profile. While it is likely that finite-volume effects are present in both ensembles for the first excited state, they are less significant in the Nm1 case. Further study of the spatial profiles is beyond the scope of this work, which provides a first test of their construction, yet it could be interesting to gain insight on spatial properties of these states. Aspects such as finite-volume effects, spatial extent of the different states and non-trivial spatial structure can be studied through these profiles to better understand the states created by the optimal profiles and how they better approximate the energy eigenstates.

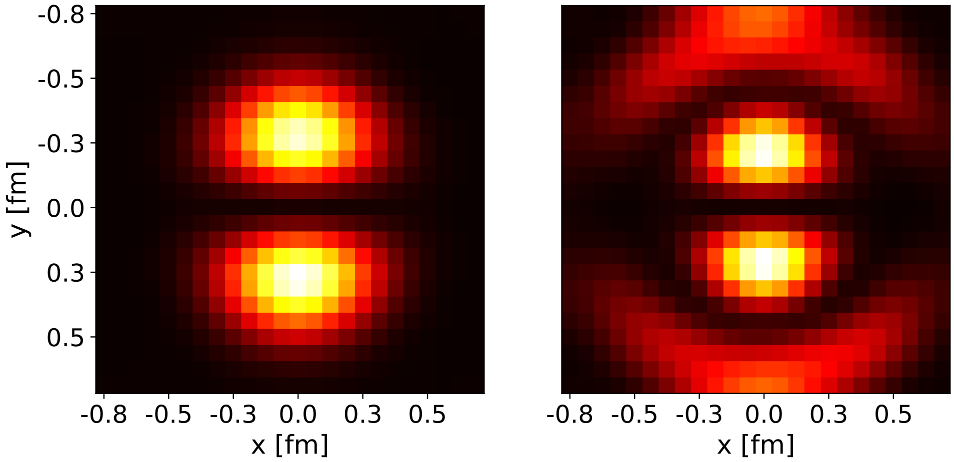

(A) In ensemble Em1.

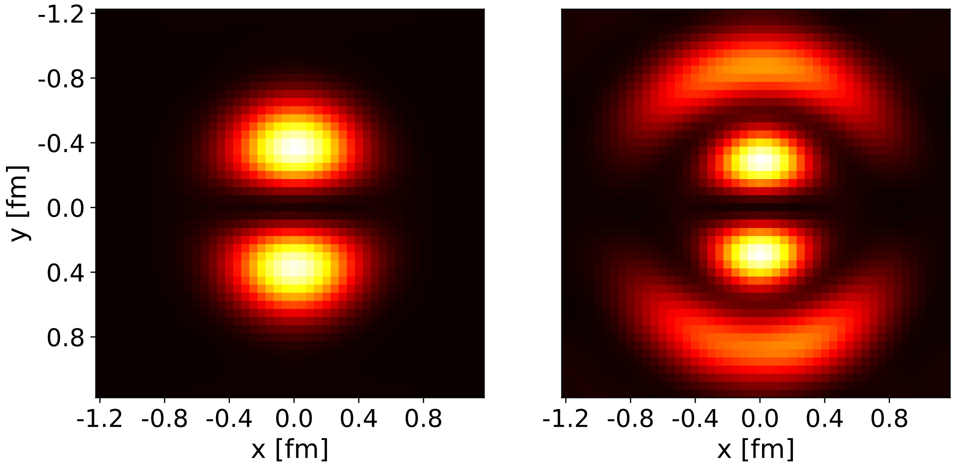

(B) In ensemble Nm1.

FIGURE 3.28: Spatial profiles for the ground and first excited states of the iso-vector $\Gamma = \gamma_5 \nabla_i$ operator

Chapter 4

Disconnected contributions and charmonium-glueball mixing

Until now this work has focused on using mesonic operators for the study of the different symmetry channels, however this is not the complete picture of such states. Iso-scalar operators that depend only on the gauge links with no explicit quark degrees of freedom can be built for each symmetry channel and are a first step to a lattice study of *glueballs*, color-singlet bound states of gluons with integer J expected to exist in QCD due to the self-coupling of the gauge field [5, 8]. In this work these gluonic operators are built from spatial Wilson loops, i.e products of link variables along a closed path involving only displacements in the spatial directions, while other types of operators can be found in [11]. Further details about lattice studies of glueballs can be found in [127]. Such gluonic operators can in principle mix with iso-scalar mesonic operators and this can shed some light on the nature of the energy eigenstates. This mixing in the Em1 and Nm1 ensembles is the main topic of this chapter and is calculated. These ensembles are a convenient testing ground for this since the absence of light quarks means that any possible mixing with glueballs is restricted to the charmonium states. Nonetheless, there are difficulties related to both kinds of iso-scalar operators involved which will also be explained.

4.1 Iso-scalar charmonium spectrum

The starting point is the calculation of the iso-scalar charmonium spectrum in ensembles Em1 and Nm1. The steps of this calculation, including the determination of the optimal profiles for the different channels, are identical to the ones presented in Chapter 3 except now the disconnected contributions have to be taken into account to build the different temporal correlation functions. The temporal correlation function for a meson operator is given by

$$\begin{aligned} C(t) = & \langle -Tr\left(\Phi[t]\tau[t,0]\bar{\Phi}[0]\tau[0,t]\right)\rangle_U \\ & + N_f \left\langle Tr\left(\Phi[t]\tau[t,t]\right) Tr\left(\bar{\Phi}[0]\tau[0,0]\right)\right\rangle_U , \end{aligned} \tag{4.1}$$

where again $N_f = 2$ for Em1 and Nm1. The difference to the iso-vector correlation function is given by the second term in Eqn. (4.1) and the product of traces involved comes from the quark-anti-quark annihilation at times 0 and t, leading to the name "disconnected" contributions. For the case of the correlation matrix relevant for the

GEVP formulation the expression is given by

$$\begin{aligned} C_{ij}(t) &= \left\langle -Tr\left(\Phi^{(i)}[t]\tau[t,0]\bar{\Phi}^{(j)}[0]\tau[0,t]\right)\right\rangle_U \\ &\quad + N_f \left\langle Tr\left(\Phi^{(i)}[t]\tau[t,t]\right) Tr\left(\bar{\Phi}^{(j)}[0]\tau[0,0]\right)\right\rangle_U . \end{aligned} \tag{4.2}$$

Although the calculation is not much more complicated than in the iso-vector case, the main problem is that the disconnected pieces have a notorious signal-to-noise problem compared with the connected ones and therefore the combination of both in a sum gets lost in noise at very early times. The absolute error of the the disconnected contribution is expected to remain approximately constant just like in glueball correlation functions [128, 129]. Furthermore, the disconnected contribution is considerably smaller than the connected contribution in magnitude. This comes from the OZI rule which indicates that processes with an intermediate step containing only gluons are strongly suppressed [5]. Finally, this contribution requires the calculation of the perambulator $\tau[t,t]$ for all values of time t (or terms of the form $Tr\left(\Gamma D^{-1}[t,t]\right)$ when distillation is not used), which leads to a considerably larger computational cost. For these reasons this disconnected contribution has often been neglected, motivated as well by the $1-4$ MeV mass difference between iso-scalar and iso-vector pseudo-scalar obtained in [16]. Nonetheless ignoring this contribution is not entirely correct for a number of reasons. First of all, the argument based on the OZI rule is tied to the running coupling of QCD and therefore depends on the energy scale at which the processes occur. Second of all, neglecting the disconnected contribution neglects as well the possible mixing with glueball states that can significantly shift the iso-scalar mass [16]. Finally, hadron spectroscopy calculations are reaching considerably precision such that differences of the order of 5 MeV are significant. Recent studies including the disconnected contribution by looking at the hyperfine mass splitting in charmonium either indirectly [17] or directly [18] agree the mass of the pseudo-scalar is increased by around $3-7$ MeV while the vector mass is not significantly affected. Furthermore, this increase disagrees with the decrease predicted by non-relativistic QCD perturbation theory [17, 19], which further motivates a careful study.

There is a clear motivation to apply the optimal distillation profiles to study the iso-scalar charmonia spectrum; the resulting suppression of excited state contamination at early times can in turn lead to an earlier mass plateau where the signal-to-noise problem is not yet too pronounced. The channel to be analyzed first corresponds to A_1^{-+} and this will be done using the $\Gamma = \gamma_5$ operator since it displayed the best results for the iso-vector case in both Em1 and Nm1 ensembles. Fig. 4.1 shows the ground state effective masses obtained using both standard distillation and the optimal profiles in ensembles Em1 and Nm1 using $t_G = 2$. Two main features can be observed in these results. First, the use of distillation allows to observe a non-negligible splitting between the iso-scalar and iso-vector effective masses which is yet another advantage of using this framework. Second and most importantly for this work, the use of the corresponding optimal profile leads to a suppression of excited-state contamination at early times just as for the iso-vector channels. Third, in both ensembles there is an upwards shift in the mass from the iso-vector case to the iso-scalar case, which agrees in sign with other results in the literature [17, 18]. Table 4.1 shows the resulting plateau average masses for the iso-scalar (I-S) and iso-vector (I-V) $\Gamma = \gamma_5$ operators for comparison, the improvement of the fractional overlap for the former case when the optimal profile is used and the mass difference between the two in MeV. Both values of the mass difference are considerable larger than the 7 MeV and 4 MeV presented in [17, 18], which can be due mainly to model differences such as number of flavors and masses of the quarks. Nonetheless, the measured differences and the improvement of the fractional overlaps indicate that the optimal profiles are a useful tool to do this kind of measurement thanks to the suppression of excited-state contamination at early times when the disconnected signal is the most useful.

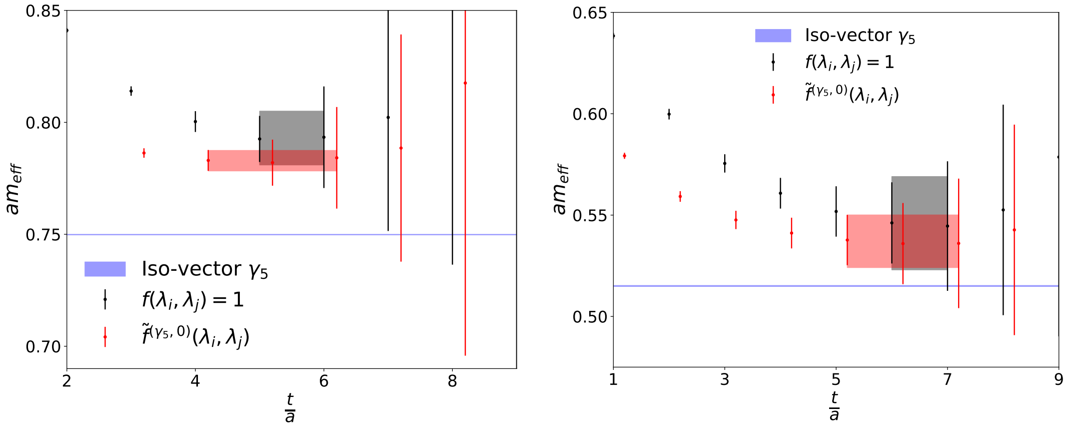

(A) Effective masses in ensemble Em1.

(B) Effective masses in ensemble Nm1.

FIGURE 4.1: Ground state effective masses for the iso-scalar $\Gamma = \gamma_5$ using standard distillation and the optimal profile in the Em1 and Nm1 ensembles. The blue bands indicate the plateau average of the corresponding iso-vector channel for comparison.

Ensemble	am_{I-S}	am_{I-V}	I-S Fractional Overlap	Δm_{I-S}
Em1	0.7829(46)	0.749862(83)	0.926(30) → 0.9849(64)	98(14)
Nm1	0.537(13)	0.51503(21)	0.900(63) → 0.964(28)	89(53)

TABLE 4.1: Plateau average masses and fractional overlaps of the iso-scalar $\Gamma = \gamma_5$ operator in ensembles Em1 and Nm1. The physical values of the splitting Δm_{I-S} are given in MeV.

The next channel is A_1^{++}, studied with the $\Gamma = \mathbb{I}$ operator. Fig. 4.2 shows the ground state effective masses obtained using both standard distillation and the optimal profiles in ensembles Em1 and Nm1. Unlike the A_1^{-+} case, the mass shift from iso-vector to iso-scalar is negative and significantly large. This same figure includes the effective masses for the first excited state of the iso-scalar channel, which in both ensembles is very close to the ground state of the iso-vector channel. A rather interesting feature is while the effective masses from the optimal profile display the expected suppression of excited-state contamination, they also display significantly larger errors when compared to standard distillation. A partial explanation for this can be seen from Fig. 4.3, which shows the effective masses obtained from the diagonal entries of the original 7×7 correlation matrix in the Em1 case. The masses from the first two Gaussian widths $\sigma_{1,2}$ display the least contamination at early times but also the largest errors, so it makes sense that the result from the optimal profile will exhibit a very similar pattern; these noisier but better operators are preferred, although the others probably contribute but less significantly. These two widths also correspond to the smallest ones of the original basis, which could indicate that the state particularly favors smaller eigenvalues. Nonetheless, the effective masses from standard distillation and the wider profile appear to eventually reach the correct mass at later values of time and with smaller errors, indicating that contributions from larger eigenvalues are not negligible. These two considerations together suggest a highly non-trivial structure in distillation space, which will be observed when looking at the corresponding optimal profiles. It also suggests the basis of Gaussian profiles that has worked well until now might not be the best choice for this particular channel in terms of the resulting error. This opens the door to future work focused on improving the choice of basis profiles. As a final note, the case of the T_1^{--} did not display a significant signal in either ensemble for the iso-scalar $\Gamma = \gamma_i$ operator.

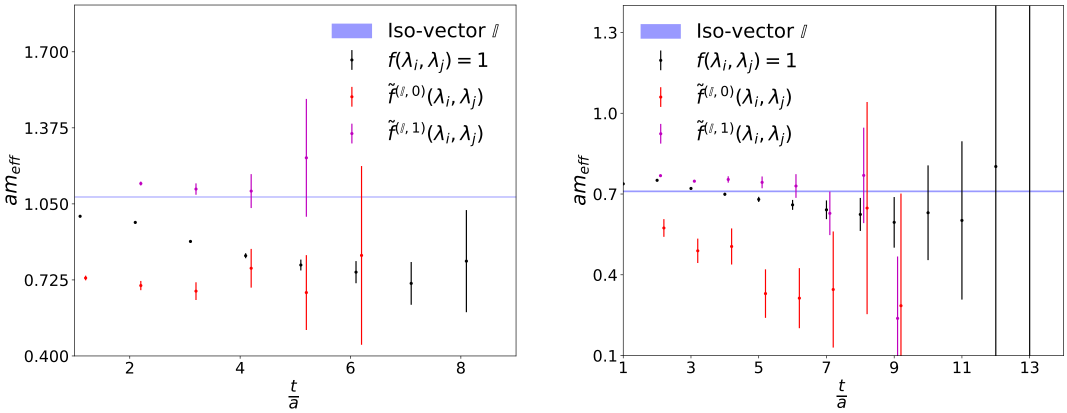

(A) Effective masses in ensemble Em1.

(B) Effective masses in ensemble Nm1.

FIGURE 4.2: Effective masses for the iso-scalar $\Gamma = \mathbb{I}$ using standard distillation and the optimal profile in the Em1 and Nm1 ensembles. The blue bands indicate the plateau average of the corresponding iso-vector channel for comparison.

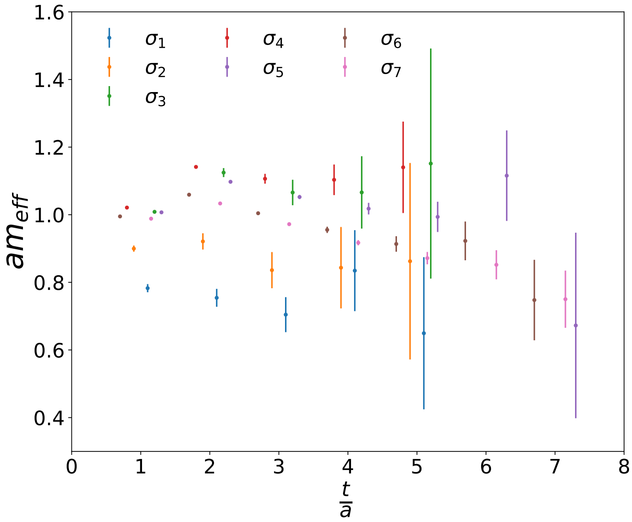

FIGURE 4.3: Ground state effective masses from the diagonal entries of the 7×7 correlation matrix using the iso-scalar $\Gamma = \mathbb{I}$ operator in ensemble Em1.

4.1.1 Optimal meson distillation profiles

Just as for the iso-vector operators, the optimal meson profiles can be determined for the different iso-scalar operators studied here. Fig. 4.4 displays the ground state optimal meson distillation profiles for the $\Gamma = \gamma_5$ operator in both iso-scalar (I-S) and iso-vector (I-V) cases for both ensembles. For comparison all profiles are normalized to $f(\lambda_1) = 1$. For each ensemble there is similarity between the shapes of the profiles for the iso-vector and iso-scalar cases, including the absence of nodes. The proximity between the masses of the two states is a possible explanation. In [120] the optimal profile obtained for the iso-vector was used to calculate the mass of the iso-scalar and the result is very similar to the one displayed in Fig. 4.2a, which supports the idea that similar masses entail similar profiles. This idea can be further tested by looking at the optimal profiles of the A_1^{++} channel which are displayed in Fig. 4.5 for Em1. The ground state iso-scalar (I-S) profile displays a single node, unlike the ground state of the iso-vector (I-V). Furthermore, the latter is more similar to the first excited state I-S profile, which explains why the effective masses are consistent with each other. These observations indicate that a meson state needs a rather non-trivial structure to have good access to the desired ground state which, as will be shown later, has a non-negligible contribution from purely gluonic operators. A very similar behavior was observed for the Nm1 case.

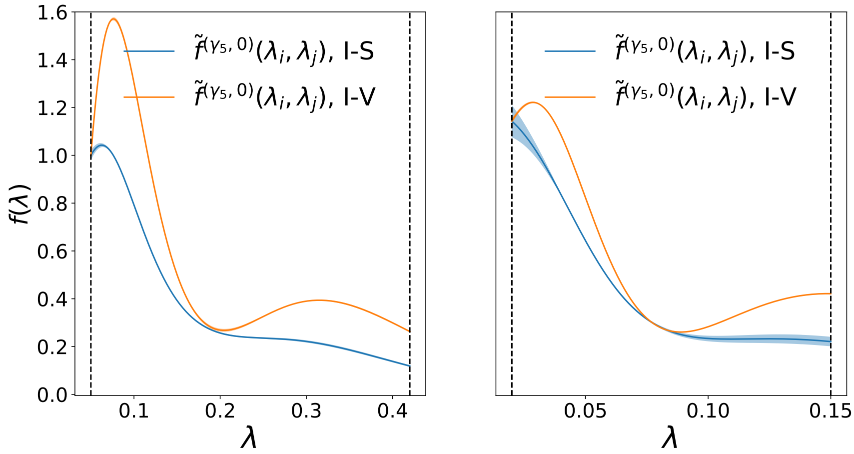

FIGURE 4.4: Optimal meson distillation profiles for the ground state $\Gamma = \gamma_5$ operator in ensembles Em1 (left) and Nm1 (right) for the iso-scalar (I-S) and iso-vector (I-V) channels. All profiles are normalized to start at 1.

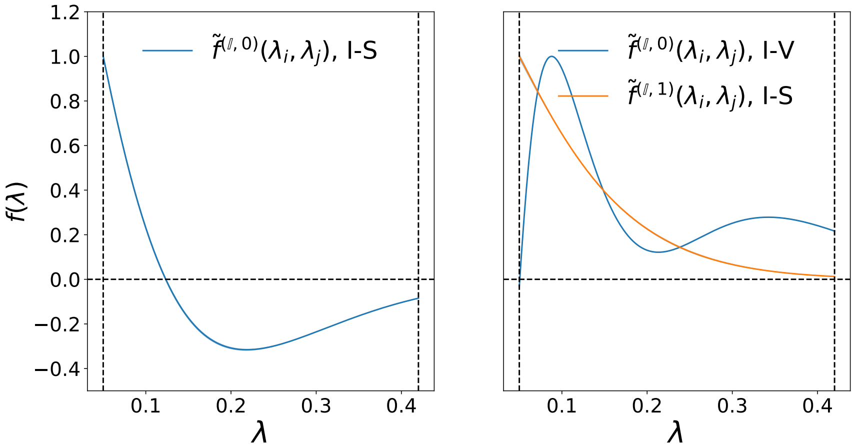

FIGURE 4.5: Optimal meson distillation profiles for the ground and first excited state for the $\Gamma = \mathbb{I}$ operator in ensemble Em1. The ground state iso-vector (I-V) profile is more similar to the first excited state iso-scalar (I-S) profile.

4.2 Gluonic spectrum

4.2.1 Gluonic operators from spatial Wilson loops

Gluonic operators at zero spatial momentum can be built from spatial Wilson loops of a given shape by projecting them onto an irrep R of the cubic group with fixed parity P and charge conjugation C symmetries as shown in [130]. This leads to the expressions

$$G_{k,i}^{R^{\pm+}}(t) = \frac{1}{N_L^3}\sum_{\vec{x}}\sum_{n=0}^{23} c_n^{(R,k,i)}\,\mathrm{Re}\left\{Tr\left(W_n(\vec{x},t) \pm W_n^p(\vec{x},t)\right)\right\} \tag{4.3}$$

$$G_{k,i}^{R^{\pm-}}(t) = \frac{1}{N_L^3}\sum_{\vec{x}}\sum_{n=0}^{23} c_n^{(R,k,i)}\,\mathrm{Im}\left\{Tr\left(W_n(\vec{x},t) \pm W_n^p(\vec{x},t)\right)\right\}, \tag{4.4}$$

where $c_n^{(R,k,i)}$ are the projection coefficients to "row" i of copy k of irrep R, $W_n(\vec{x},t)$ is the Wilson loop at $(\vec{x},t)$ with shape W_n given by applying group element g of the cubic group to a fixed original shape W, e.g the 1×1 plaquette in a fixed plane, and W_n^p is its parity twin. Not every shape has non-zero contributions in a given irrep R^{PC} and the irreducible content of shapes of lengths 4, 6 and 8 can be found in [130], together with the method to calculate the irreducible content of shapes of larger length. This method was implemented in a Python code to reproduce the irreducible contents presented in that reference as well as to be able to do the same for longer loop shapes not presented there.

To intuitively understand how glueball operators can be built from these loops it is useful to consider two simple examples. First, the A_1^{++} irrep. Here one demands the operator remains invariant under all elements of the cubic group as well as under parity and charge conjugation. Such an operator can be built from the 1×1 plaquette. By acting on it with any element of the cubic group one simply changes the plane in which the plaquette is located. An example of such a transformation is shown in Fig. 4.6; after the transformation the shape is conserved and only the plane where it lives changed. By acting on the original plaquette with all elements of the cubic group one ends up with 24 plaquettes. Since the group is closed under its product, applying any group element to any of these 24 plaquettes will turn it into another one of this same set. It is clear that the sum of the 24 plaquettes is invariant under the action of the cubic group. Here one sets the projection coefficients as $c_n^{A_1,1,1} = 1$ in the definition of the projected glueball operators although of course there is a freedom of normalization. The next step is to fix the parity symmetry. In the graphical representation of the plaquette, a parity transformation amounts to performing every displacement in the negative direction. The parity-projected $A_1^\pm$ glueball operator is the sum of the 24 plaquettes plus or minus the sum of the 24 parity transformed plaquettes depending on the choice of $P = \pm$. Fig. 4.7 shows the parity-transformed plaquette from Fig. 4.6 as well as the original plaquette transformed by a particular element of the cubic group. In the case of the plaquette one of the group elements transforms it in the same way as a parity transformation does. This means the difference between the sum of the 24 plaquettes and the sum of the 24 parity-transformed plaquettes will be 0 while the sum of the two will not. The former result shows one cannot build a non-trivial operator that transforms as A_1^- from the plaquette. Finally, for the charge conjugation symmetry one needs to add or subtract both orientations of each plaquette, however this can be shown to be equivalent to taking the real or imaginary part of the trace which defines the glueball operator. For the plaquette only the projection to A_1^{++} gives a non-trivial operator and other choices of parity and charge conjugation symmetries in A_1 will not. An example on how to project the plaquette onto the two-dimensional E^{++} irrep can be found in [26].

The second example is one which grants access to the A_1^{-+} irrep; the "hand". This shape is shown in Fig. 4.8 together with its parity-transformed version, the latter which cannot be obtained by applying any cubic transformation to the former. By adding up all 24 transformations of the "hand", subtracting from each one of them its parity twin and extracting the real part of the trace one can build a non-trivial glueball operator that transforms as A_1^{-+}. In practice it would be very unpractical to do a trial-and-error approach by taking every shape and applying the projector onto all irreps of interest to it. The standard approach to avoid this is to form a representation of the cubic group extended to include parity for each choice of shape with fixed charge conjugation symmetry, i.e see how the shape transforms under the action of the extended cubic group and build the corresponding matrices that represent these transformations [130]. The resulting representation can be expressed as a direct sum of the irreps R^P. If a given R^P does not explicitly appear in this decomposition then one cannot build a non-trivial glueball operator which transforms like R^{PC} just by using the chosen shape with fixed charge conjugation symmetry C. One then applies the projectors of the R^P that appear explicitly in the decomposition to the chosen shape. A way of building the projection coefficients for all irreps R is also presented in [130].

(A) The plaquette in a fixed plane.

(B) The plaquette under the action of one of the cubic transformations.

FIGURE 4.6: Example of the action of the cubic group on the plaquette. The red dot denotes the starting point and the first link is marked black for clarity.

(A) The original plaquette under the action of a chosen cubic transformation.

(B) The plaquette under the action of the parity transformation.

FIGURE 4.7: Equivalence between parity transformation and one of the cubic transformations for the plaquette.

(A) The "hand" Wilson loop.

(B) The "hand" under the action of the parity transformation.

FIGURE 4.8: The "hand" Wilson loop and its parity-transformed version.

One needs shapes of length at least 8 to simultaneously access the irreps A_1^{++}, A_1^{-+}, E^{++} and T_2^{++} which are of interest for this work, which is why the 5 shapes shown in [130] are used. Additionally, the Cayley-Hamilton theorem guarantees that the single and double winding of a fixed shape yield independent operators, which allows to straightforwardly double the number of available operators [14]. Furthermore, the same shape with double the length can also be easily built to again double the number of operators. These last two considerations lead to Wilson loops involving up to 32 link variables. Since longer products of link variables are expected to have larger statistical fluctuations only the ones with the smallest noise will be considered for calculating correlation functions. Finally, to further increase the number of available operators for a GEVP and reduce short-range fluctuations the APE smearing described in Section 2.2.4 is used to smear the link variables before measuring the Wilson loops. Low-statistics studies with different APE parameters yielded $\alpha_{APE} = 0.35$ and $N_{APE} = 5, 10, 15, 20$ as a good choice for ensemble Em1. For ensemble Nm1 the same value of α_{APE} was kept but with $N_{APE} = 10, 20, 30, 40$ to take into account the larger spatial volume. All of these considerations yield a total of $2 \times 2 \times 5 \times 4 = 80$ glueball operators that can be used for a GEVP. As mentioned in [129], improving the signal-to-noise ratio of glueball correlators also improves the overlap of the created state with the wanted energy eigenstate. Because of this not all 80 available operators are put together in a single correlation matrix but rather only the ones displaying the best signal-to-noise ratio in their individual temporal correlation functions. This also avoids the inclusion of additional noise in the GEVP, which can become numerically unstable in the presence of significant noise. As a final note, it is important to keep in mind two additional complications when using Wilson loops as gluonic operators. The first one is that since smearing tends to smooth out the link variables and therefore suppress short distance fluctuations then small loop shapes can lead to very similar operators if their spatial extent is smaller or comparable to the smearing radius. This was clearly observed and commented on in [131] when using both APE smearing and the 3D Wilson flow, as such near-degeneracies can lead to numerical instabilities in the GEVP formulation. The second one is that different loop shapes can have the same leading order term in a small-a expansion as shown in [132], meaning that up to a given power of a they correspond to the same operator of a given channel in terms of the continuum field-strength tensor F_{ij} and its derivatives D_k. At small enough values of lattice spacing this can lead to yet another near-degeneracy which negatively affects the GEVP. Ways to avoid these degeneracies will be studied in future work and the signal-to-noise criterion will be used to select suitable operators for the GEVP in each channel.

4.2.2 Results in $N_f = 0$

Glueball spectroscopy in the absence of quarks has yielded a clear spectrum thanks to the absence of mixing with mesonic or other states with quarks degrees of freedom [14]. Since the spectrum is much less dense, significantly less excited-state contamination is expected in the effective masses and therefore the signal-to-noise problem is not as alarming. Furthermore, the generation of gauge configurations in this model is much cheaper since no inversions of the Dirac operator are required. This allows to work with large statistics that further improves the resulting masses. Additional strategies like the use of anisotropic lattices can also be used to improve the temporal resolution of the correlation functions, allowing to better sample the earlier physical times when the signal-to-noise problem is not as pronounced [14]. With these considerations in mind, the glueball spectrum is measured using the previously described spatial Wilson loops in the isotropic, pure gauge qE ensemble to both test the effectiveness of these operators while at the same time having a reference spectrum to compare the results that will be obtained once dynamical quarks are included. Fig. 4.9 shows the resulting ground state effective masses of the A_1^{++}, A_1^{-+}, E^{++} and T_2^{++} obtained from the spatial Wilson loops. There is a non-negligible signal for all the irreps, with the best signal being the one of the A_1^{++} glueball where excited-stated contamination is gone after $\frac{t}{a} = 0$. The masses for the E^{++} and T_2^{++} irreps are compatible until the point where the errors become too large and the ones from the A_1^{-+} are slightly above them. This hierarchy is consistent with previous pure gauge results [14]. While no mass plateaus can be reliably extracted for the E^{++}, T_2^{++} and A_1^{-+} irreps, one could argue that there is not much excited-state contamination in these masses since the difference between them at successive values of time is not large. The problematic issues with these channels are the large errors and the possible presence of cut-off effects due to the relatively large values of the effective masses in lattice units. Nonetheless, the hierarchy of states, the small presence of excited-state contamination and the clear signal for the A_1^{++} channel are the benchmarks of comparison for the results that will be obtained using the same gluonic operators in the presence of dynamical quarks.

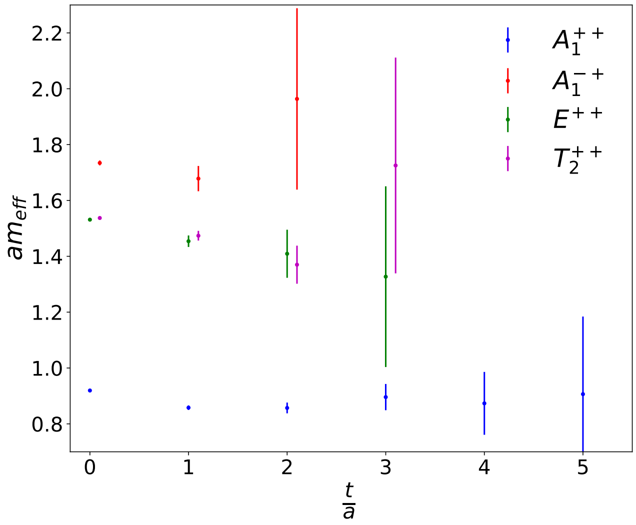

FIGURE 4.9: Ground state effective masses of the 4 irreps of interest in the qE ensemble.

4.2.3 Results in $N_f = 2$

The gluonic operators are measured in the Em1 and Nm1 ensembles to extract the corresponding glueball masses for the A_1^{++}, A_1^{-+}, E^{++} and T_2^{++} channels. Given that these measurements are vastly cheaper than the ones for the meson operators they are done in a larger number of gauge configurations, namely $\approx 12 \times 10^3$ in Em1 and 982 in Nm1. The resulting ground states for the different channels of interest are displayed in Fig. 4.10. The lightest channel in both ensembles, which also has the clearest signal for the effective mass, is A_1^{++}, yielding a plateau average value of $am = 0.652(25)$ for Em1 and $am = 0.567(36)$ for Nm1. These values are in relatively good agreement with the ones obtained from the iso-scalar $\Gamma = \mathbb{I}$ previously measured, indicating that both gluonic and mesonic operators are granting access to the same state. This agreement further motivates the study of the mixing between these types of operators. The obtained spectrum can also be compared to the one obtained in the qE ensemble, i.e in a pure gauge setup. In both cases, pure gauge and $N_f = 2$, the A_1^{++} effective masses display the clearest signal and smallest excited-state contamination. This is particularly true when comparing the qE and Em1 ensembles. This serves as further indications that this channel can have a significant gluonic contribution. Furthermore, the hierarchy of states observed in the qE ensemble is not the same as in the Em1 and Nm1 ensembles, where the A_1^{-+} effective masses tend to lie below the ones of the E^{++} and T_2^{++} irreps. This is expected, since now the gluonic operators couple to the iso-scalar states which are not pure glueballs. In particular, the iso-scalar A_1^{-+} was observed to be slightly above the iso-vector one and significantly below the iso-vector E^{++} and T_2^{++} by using mesonic operators. Finally, it is worth noting that the A_1^{-+} masses graphically exhibit larger excited-state contamination than their pure gauge counterparts, most probably due to the denser spectrum. Since the signal-to-noise problem is present in this setup as well, these results emphasize the need to understand the mixing between gluonic and mesonic states as to be able to better disentangle the ground state from the excited ones at early times before the noise becomes dominant.

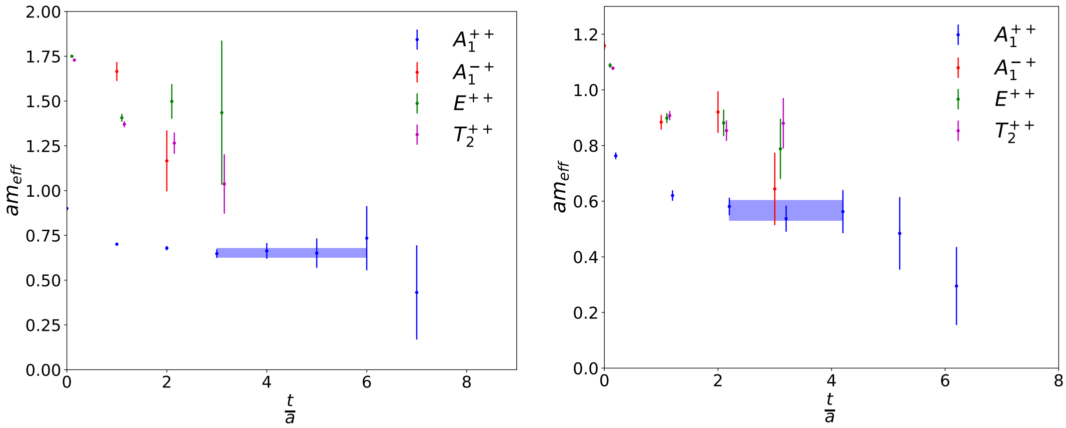

(A) In ensemble Em1.

(B) In ensemble Nm1.

FIGURE 4.10: Ground state effective masses of the irreps A_1^{++}, A_1^{-+}, E^{++} and T_2^{++} in ensembles Em1 and Nm1.

4.3 Mesonic-Gluonic mixing

The mixing between gluonic and mesonic operators will be performed in the A_1^{++} channel using the previously discussed spatial Wilson loops and the iso-scalar $\Gamma = \mathbb{I}$ operator. Furthermore, it is performed only in the Em1 where the statistics for the gluonic operators are sufficiently large. Additionally, since this state is the lightest one on this ensemble then it is expected to yield the clearest signal for the mixing. It is worth noting that the correlation function involving $\Gamma = \mathbb{I}$ at source time and a spatial Wilson loop at sink time is even under time-reversal so the GEVP formulation is well-posed, which is not the case for the mixing involving the $\Gamma = \gamma_5$ operators with a A_1^{-+} gluonic operator. Finally, as can be seen in Fig. 4.11 for ensemble Em1, the effective masses from the optimal A_1^{++} gluonic operator and the iso-scalar $\Gamma = \mathbb{I}$ with the optimal profile are relatively consistent with each other, indicating that both grant relatively good access to this lightest state. This same figure also displays the effective masses coming from the optimal operator built from a 15×15 correlation matrix involving the 7 mesonic operators with the Gaussian profile basis and the 8 different Wilson loop operators used in the previous section. The expected reduction of excited-state contamination can be seen at early times, particularly compared to the pure mesonic results, while at later times it is consistent with the purely gluonic effective masses. Not only this, but the errors are consistent in magnitude with the ones from the gluonic masses which points to the possibility that this kind of operators are the most significant ones to resolve this ground state. The resulting plateau average masses for the three operators are

- Wilson loops: $am = 0.652(25)$
- $\Gamma = \mathbb{I}$ meson with optimal profile: $am = 0.695(40)$
- Optimal linear combination of the latter two: $am = 0.640(21)$,

which are relatively consistent with each other. The effective masses for the first excited state are displayed in Fig. 4.12 for the $\Gamma = \mathbb{I}$ mesonic operator using the optimal profile and the mixed operator generated from the 15×15 mixing correlation matrix. No results are shown from the Wilson loops alone since there is no clear signal there for this state. The fact that both masses are completely consistent with each other and that the Wilson loops alone do not get clear access to this state points to the possibility of it being mainly mesonic, contrary to the ground state which can be accessed by both types of operators and therefore most probably has significant contributions from them. The plateau average masses for this state are given by

- $\Gamma = \mathbb{I}$ meson with optimal profile: $am = 1.114(23)$
- Optimal linear combination of the mesonic and gluonic operators: $am = 1.114(19)$,

which are also considerably close to the $am = 1.07944(48)$ plateau mass for the isoscalar $\Gamma = \mathbb{I}$ operator.

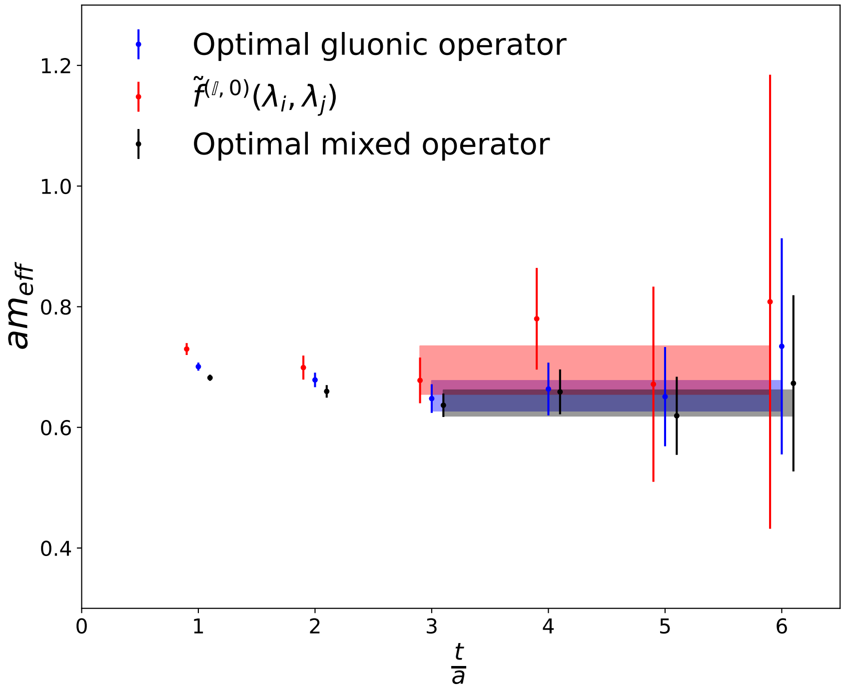

FIGURE 4.11: Ground state effective masses of the A_1^{++} channel using purely gluonic and purely mesonic operators together with the optimal linear combination of them as given by the GEVP formulation in ensemble Em1.

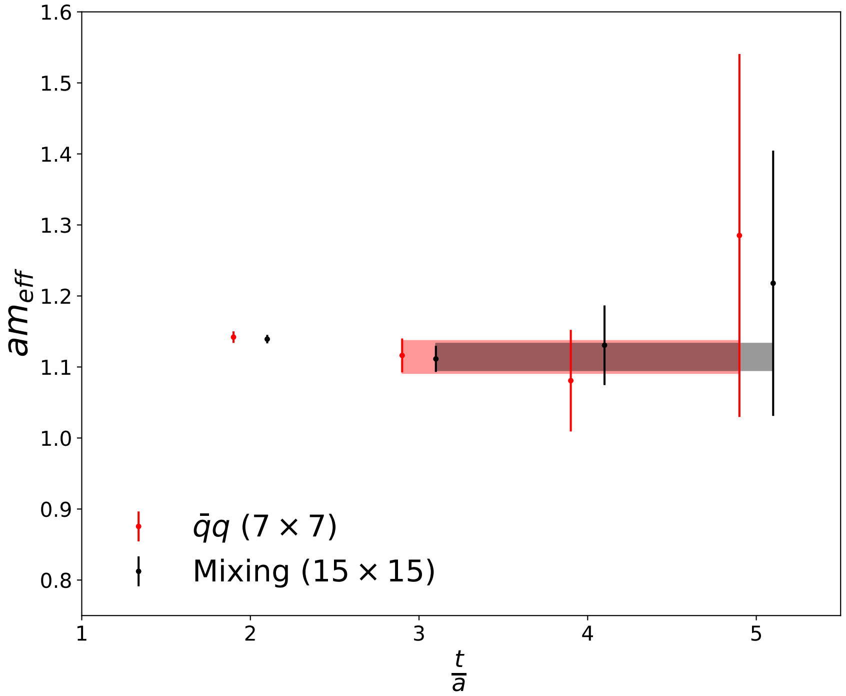

FIGURE 4.12: First excited state effective masses of the A_1^{++} channel using purely mesonic operators together with the optimal linear combination of them with Wilson loops as given by the GEVP formulation in ensemble Em1.

The fact that the effective masses obtained from the GEVP are different to the ones from the separate optimal mesonic and gluonic operators and yield a slightly clearer access to the ground state of interest means that there is a non-negligible mixing between the gluonic and mesonic operators used in this work. This phenomenon is already clear also at the level of the 15×15 correlation matrix where the off-diagonal entries are non-zero at early times when the error does not dominate the signal. The interpretation of this mixing requires some care. The gluonic and mesonic operators used in this work are not expected to create states which are pure glueballs or mesons respectively, but rather these created states have overlaps with presumably all possible energy eigenstates in the symmetry channel independently of the nature of each energy eigenstate. Furthermore, there is no guarantee that the energy eigenstates can be divided into these two kinds and are not a mixture of both. On the contrary, the fact that the Wilson loops, which contain only valence gluons, and the meson operators, which include valence quarks, both grant access to the mass of the ground state points to the possibility that this energy state contains both quark and gluon degrees of freedom. This last observation is the main feature of the results presented in this chapter: one needs to take into account both quark and gluon degrees of freedom to create a state with good overlap with the ground iso-scalar 0^{++} state. On the other hand, the first excited state seems to receive very little or no contributions from gluonic operators, pointing to a mostly mesonic composition. Nonetheless a strong statement about this cannot yet be done, since one should first use other purely gluonic operators or try to improve on the current ones to access this state to determine if the lack of signal is really due to no gluonic contributions to this state or rather an effect of the considerable noise that all gluonic operators suffer from.

Chapter 5

Towards the physical point

> We can only see a short distance ahead, but we can see plenty there that needs to be done.
>
> Alan Turing

This chapter focuses on applying the method of the optimal profiles to the previously described B ensemble corresponding to $N_f = 3 + 1$ QCD at the light flavor symmetric point and one physical charm quark, being significantly closer to the physical point than the previously analyzed Em1 and Nm1 ensembles. A selection of operators corresponding to different symmetry channels are used to study the charmonium spectrum in this ensemble using both standard distillation and the optimal profiles to see how the advantages of the latter manifest themselves in this close-to-physical setup. The resulting spectrum is then compared with one obtained for this same ensemble in [107] and with the corresponding values in nature. The overall agreement with the former at considerably smaller statistics and earlier mass plateau regions further emphasizes the advantages of the method proposed in this work in a close-to-physical setup. The few discrepancies found with respect to nature and their possible causes are discussed.

5.1 Open temporal boundary conditions

As stated in Sect. 2.4, ensemble B has open boundary conditions in the temporal direction. This violates temporal translation invariance and therefore one needs to be careful when calculating temporal correlation functions. One way of doing so is choosing a time interval sufficiently far away from the boundaries such that their effects can be safely neglected in this interval, a strategy which was used in [107] to study flow-related observables in this same ensemble. There the interval was chosen by looking at the behavior of these observables as a function of time which are expected to slightly vary around a constant value when sufficiently away from the open boundaries. The results in this reference serve as a guide to choose the relevant time interval for this work, yet it is useful to perform a similar study based on the Laplacian eigenvalues. As was seen in the Em1 and Nm1 ensembles, these eigenvalues slightly vary around a constant value for the entire temporal extent of the lattice thanks to the periodic boundary conditions in time and the eigenvalues in this ensemble should display a similar behavior away from the open boundaries. Fig 5.1 shows the 5 smallest and largest Laplacian eigenvalues as function of time together with the lower $\left(\frac{t}{a} = 30\right)$ and upper $\left(\frac{t}{a} = 114\right)$ limits of the interval used in [107]. The effects of the open boundary conditions are clear at both sides of the temporal extent, yet in the interval proposed in [107] the expected approximately constant behavior is observed, indicating that it is a suitable choice to measure quantities that depend directly on the Laplacian eigenvalues. It could be argued that this interval could be increased, however the current choice already results in a total of 85 time slices where the correlation functions can be calculated and this quantity was enough to obtain satisfactory results for the spectrum of particles studied in [107]. Since the method presented in this work is expected to significantly improve upon these results then the same choice of time interval should be a good choice.

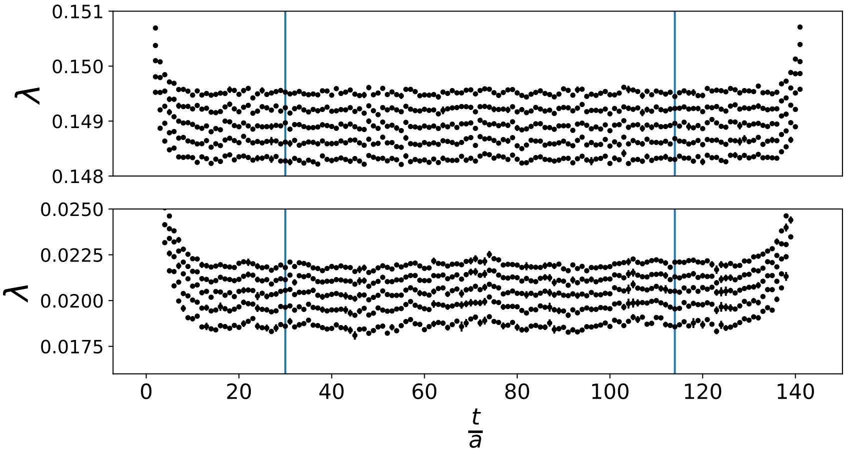

FIGURE 5.1: Five smallest and largest eigenvalues of the 3D covariant Laplacian as a function of time calculated in ensemble B. The vertical lines denote the lower and upper limits of the interval that will be used for calculating the temporal correlation functions in this work.

Two further modifications are required due to the use of temporal boundary conditions and the Lüscher-Weisz gauge action in this ensemble: the calculation of the effective masses and the calculation of the fractional overlaps. As explained in [133, 134], the use of the Lüscher-Weisz gauge action leads to the possibility of a spectral decomposition whose terms are not all necessarily positive. This means at sufficiently large values of time, masses can be extracted from an exponential decay however the resulting effective masses may not necessarily approach the plateau value from above as was the case for the Em1 and Nm1 ensembles. Furthermore, due to the open temporal boundary conditions and the fact that the correlation is measured at values of time sufficiently far away from the boundaries, the effective masses must be calculated as

$$am_{eff}(t) = \ln\left(\frac{C(t)}{C(t+a)}\right), \tag{5.1}$$

unlike the root-finding method related to the cosh behavior of the temporal correlation functions used for the Em1 and Nm1 ensembles. The correlation function $C(t)$ in question can no longer be calculated as an average over all sources exploiting translation invariance over the whole temporal extent, i.e

$$C(t) = \frac{1}{N_t}\sum_{s=0}^{N_t-1} C(as+t, as), \tag{5.2}$$

since the correlation function $C(t_1, t_2)$ between all possible source and sink times is not available and boundary effects can become significant even if all source and sink times were available. Instead translation invariance is only assumed in the interval chosen far away from the boundaries and the number of terms in the average will depend on the value of t. Finally, the fractional overlaps have to be redefined in terms of exponentials and not hyperbolic cosines as follows. The temporal correlation function in the chosen interval is expected to have the form

$$C(t) = c_0 e^{-m_0 t} + B_1(t), \tag{5.3}$$

where c_0 is a time-independent constant and $B_1(t)$, now allowed to be negative, accounts for the contributions from excited states. The normalized correlation function can be defined as

$$\frac{C(t)}{C(t_G)} = \left(\frac{1 + B_2(t)}{1 + B_2(t_G)} \right) e^{-m_0(t-t_G)}, \tag{5.4}$$

with

$$B_2(t) = \frac{B_1(t)}{c_0} e^{m_0 t}. \tag{5.5}$$

The effective fractional overlap can be defined as

$$A_{eff}(t) = \frac{C(t)}{C(t_G)} e^{m_0(t-t_G)}, \tag{5.6}$$

and in the mass plateau interval where $B_1(t)$ is well-approximated by 0 this effective fractional overlap should provide a good approximation to the constant

$$A = \frac{1}{1 + B_2(t_G)}. \tag{5.7}$$

In total absence of any excited-state contamination at time t_G the fractional overlap becomes 1, which was also the case for the Em1 and Nm1 ensembles. In the presence of excited-state contamination this quantity can either be smaller or larger than 1 depending on the sign of $B_2(t_G)$, unlike the case of Em1 and Nm1 where $B_2(t)$ was strictly positive. There is a possible divergence in the limit when $B_2(t_G)$ approaches -1, nonetheless this is not a problem since what matters for the fractional overlap is its closeness to 1 as a measure of the excited-state contamination and therefore a divergence towards $\pm\infty$ simply means that $|B_2(t_G)| = 1 > 0$. It should be noted that this is not expected to happen in the numerical calculations. Furthermore, it was observed in the Em1 and Nm1 ensembles that both standard distillation and the one with the optimal profiles yielded fractional overlaps significantly closer to 1 than 0.5 and therefore one would not expect to obtain values of $B_2(t_G)$ close enough to -1 to yield problematically large values of fractional overlap. As mentioned in the derivation of the fractional overlap for the case with periodic boundary conditions, statistical fluctuations and numerical instability at large values of time in the case of the GEVP leads to deviations from the expected constant of Eqn. (5.7), which in turn introduces a systematic error to the effective fractional overlaps which can also contribute to the approach to 1 from above.

5.2 Charmonium in ensemble B

5.2.1 Setup of distillation parameters

The first consideration is the choice of N_v based on the results obtained for the Em1 and Nm1 ensembles. The 3D volume scaling from the Em1 ensemble as was done for the Nm1 ensemble yields

$$N_v = 200 \times \left(\frac{0.0429 \times 48}{0.0658 \times 24} \right)^3 \approx 444, \tag{5.8}$$

which means that, unlike in Nm1 where one would have needed to triple the number of eigenvectors used, one needs to roughly double the number of eigenvectors to achieve a similar level of smearing in this ensemble. Although this would represent less computational work than for the Nm1 ensemble, it is still outside of reach with the resources available for this work. Nonetheless, this is not expected to be a problem: the use of the optimal profiles in ensemble Nm1 showed that with 325, out of the 600 that the 3D volume scaling suggested, the improvement obtained over standard distillation was already considerably significant and very clear access to ground states together with a preliminary access to first excited states was achieved. Although ensemble B has fundamental differences to Em1 and Nm1, it would be expected (and will be shown) that using 325 vectors out of a recommended 444 together with the use of the optimal profiles yields similar if not better improvements over standard distillation. With this in mind, the value $N_v = 325$ that was used for Nm1 is kept for ensemble B as well. Another important consideration is that with only a single charm quark in this ensemble, there is no iso-spin symmetry and the corresponding correlation functions for charmonia should include both connected and disconnected pieces. Nonetheless, these disconnected contributions are still expected to be relatively small compared to the connected ones and will be neglected, which constitutes a systematic error in the final spectrum. As a further note, the correlation functions which are measured as primary observables are reweighed as described in [107]. The quark profiles used are the same Gaussian functions as for ensembles Em1 and Nm1 but the widths have been scaled with the ratio of squared lattice spacings with respect to the Em1 widths.

5.2.2 Results from local and derivative-based operators

5.2.2.1 Charmonium spectrum

The same analysis strategy as for ensembles Em1 and Nm1 is used regarding the pruning of the correlation matrix and solution of the GEVP. The ground state effective masses for the case of $\Gamma = \gamma_5$ using both standard distillation and the optimal profile are displayed in 5.2. As expected, the use of the optimal profile leads to a very significant suppression of excited-state contamination, which allows a much earlier and longer mass plateau for this channel. This improvement at early times is of particular importance since the effective masses at large values of t come from correlation functions which are averaged over fewer time sources and therefore are expected to have larger errors. This is clear from looking at the fluctuations and errors of the masses at times $\frac{t}{a} \geq 60$. The mass plateau averages are $am = 0.64574(14)$ for standard distillation and $am = 0.64574(15)$ for the optimal profile, showing a complete agreement between both methods.

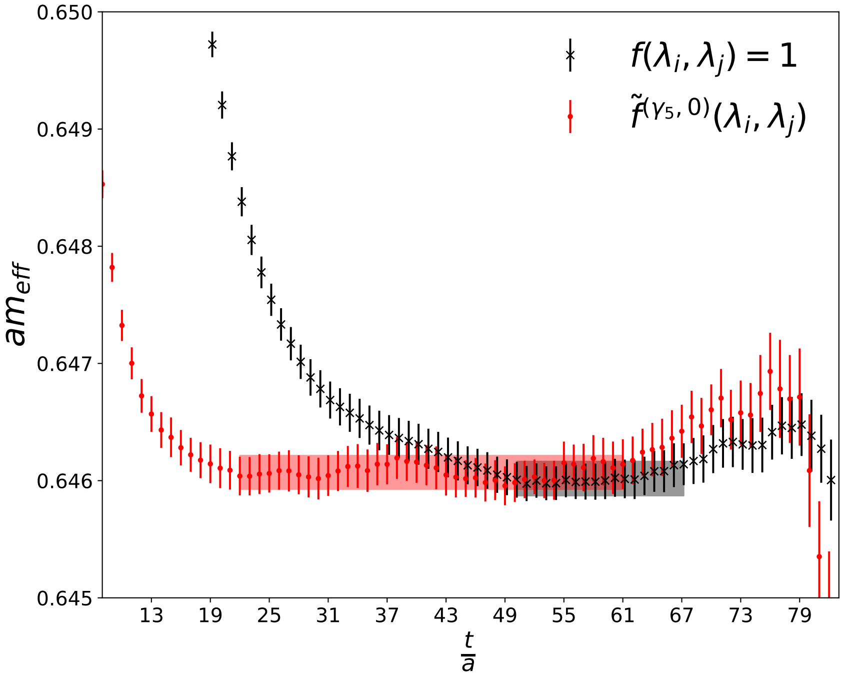

FIGURE 5.2: Ground state effective masses of the $\Gamma = \gamma_5$ operator using standard distillation ($f(\lambda_i, \lambda_j) = 1$) and distillation with the optimal meson distillation profile for the ground state $\left(\tilde{f}^{(\gamma_5,0)}(\lambda_i, \lambda_j)\right)$ in ensemble B.

The plateau averages of the fractional overlaps are given by 0.9380(22) for standard distillation and 0.99909(66) for the optimal profile which further confirms the improvement. These results highlight the method of optimal profiles proposed in this work yields significant improvements not only in the simplified models where it was first tested but also in an ensemble with a close-to-physical setup. The obtained mass for this operator is in good agreement with the one reported in [107], achieving a consistent precision while using considerably smaller statistics. A final result for this operator is the mass for its first excitation. The corresponding effective masses are displayed in Fig. 5.3, where a somewhat clear plateau region can be identified. The signal for the mass of this first excited state is considerably better than the one obtained in the Em1 and Nm1 ensembles in terms of length of the plateau and suppression of early time contamination, as the plateau starts immediately after the value of t_G (cf. Eqn. (2.40)). The latter is not surprising, since the value of $\frac{t_G}{a}$ is considerably larger than in the other two ensembles and therefore the contamination from other states at this time is expected to be more suppressed than it was at $\frac{t_G}{a} \approx 4$ for the other ensembles.

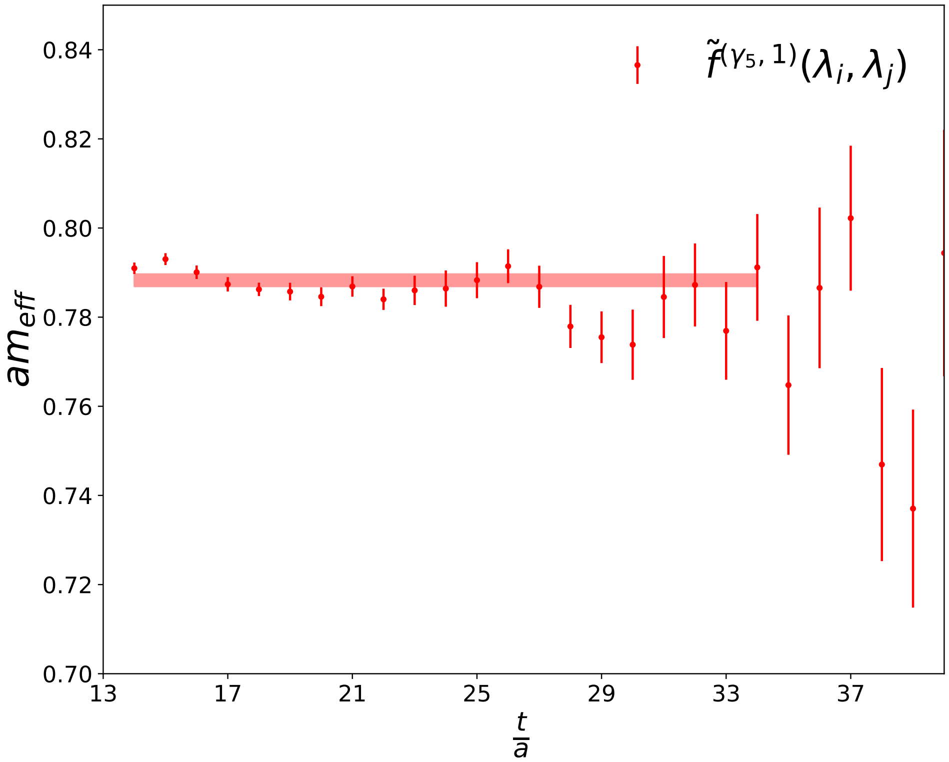

FIGURE 5.3: Effective masses of the first radial excitation of the $\Gamma = \gamma_5$ operator accessed via the corresponding optimal meson distillation profile in ensemble B.

The ground state effective masses using both standard distillation and the corresponding optimal profiles can be seen in Fig. 5.4. All the local operators exhibit a significant suppression of excited-state contamination when using the optimal profile. Additionally, all cases display mass plateau values which are compatible between both approaches. As expected, large errors become particularly problematic at large values of time partly due to the restricted averaging over available time sources, however the plateau regions start early enough to be safe from this issue. The effective masses for the first excitation of each operator using the corresponding optimal profile are displayed in Fig. 5.5. Just as for the $\Gamma = \gamma_5$ operator, there is a relatively early and clear access to the masses of these different operators. This is an encouraging result, since it shows the sole use of the optimal profiles grants sufficient access to the first excitation and any improvement achieved by including other Γ operators in an extended GEVP will build on it. The corresponding mass plateau averages and fractional overlaps for ground and first excited states of all local operators are displayed in Table 5.1, where the improvement brought by the optimal profiles can be quantitatively seen. All operators display plateau masses consistent between both methods used, the fractional overlaps are shifted considerably closer to 1 when the optimal profiles are used and the plateau intervals both start earlier and are longer compared to standard distillation, leading to more precise masses.

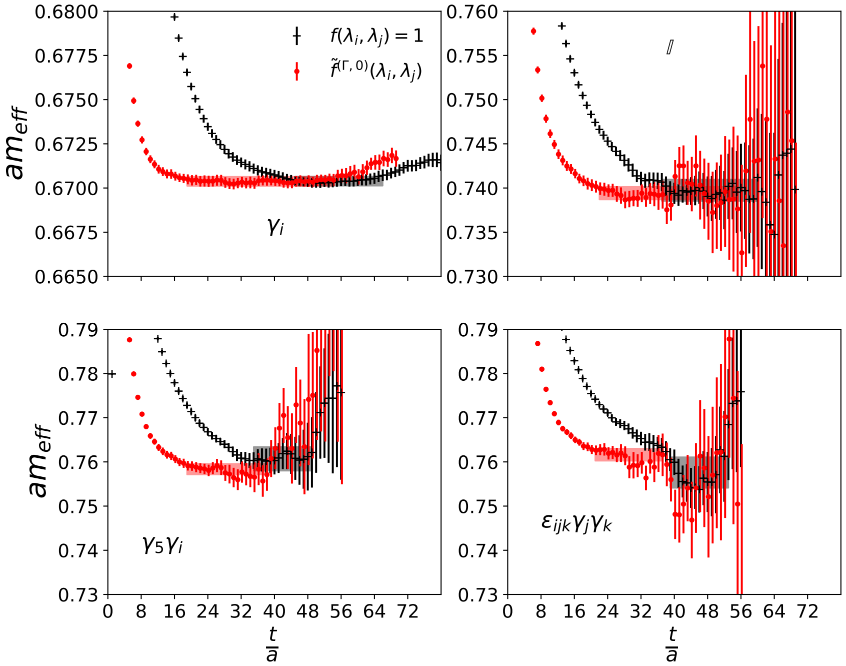

FIGURE 5.4: Ground state effective masses of the operators built from local Γ given in the plots in ensemble B.

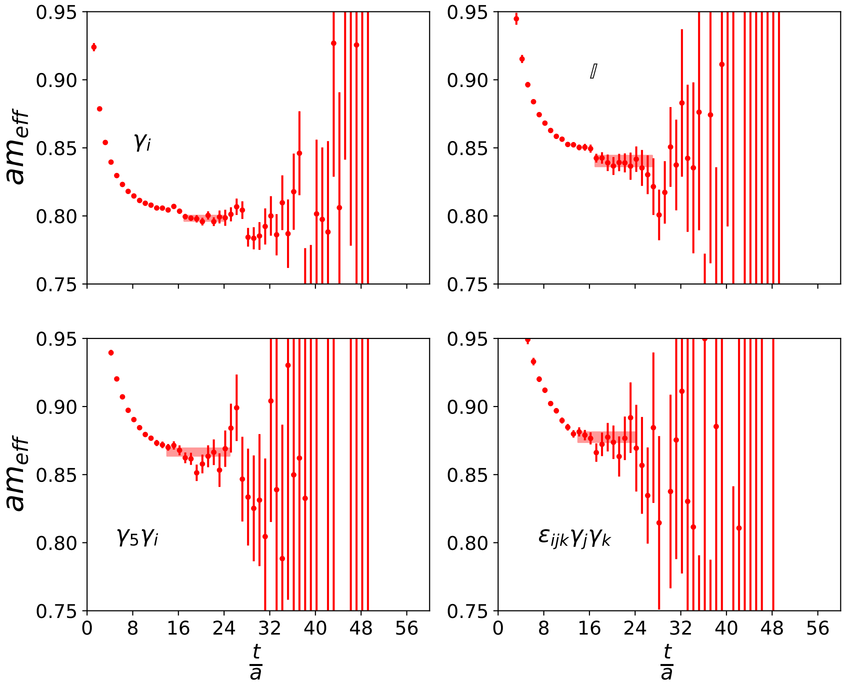

FIGURE 5.5: First excited state effective masses of the operators built from local Γ given in the plots in ensemble B.

Γ	Plateau masses	Fractional overlaps	Plateau intervals
γ_5	0.64602(15)	0.9375(20)	50-67
	0.64607(14)	0.99828(73)	22-61
	0.7883(14)	0.9955(16)	14-34
γ_i	0.67041(26)	0.8983(45)	45-66
	0.67039(26)	0.9984(10)	19-54
	0.7983(21)	0.9733(62)	17-24
$\mathbb{I}$	0.7400(12)	0.856(20)	37-60
	0.73950(71)	0.9842(42)	22-55
	0.8394(37)	0.9607(89)	17-27
$\gamma_5\gamma_i$	0.7607(27)	0.830(40)	35-49
	0.7583(12)	0.9858(44)	19-38
	0.8662(29)	0.9946(25)	14-25
$\epsilon_{ijk}\gamma_j\gamma_k$	0.7577(35)	0.693(55)	39-53
	0.7617(14)	0.9771(71)	21-37
	0.8777(38)	0.9991(39)	14-24

TABLE 5.1: Plateau average masses and fractional overlaps for the ground and first excited states using local Γ operators in ensemble B. For a fixed Γ the first row corresponds to the ground state using standard distillation, the second row to the ground state using the optimal profile and the third row to the first excited state using the optimal profile.

With the presence of light quarks there is a threshold energy at which the different states can decay into multi-particle states involving D mesons, which was not the case in the Em1 and Nm1 ensembles. The mass of the D and D_s mesons, which are degenerate in this ensemble, was calculated in [107] to be $am_{D,D_s} = 0.4138(4)$. Twice this value sets the $D\bar{D}$ threshold at $0.8276(7)$ and an excited state with quantum numbers 0^{++} can decay into a $D\bar{D}$ pair, for example. This can be the case for the first excited state of the $\Gamma = \mathbb{I}$ operator, whose mass is above the $D\bar{D}$ threshold. This state is not stable and its analysis would require the use of multi-meson operators, which is beyond the scope of this work. Further excited states with other J^{PC} can similarly decay into multi-meson states with matching quantum numbers so in this work only the states whose masses are below the $D\bar{D}$ threshold will be considered as stable. For completeness, their masses obtained from local operators in lattice $(am_{\bar{c}c})$ and physical units $(m_{\bar{c}c})$ are displayed in Table 5.2. Their similarity to the corresponding values in nature $(m^*_{\bar{c}c})$ [4] is clear. The uncertainties for the masses converted into physical units include the one from the lattice spacing as reported in [107].

J^{PC}	$am_{\bar{c}c}$	$\sqrt{t_0}m_{\bar{c}c}$	$m_{\bar{c}c}$	$m^*_{\bar{c}c}$
0^{-+}	0.64607(14)	2.1979(33)	2.970(36)	2.9839(4)
1^{--}	0.67039(26)	2.2806(33)	3.082(38)	3.096900(6)
0^{++}	0.73950(71)	2.5154(29)	3.399(41)	3.41471(30)
1^{++}	0.7583(12)	2.5799(32)	3.486(42)	3.51067(5)
1^{+-}	0.7617(14)	2.5911(33)	3.502(43)	3.52538(11)

TABLE 5.2: Plateau average masses of the ground state using local Γ operators in ensemble B in both lattice and physical units together with the mass of the state in nature $m^*_{\bar{c}c}$. Physical masses are given in GeV.

In this ensemble the only derivative-based Γ operators studied transform in the E^{++} and T_2^{++} irreps to get access to the 2^{++} channel, i.e $\Gamma = \mathbb{Q}_{ijk}\gamma_j\nabla_k\ (E^{++})$, $|\epsilon_{ijk}|\gamma_j\nabla_k\ \left(T_2^{++}\right)$. Fig. 5.6 displays the ground state effective masses for both of these operators using standard distillation and the corresponding optimal profiles. With both methods the effective masses are almost identical to each other until the errors become relatively large at $\frac{t}{a} > 30$ for the GEVP results, after which they are still consistent. Due to this the resulting four plateau averages are consistent with each other. This reflects how at such a small value of lattice spacing a the ground states of both E^{++} and T_2^{++} come close together to become the ground state of the 2^{++} channel. The suppression of excited-state contamination at early times is also visible and leads to considerably early and longer plateau regions compared to the case of standard distillation. Fig. 5.7 displays the effective masses corresponding to the first excited state of both operators using the corresponding optimal profiles, where there is again an agreement between the results of both operators, indicating that this state belongs to channel where both irreps contribute. The mass plateau averages and corresponding fractional overlaps are displayed in Table 5.3 which quantify the improvement achieved thanks to the use of the optimal profiles. It is worth noting that with the optimal profiles the error is halved with respect to standard distillation. Table 5.4 displays the ground state mass plateau averages $am_{\bar{c}c}$ converted to physical units together with the value of the ground state 2^{++} in nature $m^*_{\bar{c}c}$. The masses of the first excited state of both operators is above the $D\bar{D}$ threshold and therefore this state is not stable.

A final calculation related to the obtained masses and which exemplifies the high precision achieved is setting the scale based on them. This can be done by calculating the splitting between spin-singlet states

$$a\Delta = am_{h_c} - am_{\eta_c} \tag{5.9}$$

and demanding its physical value is as in nature, i.e

$$\Delta = m^*_{h_c} - m^*_{\eta_c}. \tag{5.10}$$

Solving for a results in

$$a = 0.04212(49)\ \text{fm}, \tag{5.11}$$

which is in good agreement with the 0.04292(52) fm obtained in [107] using 2000 configurations of this ensemble opposed to the 500 used in this work. The similarity of the uncertainty in the presence of such difference in statistics is yet another advantage of using the optimal profiles.

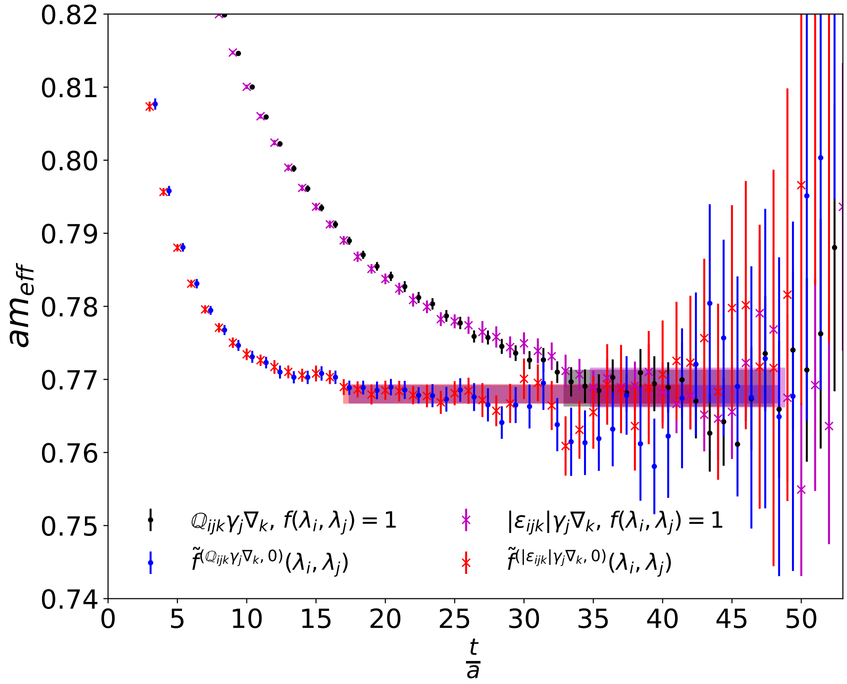

FIGURE 5.6: Ground state effective masses of the $\Gamma = \mathbb{Q}_{ijk}\gamma_j\nabla_k$ and $\Gamma = |\epsilon_{ijk}|\gamma_j\nabla_k$ in ensemble B.

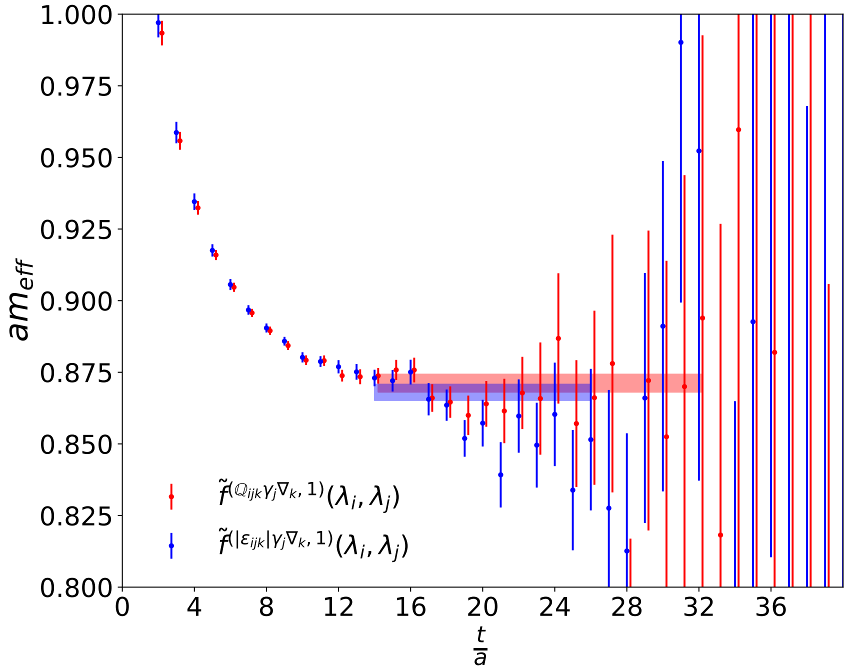

FIGURE 5.7: First excited state effective masses of the $\Gamma = \mathbb{Q}_{ijk}\gamma_j\nabla_k$ and $\Gamma = |\epsilon_{ijk}|\gamma_j\nabla_k$ operators in ensemble B.

Γ	Plateau masses	Fractional overlaps	Plateau intervals
$\mathbb{Q}_{ijk}\gamma_j\nabla_k$	0.7688(25)	0.767(31)	33-48
	0.7680(12)	0.9907(31)	17-48
	0.8710(31)	0.9972(28)	14-32
$\lvert\epsilon_{ijk}\rvert\gamma_j\nabla_k$	0.7691(26)	0.762(39)	35-49
	0.7680(13)	0.9900(35)	17-42
	0.8678(28)	0.9909(30)	14-26

TABLE 5.3: Plateau average masses and fractional overlaps for the ground and first excited states using the $\Gamma = \mathbb{Q}_{ijk}\gamma_j\nabla_k, \lvert\epsilon_{ijk}\rvert\gamma_j\nabla_k$ operators in ensemble B. For a fixed Γ the first row corresponds to the ground state using standard distillation, the second row to the ground state using the optimal profile and the third row to the first excited state using the optimal profile.

J^{PC}	$am_{\bar{c}c}$	$\sqrt{t_0}m_{\bar{c}c}$	$m_{\bar{c}c}$	$m^*_{\bar{c}c}$
2^{++} (E^{++})	0.7680(12)	2.6126(32)	3.531(43)	3.55617(7)
2^{++} (T_2^{++})	0.7680(13)	2.6126(32)	3.531(43)	3.55617(7)

TABLE 5.4: Plateau average masses of the ground state using E^{++} and T_2^{++} Γ operators in ensemble B in both lattice and physical units together with the mass of the state in nature $m^*_{\bar{c}c}$. Physical masses are given in GeV.

5.2.2.2 Optimal meson distillation profiles

The optimal profiles obtained for the ground state of the local Γ operators are displayed in Fig. 5.8. All profiles show the expected suppression of larger eigenvalues and enhancement of the lowest ones together with a similarity in overall shape among S- and P-waves. It is worth noting that the error bars of these profiles are larger, than the ones obtained for the Em1 and Nm1 ensembles. This is a consequence of the smaller statistics available for this ensemble and the restricted average over time sources for the correlation functions in the time interval chosen away from the open temporal boundaries.

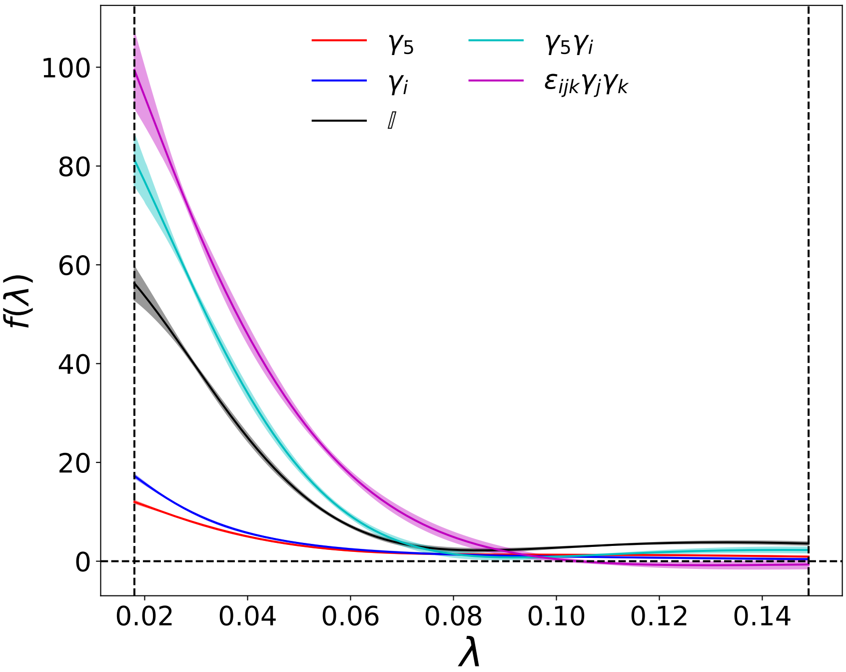

FIGURE 5.8: Optimal meson distillation profiles for the ground state of the local Γ operators in ensemble B.

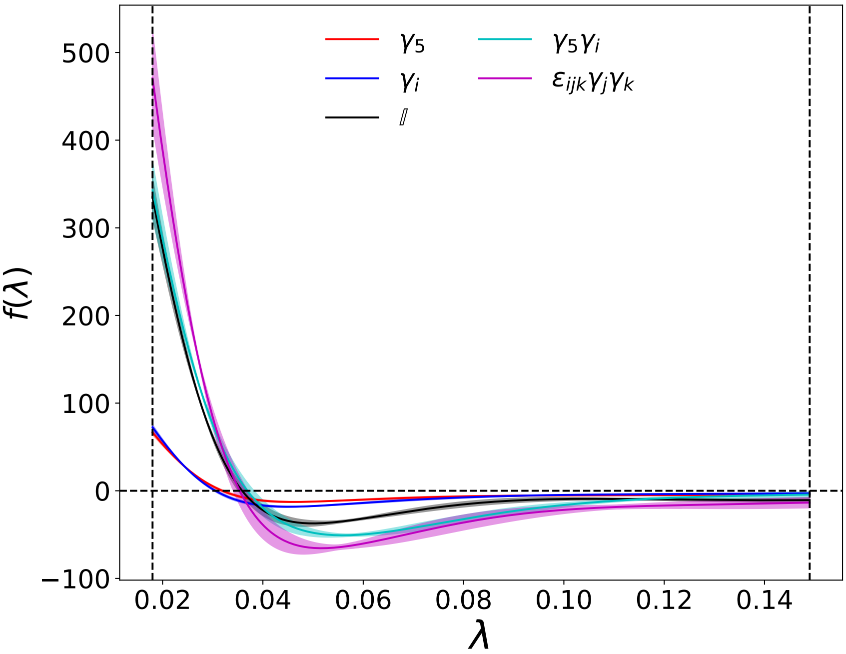

FIGURE 5.9: Optimal meson distillation profiles for the first excited state of the local Γ operators in ensemble B.

The optimal profiles obtained for the first excited state of the local Γ operators are displayed in Fig. 5.9. The expected single node appears in all cases at rather small values of the eigenvalues which indicates non-trivial structure in space. The suppression of larger eigenvalues is still present as for the Em1 and Nm1 ensembles, yet the higher eigenvalues are more significantly suppressed. A similar feature is observed for the ground state profiles and might be related to the difference in the charm quark mass which in turn can affect the spatial distribution of the meson state. The optimal meson distillation profiles for the different states of the $\Gamma = \mathbb{Q}_{ijk}\gamma_j\nabla_k$ and $\Gamma = |\epsilon_{ijk}|\gamma_j\nabla_k$ operators can be built as for the Em1 and Nm1 ensembles. Fig. 5.10 shows the profile of the ground state of each operator. Both profiles have very similar overall behavior; the radial symmetry and suppression of larger eigenvalues are still present in both cases. Fig. 5.11 depicts the profiles of both operators corresponding to the first excited state, where again the suppression of larger eigenvalues is observed together with a radially symmetric node indicating a non-trivial spatial structure. The presence of the node around relatively small values of $r = \sqrt{\lambda_i^2 + \lambda_j^2}$ and the suppression by a factor of roughly $\frac{1}{10}$ at the largest values of r indicate that the choice of $N_v = 325$ is suitable to study both states.

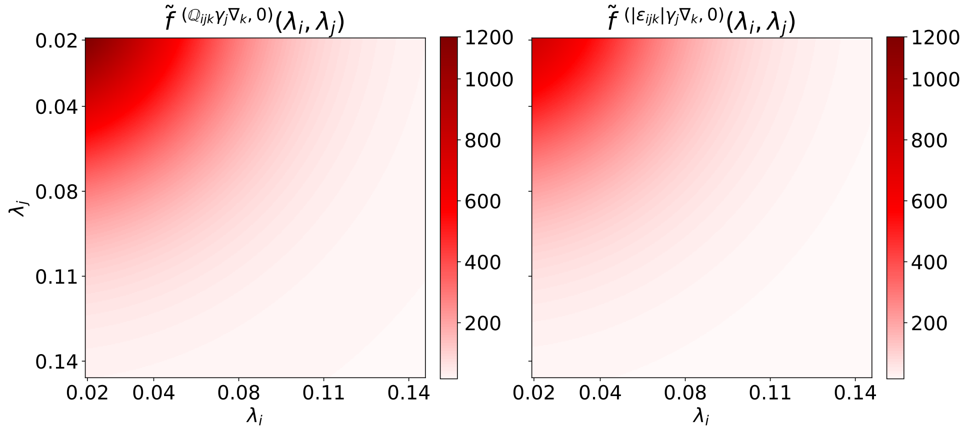

FIGURE 5.10: Optimal meson distillation profiles for the ground state of the $\Gamma = \mathbb{Q}_{ijk}\gamma_j\nabla_k, |\epsilon_{ijk}|\gamma_j\nabla_k$ operators in ensemble B.

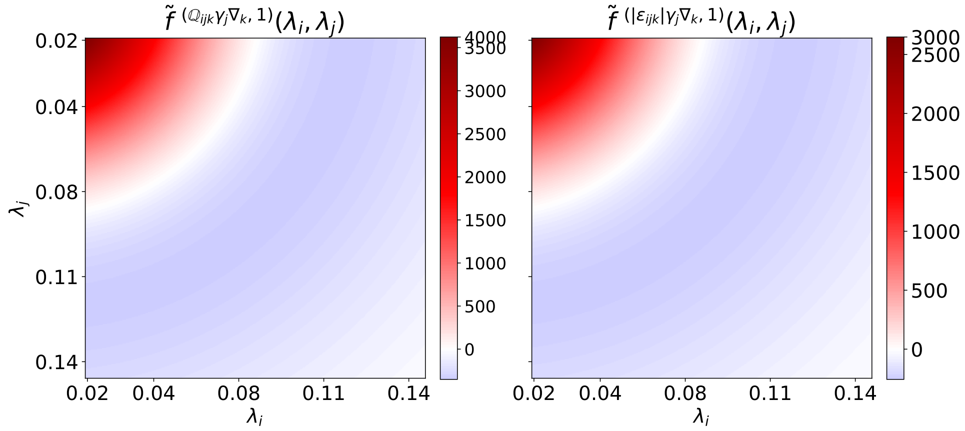

FIGURE 5.11: Optimal meson distillation profiles for the first excited state of the $\Gamma = \mathbb{Q}_{ijk}\gamma_j\nabla_k, |\epsilon_{ijk}|\gamma_j\nabla_k$ operators in ensemble B.

5.2.2.3 Spatial profiles via the optimal meson distillation profiles

As with Em1 and Nm1, the spatial profile of the ground and first excited states of the $\Gamma = \gamma_5$ operator can be built using the corresponding optimal distillation profiles, this time by placing the 3D point-source at $\vec{z} = (24a, 24a, 24a)$ and evaluating it on a single configuration. Both spatial profiles are displayed in Fig. 5.12, which are very similar to the ones from the other two ensembles analyzed in this work. The radial symmetry and the appearance of a node can be seen and both profiles appear to be well contained within the spatial extent of the lattice, which indicates that finite-volume effects are still negligible for these two states.

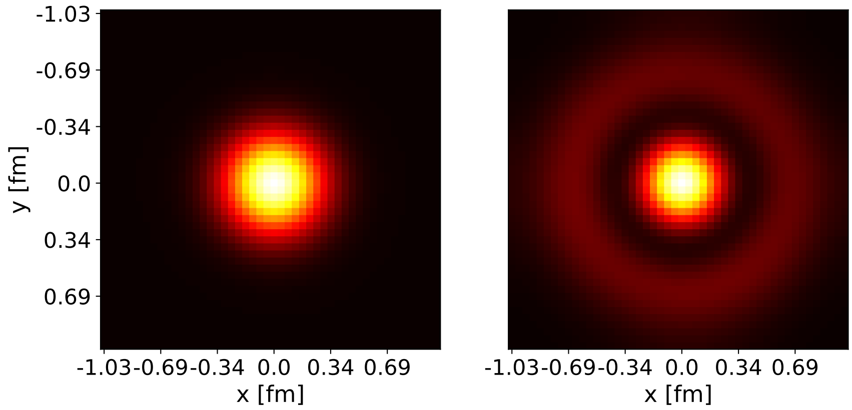

FIGURE 5.12: Spatial profiles for the ground and first excited states of the $\Gamma = \gamma_5$ operator in ensemble B.

5.2.3 Comparison with other lattice calculations

The ground state masses for the $\Gamma = \gamma_5, \gamma_i$ operators are consistent with those in [107] while the remaining three exhibit a slight tension. This can be explained by looking at Fig. 5.13, which shows the effective masses using the optimal profiles together with the ones from [107], which were calculated without using distillation. The plateau regions of the $\Gamma = \mathbb{I}, \gamma_5\gamma_i$ and $\epsilon_{ijk}\gamma_j\gamma_k$ of the latter work are heavily affected by excited-state contamination, shifting each of the estimated plateau averages above the ones from this work. Additionally, no quark smearing was used there, which means excited-state contamination is more pronounced at early times. Furthermore, the correlation functions were built by fixing the source time close to a boundary and varying the sink time to reach different temporal separations. The dominant terms in the spectral decomposition of such correlation functions are different to those of the correlation functions calculated here since they contain a dependence on the source time [135, 136]. This means a direct comparison to quantify the suppression of excited-state contamination cannot be straightforwardly done by looking at the values of the correlation function at early times, however it helps to explain the tension between the mass plateau values. What can be asserted is that the use of optimal profiles in a region away from the boundaries results in effective masses approaching their corresponding plateau quicker and with a comparable level of statistical precision despite having considerably smaller statistics. Furthermore, the effective masses from the optimal profiles for the P-waves show the plateaus calculated in [107] were still heavily affected by contamination of excited states, which introduces a systematic error in the plateau averages reported.

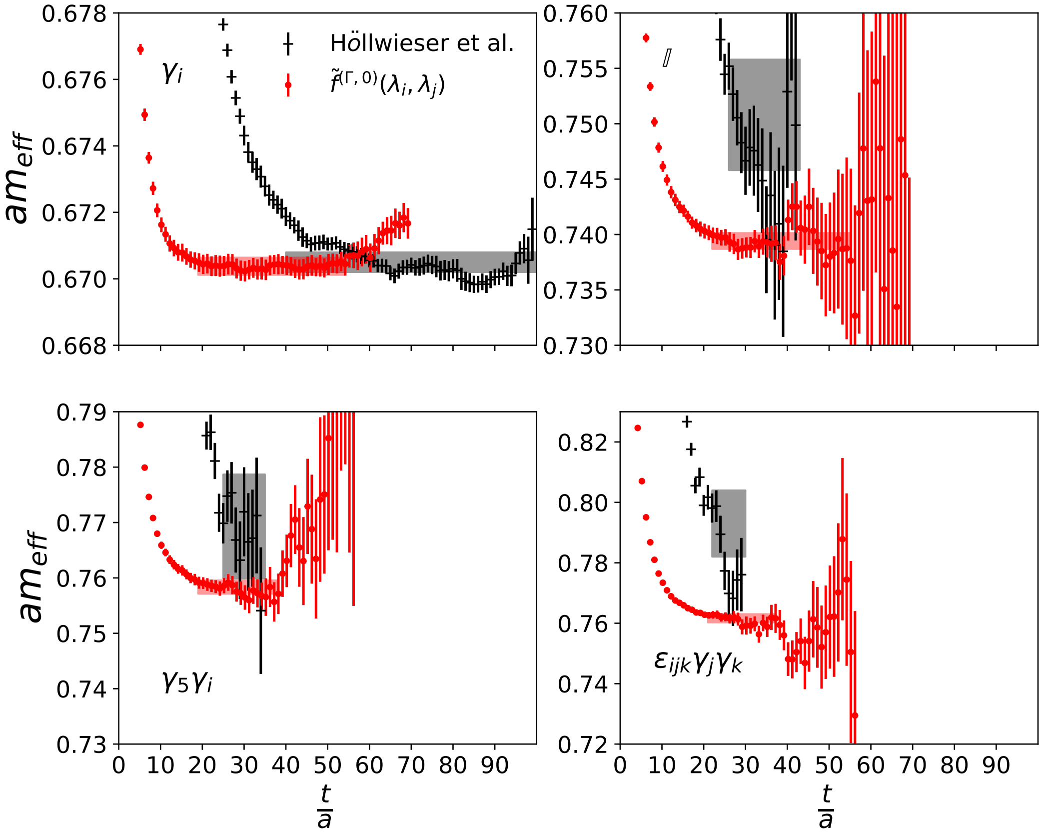

FIGURE 5.13: Ground state effective masses of the operators built from local Γ not including the $\Gamma = \gamma_5$ case in ensemble B using the corresponding optimal profile together with the effective masses measured in [107].

The different mass splittings can be compared to those from different state-of-the-art lattice calculations. Table 5.5 displays the hyperfine splitting Δm_{HF} obtained in this work together with its value from other calculations as well as in nature. In [17] the authors use $2+1+1$ and $1+1+1+1$ HISQ ensembles and tune the charm quark mass to recover the physical J/ψ mass. A continuum extrapolation is done to obtain the final splitting result and the one included in the table does not include the effects of QED, which the authors also study. This study does not use distillation but rather wall sources. In [126] the authors use a $2+1$ asqtad fermion action for the up, down and strange quarks and include the charm quark by tuning its bare mass so the kinetic mass of the D_s matches the one in nature. The set of operators for each irrep used in this reference includes the local and derivative-based ones used in this work, however the authors do not use distillation but rather Gaussian smearing of sources. The authors also perform a continuum extrapolation using a number of different ensembles with different lattice spacings. In [118] the authors use a $2+1$ anisotropic clover action for the up, down and strange quarks and include the charm quark by tuning its bare mass so the ratio of the η_c meson mass and Ω baryon mass has its physical value. Unlike the previous two references, this study uses distillation. Their value of Δm_{HF} deviates significantly from the one in nature, however this was shown in [110] to be due to discretization effects related to the large value of the spatial lattice spacing $a_s \approx 0.12$ fm. Nonetheless, the statistical uncertainty of the result is compatible with the ones from the other calculations. The splitting presented in this work is in good agreement not only with the value in nature but also with all other lattice calculations except for [118], even when no continuum extrapolation was done. Furthermore, the statistical errors in this work are completely compatible with all other lattice calculations, some of which have considerably larger statistics. Table 5.6 displays the remaining splittings for the 8 stable states, i.e splittings involving ground state masses and the hyperfine splitting for the first excited state of the 0^{-+} and 1^{--} channels denoted as Δm_{HF-1}. All splittings show good agreement with their corresponding experimental value as well as with the results from [126]. In particular, all splittings from this work except for Δm_{1P-1S} have smaller statistical errors despite coming from smaller statistics. The absence of the disconnected contributions to the correlation functions, the difference in the light quark masses and the omission of QED effects lead to additional sources of systematic error which can account for discrepancies between the values in this ensemble and their counterparts in nature.

This work	Ref. [17]	Ref. [126]	Ref. [118]	Nature [4]
111.8(1.4)	118.6(1.1)	116.2(1.1)	88(1)	113.0(5)

TABLE 5.5: Hyperfine splitting Δm_{HF} calculated in this work together with its value in other state-of-the-art lattice calculations as well as in nature. All values are given in MeV.

Splitting	This work	Nature [4]	Ref. [126] *et al.*
Δm_{1P-1S}	447.3(5.5)	456.64(14)	462.2(4.5)
Δm_{SO}	43.93(87)	46.60(8)	46.6(3.0)
Δm_{tensor}	14.43(41)	16.27(7)	17.0(2.3)
Δm_{1PHF}	-0.2(1.6)	-0.09(14)	-6.1(4.2)
Δm_{HF-1}	45.9(1.8)	48(1)	

TABLE 5.6: Mass splittings for the stable states in ensemble B. All values are given in MeV.

The final spectrum obtained can be seen in Fig. 5.14, where the mass of the ground state η_c (0^{-+}) has been subtracted from all others. This subtraction is done to eliminate the effects of the charm quark mass mistuning, a strategy which was also used in [118]. The solid rectangles are the masses converted to physical units via the lattice spacing determined in [107] using the physical value of t_0 at the $N_f = 3$ symmetric point [137], the red bands correspond to the $D\bar{D}$ threshold as measured in [107] and the blue rectangles correspond to the values in nature [4], including the $\bar{D}_0 D_0$ threshold. The good agreement with nature in most cases that was observed in Table 5.2 is graphically seen. The J^{PC} are used as labels instead of the irreps R^{PC} based on the agreement with the values in nature, including the combination of the E^{++} and T_2^{++} ground states into a single 2^{++} state since the plateau average masses are identical within errors. The disconnected contributions were ignored yet there is an overall agreement with nature up to small differences in some of the P-waves. This indicates that these effects might play a larger role in these states. A future study of these disconnected contributions for each symmetry channel will help clarify this issue. Nonetheless, even if these disconnected contributions have very small effects in the masses, they cannot be fully neglected since the mixing with glueballs and in between light and heavy flavor neutral states can only happen through them.

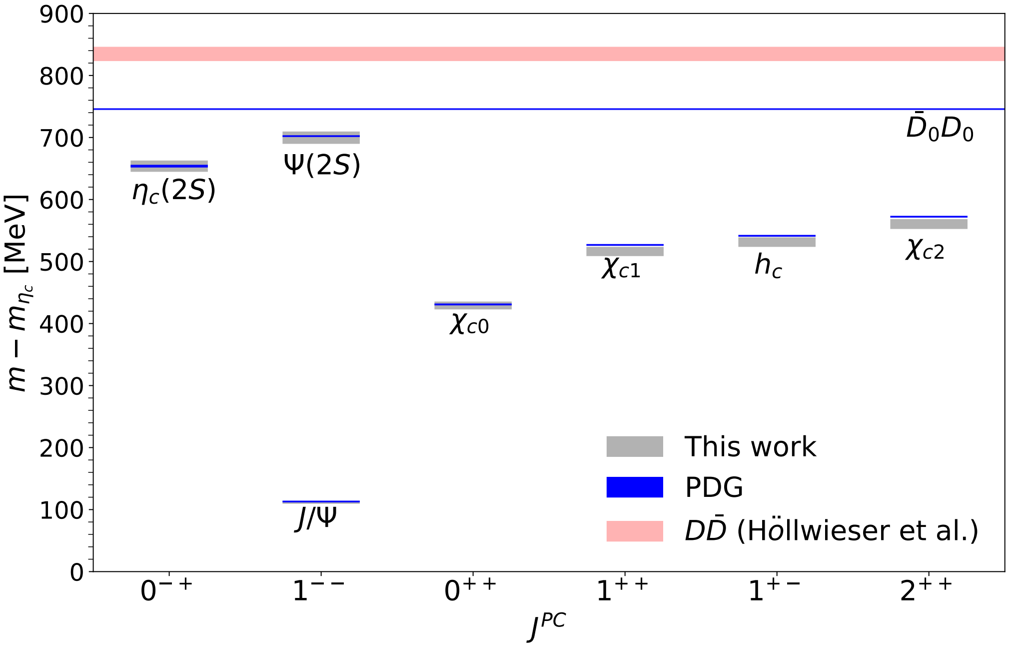

FIGURE 5.14: Low-lying charmonium spectrum relative to the $\eta_c(1S)$ in ensemble B converted to physical units including the $D\bar{D}$ threshold as measured in [107].

5.2.4 A first look at the disconnected contributions

To get a clear picture of the current problem when measuring disconnected contributions to the correlation functions at such a close-to-physical setup one can see what their signal is for the $\Gamma = \gamma_5$ operator. Fig. 5.15 shows this contribution with standard distillation. There is a non-negligible signal up until around $\frac{t}{a} = 15$, meaning one can add the disconnected contribution to the connected one to form the full correlation function. However, this would prove problematic since this disconnected contribution has a change of sign. A possible interpretation for this sign change is the following. In the Em1 and Nm1 ensembles, the disconnected contribution for this same operator was negative. When summed with the positive connected contribution, the effective masses of the iso-scalar state were larger than the ones from the iso-vector. For the case of $\Gamma = \mathbb{I}$, the disconnected contributions were positive and the effective masses of the iso-scalar were smaller than the ones from the iso-vector. If the sign of the disconnected contribution has this same effect in this ensemble then the negative values at early times indicate contributions from heavier states. The change to a positive sign that happens at later times would therefore indicate that the contributions from lighter states become dominant. These states correspond to iso-scalar pseudo-scalars made of light quarks. This sign change was not present in the Em1 and Nm1 ensembles and even there it was complicated to extract the effective mass including the disconnected contribution for $\Gamma = \gamma_5$, which indicates a similar calculation in this setup is considerably more difficult. The disconnected contribution for $\Gamma = \mathbb{I}$ is shown in Fig. 5.16, where there is also a non-negligible signal at early times. There is no sign change, as was the case in Em1 and Nm1 when comparing iso-vector and iso-scalar charmonium. This indicates the presence of contributions from lighter states made of light quarks and there is no reliable way to extract the mass of the charmonium state unless operators for these light mesons and glueballs are included in a GEVP basis. A careful study of these contributions is left for future work and these preliminary results exemplify the problem that arises with the presence of light quarks in the setup.

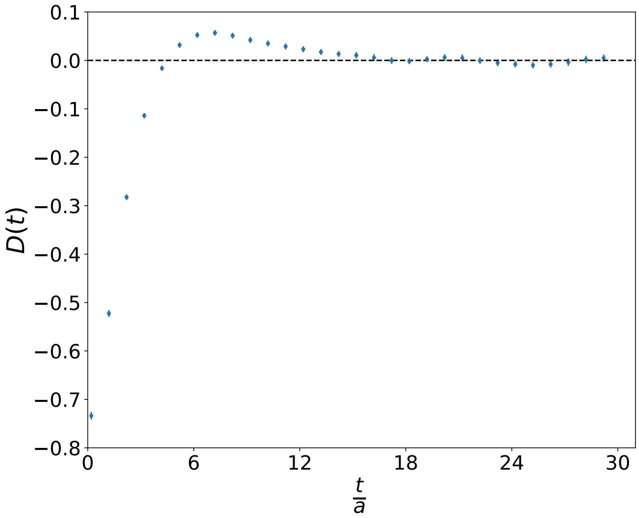

FIGURE 5.15: Disconnected contribution to the temporal correlation function of the $\Gamma = \gamma_5$ operator using standard distillation.

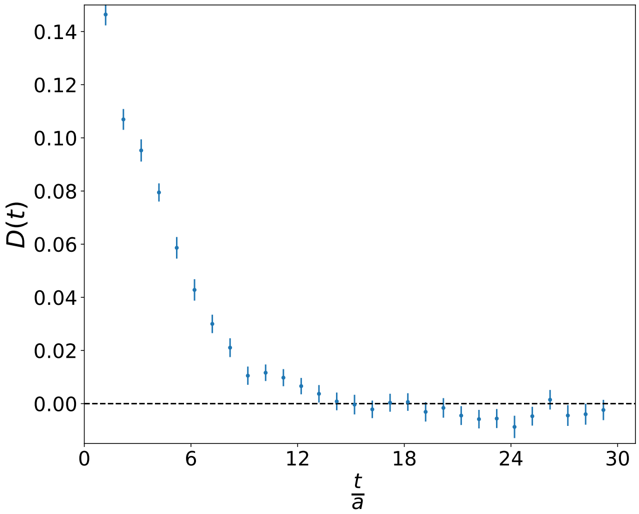

FIGURE 5.16: Disconnected contribution to the temporal correlation function of the $\Gamma = \mathbb{I}$ operator using standard distillation.

Chapter 6

Conclusions and outlook

> We shall not cease from exploration and the end of all our exploring will be to arrive where we started and know the place for the first time.
>
> T. S. Eliot

This work introduced an improvement to the distillation method via the optimal meson distillation profiles. These profiles lead to operators with earlier effective mass plateaus thanks to a suppression of excited-state contamination in their correlation functions. The optimality is defined via a GEVP for a fixed Γ operator in form $\bar{\psi}\Gamma\psi$, where the operator basis is built from different Gaussian quark profiles. The construction of the correlation matrix comes at no significant additional computational cost compared to the cost of the perambulators and elementals that are necessary for distillation. Optimal profiles which maximize the overlap with ground and excited states were obtained for a wide selection of local and derivative-based Γ operators. Unlike the constant profile in standard distillation, the optimal profiles introduce non-trivial structure that increased the overlap of the created states with the energy eigenstates for each Γ. In this way the proposed method provides a systematic way to individually improve meson operators. The method was also extended to the case of multiple Γ operators within a same symmetry channel, such that different spatial structures can be sampled via local and derivative-based Γ operators together with an optimal profile. Finally, optimal profiles of selected operators were used to build the spatial profile of the operator itself, a useful feature to examine its spatial behavior as well as finite-volume effects.

The proposed improvement was first tested for iso-vector operators in two different ensembles with $N_f = 2$ clover-improved Wilson quarks. The effective masses obtained from correlations of a wide variety of meson operators with both local and derivative-based Γ, including ones with exotic quantum numbers 1^{-+}, displayed a significant suppression of excited-state contamination when compared to standard distillation. Some examples of this improvement are $\Gamma = \gamma_5, \gamma_i, \gamma_0\gamma_5\gamma_i\nabla_i, \gamma_5\nabla_i$, where the resulting ground state mass plateaus were considerably longer than their standard distillation counterparts. Furthermore, an increase in the number of Laplacian eigenvectors used was shown to increase excited-state contamination in standard distillation while the use of an optimal profile avoids this problem by appropriately weighing the contributions of these additional vectors. The profiles also granted access to the first excited state for almost all Γ operators, something that with standard distillation would require the additional cost of calculating elementals for at least two different Γ operators. None of the resulting optimal profiles resembled a constant, showing a customized approach for every operator is a better choice than a constant profile. The improvement of the effective masses in terms of suppression of excited-state contamination and precision was found to be larger when using a fixed Γ operator with its optimal profile than when using two different Γ operators with standard distillation. This means optimizing the profile is not equivalent to optimizing a linear combination of different Γ operators. The former is computationally cheaper and leads to a more substantial improvement. Both approaches were also combined; different Γ operators together with an optimal profile lead to slightly larger suppression of excited-state contamination in the ground state compared to the case of a single Γ with its optimal profile, showing such an extended GEVP can still lead to an improvement.

Iso-scalar meson operators were also studied using the proposed method in the $N_f = 2$ ensembles and the suppression of excited-state contamination again observed. Using $\Gamma = \gamma_5$ and optimal profiles, the mass difference between the iso-scalar an iso-vector masses could be resolved in both ensembles, although the time interval from where these mass differences were extracted could perhaps still have residual excited-state contamination. Using $\Gamma = \mathbb{I}$ and its optimal profile it was possible to access the mass of the lightest state in the model, shown to coincide with the ground state mass obtained via 3D spatial Wilson loops in this same symmetry channel. These two types of operators were mixed to study the mesonic and gluonic contributions to the actual energy eigenstates. The ground state effective masses benefited from including the meson operator together with the Wilson loops, showing both contribute to this state. The first excited state could not be clearly accessed with the Wilson loops alone and only the meson operator significantly contributed to it. For this particular channel the basis profiles which had better access to the ground state also had the effective masses with the largest errors, which points to the possibility of there being a better choice of basis. Near-degeneracies in the masses of different Wilson loop operators were also seen which can affect the stability of the GEVP. Possible solutions to this issue will be explored in a future work.

Finally, the proposed improvement was used to calculate the low-lying charmonium spectrum on an $N_f = 3 + 1$ ensemble at the $SU(3)$ light flavor symmetric point with a physical charm quark. The masses of the 8 charmonium states which in nature are below the $D\bar{D}$ threshold were measured and shown to be in good agreement with their values in nature. The different mass splittings also displayed this same agreement and their statistical uncertainties were comparable, if not smaller, to the ones from state-of-the-art lattice calculations, some of which used larger statistics. All symmetry channels benefited from the significant suppression of excited-state contamination, which allowed to improve the values of some of them compared to a previous study of this same ensemble which did not employ distillation. Due to limited statistics only the connected contributions to the temporal correlation functions were used, however the disconnected contributions were also measured and will be used in a future study.

The profile optimization presented in this work has been used for the measurement of static potentials based on Laplacian trial states in [122]. Future directions of study based on this work include applying the method to light and D mesons, where for lighter quark masses one might need fewer eigenvectors. The corresponding elementals and profiles have to be appropriately modified and tuned. Scattering studies which use standard distillation, such as [138], can also benefit from the use of optimal profiles. The proposed method can also be combined with stochastic distillation [117], which is particularly useful for scattering studies such as in [139]. Since the estimation of the perambulators can be done independently from the calculation of the elementals, the construction of the optimal profiles via a GEVP formulation can be done just as in this work. The optimal meson profile formalism can also be extended to more general hadron operators such as baryons, where the corresponding elementals from standard distillation can be modified to include profiles that depend on three Laplacian eigenvalues instead of two. Further improvements to the distillation framework are also possible. The calculation of the perambulators represents the majority of the computational cost with or without the optimal profiles. The sparsity of the right-hand sides of the linear systems that must be solved together with the fact that only the orthogonal projections of the solutions onto a very low-dimensional subspace are required are features which could be exploited to reduce the overall computational cost. This would be particularly useful for the case of light quarks where the computationally expensive inversions are the main issue when deciding on the number of Laplacian eigenvectors to use.

Appendix A

The cubic group

Considering the three unitary vectors x, y and z one can characterize the cubic group by how each element acts on each of them. The action of each group element is listed below, where the ordering is not unique and the choice presented here corresponds to the one used by [140].

- g_0: $(x, y, z) \to (x, y, z)$
- g_1: $(x, y, z) \to (-x, -z, -y)$
- g_2: $(x, y, z) \to (z, x, y)$
- g_3: $(x, y, z) \to (-z, -y, -x)$
- g_4: $(x, y, z) \to (y, z, x)$
- g_5: $(x, y, z) \to (-y, -x, -z)$
- g_6: $(x, y, z) \to (x, -y, -z)$
- g_7: $(x, y, z) \to (-x, z, y)$
- g_8: $(x, y, z) \to (-z, x, -y)$
- g_9: $(x, y, z) \to (z, y, -x)$
- g_{10}: $(x, y, z) \to (-y, -z, x)$
- g_{11}: $(x, y, z) \to (y, -x, z)$
- g_{12}: $(x, y, z) \to (-x, y, -z)$
- g_{13}: $(x, y, z) \to (-z, -x, -y)$
- g_{14}: $(x, y, z) \to (-z, -x, y)$
- g_{15}: $(x, y, z) \to (z, -y, x)$
- g_{16}: $(x, y, z) \to (y, -z, -x)$
- g_{17}: $(x, y, z) \to (-y, x, z)$
- g_{18}: $(x, y, z) \to (-x, -y, z)$
- g_{19}: $(x, y, z) \to (x, -z, y)$
- g_{20}: $(x, y, z) \to (z, -x, -y)$
- g_{21}: $(x, y, z) \to (-z, y, x)$
- g_{22}: $(x, y, z) \to (-y, z, -x)$
- g_{23}: $(x, y, z) \to (y, x, -z)$

Appendix B

$C(t_G)$-orthonormality of plateau-averaged GEVP vectors

In the plateau region the vector at a given time $\omega_i(t)$ (omitting the t_G index for brevity) can be written as

$$\omega_i(t) = \omega_i^* + \delta_t^i, \tag{B.1}$$

where ω_i^* denotes the true vector of state i satisfying $\omega_i^* C(t_G)\omega_j^* = \delta_{ij}$ in the absence of any contamination and δ_t^i denotes the fluctuation at time t assumed to have statistical origin. For simplicity one can first consider the corresponding inner product between two vectors formed by the average of the $\omega_i(t)$ at two different values of t in the corresponding plateau region (which can be different for different i)

$$\omega_i^\dagger C(t_G)\omega_j = \frac{1}{2}\left(\omega_i^* + \delta_{t_1}^i + \omega_i^* + \delta_{t_2}^i\right)^\dagger C(t_G)\left(\omega_j^* + \delta_{t_3}^j + \omega_j^* + \delta_{t_4}^j\right)\frac{1}{2}, \tag{B.2}$$

from where the terms that do not become proportional to δ_{ij} are instead proportional to one of these forms:

- $\omega_i^{*\dagger} C(t_G)\delta_{t'}^j$
- $\delta_t^{i\dagger} C(t_G)\delta_{t'}^j$.

If one were to repeat these measurements over several Markov chains of gauge configurations then the expected value of this inner product is given by

$$\left\langle \omega_i(t)^\dagger C(t_G)\omega_j(t)\right\rangle$$

and the non-vanishing terms are of the form $\left\langle \omega_i^{*\dagger} C(t_G)\delta_t^j\right\rangle$ and $\left\langle \delta_t^{i\dagger} C(t_G)\delta_{t'}^j\right\rangle$. Assuming both ω_i^* and $C(t_G)$ are constant over such a chain of measurements then any term of the form $\left\langle \omega_i^{*\dagger} C(t_G)\delta_t^j\right\rangle$ vanishes, as over these different measurements δ_t^j should oscillate around zero if Eqn. (B.1) is an unbiased estimator of ω_i^*. The quadratic terms of the form $\left\langle \delta_t^{i\dagger} C(t_G)\delta_{t'}^j\right\rangle$ do not vanish as long as all δ_t^i are not zero and take the form of a covariance which quantifies the deviation of $\langle\omega_i(t)^\dagger C(t_G)\omega_j(t)\rangle$ from δ_{ij}. The better the estimator in Eqn. (B.1) becomes in terms of having δ_t^i fluctuating much closer to 0 then the closer $\langle\omega_i(t)^\dagger C(t_G)\omega_j(t)\rangle$ comes to being δ_{ij}. The extension of this analysis to a more general weighted average to define the estimators is straightforward and will exhibit the same dependence only on the terms quadratic in the δ_t^i. One can express $C(t_G)$ as an estimator of the true correlation matrix and repeat this same analysis yet the result is equal in essence; the only non-vanishing terms are covariances between fluctuations from the different estimators involved and the inner product becomes closer to δ_{ij} the better these estimators become. With these considerations, the average vectors are expected to be $C(t_G)$-orthonormal within statistical errors.

Appendix C

Conventions

The conventions for the Euclidean Dirac matrices used in this work are those of qcdlib, namely

$$\gamma_0 = \begin{bmatrix} 0 & 0 & -1 & 0 \\ 0 & 0 & 0 & -1 \\ -1 & 0 & 0 & 0 \\ 0 & -1 & 0 & 0 \end{bmatrix} \tag{C.1}$$

$$\gamma_1 = \begin{bmatrix} 0 & 0 & 0 & -i \\ 0 & 0 & -i & 0 \\ 0 & i & 0 & 0 \\ i & 0 & 0 & 0 \end{bmatrix} \tag{C.2}$$

$$\gamma_2 = \begin{bmatrix} 0 & 0 & 0 & -1 \\ 0 & 0 & 1 & 0 \\ 0 & 1 & 0 & 0 \\ -1 & 0 & 0 & 0 \end{bmatrix} \tag{C.3}$$

$$\gamma_3 = \begin{bmatrix} 0 & 0 & -i & 0 \\ 0 & 0 & 0 & i \\ i & 0 & 0 & 0 \\ 0 & -i & 0 & 0 \end{bmatrix} \tag{C.4}$$

$$\gamma_4 = -\gamma_0 \tag{C.5}$$

$$\gamma_5 = \gamma_0\gamma_1\gamma_2\gamma_3 = \begin{bmatrix} 1 & 0 & 0 & 0 \\ 0 & 1 & 0 & 0 \\ 0 & 0 & -1 & 0 \\ 0 & 0 & 0 & -1 \end{bmatrix} \tag{C.6}$$

$$C = -\gamma_0\gamma_2 \tag{C.7}$$

Bibliography

1. Gell-Mann, M. A schematic model of baryons and mesons. *Physics Letters* **8,** 214–215. ISSN: 0031-9163. `https://www.sciencedirect.com/science/article/pii/S0031916364920013` (1964).
2. Zweig, G. *An* SU_3 *model for strong interaction symmetry and its breaking I* en. 2002. `https://cds.cern.ch/record/352337`.
3. Zweig, G. *An* SU_3 *model for strong interaction symmetry and its breaking II* en. 2002. `http://cds.cern.ch/record/570209`.
4. Workman, R. L. & Others. Review of Particle Physics. *PTEP* **2022,** 083C01 (2022).
5. Close, F. E. *Introduction to Quarks and Partons* en (Academic Press, San Diego, CA, Mar. 1979).
6. Okubo, S. ϕ-meson and unitary symmetry model. *Physics Letters* **5,** 165–168. ISSN: 0031-9163. `https://www.sciencedirect.com/science/article/pii/S0375960163925489` (1963).
7. Iizuka, J. A Systematics and Phenomenology of Meson Family*. *Progress of Theoretical Physics Supplement* **37-38,** 21–34. ISSN: 0375-9687. eprint: `https://academic.oup.com/ptps/article-pdf/doi/10.1143/PTPS.37.21/5215468/37-38-21.pdf`. `https://doi.org/10.1143/PTPS.37.21` (Mar. 1966).
8. Jaffe, R. & Johnson, K. Unconventional states of confined quarks and gluons. *Physics Letters B* **60,** 201–204. ISSN: 0370-2693. `https://www.sciencedirect.com/science/article/pii/0370269376904238` (1976).
9. Mathieu, V., Kochelev, N. & Vento, V. The Physics of Glueballs. *International Journal of Modern Physics E* **18,** 1–49. `https://doi.org/10.1142/s0218301309012124` (Jan. 2009).
10. Ochs, W. The status of glueballs. *Journal of Physics G: Nuclear and Particle Physics* **40,** 043001. `https://doi.org/10.1088/0954-3899/40/4/043001` (Feb. 2013).
11. Chen, Y. *et al.* Glueball spectrum and matrix elements on anisotropic lattices. *Physical Review D* **73.** `https://doi.org/10.1103/physrevd.73.014516` (Jan. 2006).
12. Lucini, B., Teper, M. & Wenger, U. Glueballs and k-strings in SU(N) gauge theories: calculations with improved operators. *Journal of High Energy Physics* **2004,** 012–012. `https://doi.org/10.1088/1126-6708/2004/06/012` (June 2004).
13. Lucini, B., Rago, A. & Rinaldi, E. Glueball masses in the large N limit. *Journal of High Energy Physics* **2010.** `https://doi.org/10.1007/jhep08(2010)119` (Aug. 2010).
14. Morningstar, C. J. & Peardon, M. Glueball spectrum from an anisotropic lattice study. *Phys. Rev. D* **60,** 034509. `https://link.aps.org/doi/10.1103/PhysRevD.60.034509` (3 1999).

15. Liang, Y., Liu, K., Li, B., Dong, S. & Ishikawa, K. Lattice calculation of glueball matrix elements. *Physics Letters B* **307,** 375–382. ISSN: 0370-2693. `https://www.sciencedirect.com/science/article/pii/037026939390236B` (1993).
16. Levkova, L. & DeTar, C. Charm annihilation effects on the hyperfine splitting in charmonium. *Phys. Rev. D* **83,** 074504. `https://link.aps.org/doi/10.1103/PhysRevD.83.074504` (7 2011).
17. Hatton, D. *et al.* Charmonium properties from lattice QCD + QED: Hyperfine splitting, J/ψ leptonic width, charm quark mass, and a_μ^c. *Phys. Rev. D* **102,** 054511. `https://link.aps.org/doi/10.1103/PhysRevD.102.054511` (5 2020).
18. Zhang, R. *et al.* Annihilation diagram contribution to charmonium masses *. *Chinese Physics C* **46,** 043102. `https://dx.doi.org/10.1088/1674-1137/ac3d8c` (2022).
19. Follana, E. *et al.* Highly improved staggered quarks on the lattice with applications to charm physics. *Phys. Rev. D* **75,** 054502. `https://link.aps.org/doi/10.1103/PhysRevD.75.054502` (5 2007).
20. Bodwin, G. T., Braaten, E. & Lepage, G. P. Rigorous QCD analysis of inclusive annihilation and production of heavy quarkonium. *Phys. Rev. D* **51,** 1125–1171. `https://link.aps.org/doi/10.1103/PhysRevD.51.1125` (3 1995).
21. Adkins, G. S. *Application of the bound state formalism to positronium* in *AIP Conference Proceedings* (AIP, 1989). `https://doi.org/10.1063/1.38442`.
22. Karplus, R. & Klein, A. Electrodynamic Displacement of Atomic Energy Levels. III. The Hyperfine Structure of Positronium. *Phys. Rev.* **87,** 848–858. `https://link.aps.org/doi/10.1103/PhysRev.87.848` (5 1952).
23. Peardon, M. *et al.* Novel quark-field creation operator construction for hadronic physics in lattice QCD. *Physical Review D* **80.** `https://doi.org/10.1103/physrevd.80.054506` (Sept. 2009).
24. Wilson, K. G. Confinement of quarks. **10,** 2445–2459. `https://doi.org/10.1103/physrevd.10.2445` (Oct. 1974).
25. Gattringer, C. & Lang, C. B. *Quantum Chromodynamics on the Lattice* `https://doi.org/10.1007/978-3-642-01850-3` (Springer Berlin Heidelberg, 2010).
26. Knechtli, F., Günther, M. & Peardon, M. *Lattice Quantum Chromodynamics* `https://doi.org/10.1007/978-94-024-0999-4` (Springer Netherlands, 2017).
27. Weber, J., Diehl, S., Kuske, T. & Wagner, M. *An introduction to lattice hadron spectroscopy for students without quantum field theoretical background* 2013. arXiv: `1310.1760 [hep-lat]`.
28. Montvay, I. & Münster, G. *Quantum Fields on a Lattice* (Cambridge University Press, 1994).
29. Peskin, M. E. & Schroeder, D. V. *An introduction to quantum field theory* (Westview Press, Philadelphia, PA, Sept. 1995).
30. Itzykson, C. & Zuber, J.-B. *Quantum Field Theory* (Dover Publications, Mineola, NY, Feb. 2006).
31. Shindler, A. Twisted mass lattice QCD. *Physics Reports* **461,** 37–110. `https://doi.org/10.1016/j.physrep.2008.03.001` (May 2008).
32. Luscher, M. & Weisz, P. On-Shell Improved Lattice Gauge Theories. *Commun. Math. Phys.* **97.** [Erratum: Commun.Math.Phys. 98, 433 (1985)], 59 (1985).

33. Nielsen, H. & Ninomiya, M. A no-go theorem for regularizing chiral fermions. *Physics Letters B* **105,** 219–223. ISSN: 0370-2693. `https://www.sciencedirect.com/science/article/pii/0370269381910261` (1981).

34. Sheikholeslami, B. & Wohlert, R. Improved Continuum Limit Lattice Action for QCD with Wilson Fermions. *Nucl. Phys. B* **259,** 572 (1985).

35. Lüscher, M., Sint, S., Sommer, R. & Weisz, P. Chiral symmetry and O(a) improvement in lattice QCD. *Nuclear Physics B* **478,** 365–397. ISSN: 0550-3213. `https://www.sciencedirect.com/science/article/pii/0550321396003781` (1996).

36. Fritzsch, P., Sommer, R., Stollenwerk, F. & Wolff, U. Symanzik improvement with dynamical charm: a 3+1 scheme for Wilson quarks. *Journal of High Energy Physics* **2018.** `https://doi.org/10.1007%2Fjhep06%282018%29025` (2018).

37. Jansen, K. & Sommer, R. O(a) improvement of lattice QCD with two flavors of Wilson quarks. *Nuclear Physics B* **530,** 185–203. ISSN: 0550-3213. `https://www.sciencedirect.com/science/article/pii/S0550321398003964` (1998).

38. Symanzik, K. Continuum limit and improved action in lattice theories: (I). Principles and ϕ^4 theory. *Nuclear Physics B* **226,** 187–204. ISSN: 0550-3213. `https://www.sciencedirect.com/science/article/pii/0550321383904686` (1983).

39. Symanzik, K. Continuum limit and improved action in lattice theories: (II). O(N) non-linear sigma model in perturbation theory. *Nuclear Physics B* **226,** 205–227. ISSN: 0550-3213. `https://www.sciencedirect.com/science/article/pii/0550321383904698` (1983).

40. Altmann, S. L. & Herzig, P. *Point-group Theory Tables* - ISBN: 978-0-198-55226-0 (Clarendon Press, Oxford, 1994).

41. Mandula, J. E., Zweig, G. & Govaerts, J. Representations of the rotation reflection symmetry group of the four-dimensional cubic lattice. *Nuclear Physics B* **228,** 91–108. ISSN: 0550-3213. `https://www.sciencedirect.com/science/article/pii/0550321383903991` (1983).

42. Johnson, R. Angular momentum on a lattice. *Physics Letters B* **114,** 147–151. `https://doi.org/10.1016/0370-2693(82)90134-4` (July 1982).

43. Bunker, P. R. & Jensen, P. *Molecular symmetry and spectroscopy* 2nd ed. (NRC Press, Ottawa, ON, Canada, Jan. 1998).

44. Cornwell, J. F. *Group Theory in Physics: Volume 1* en (Academic Press, San Diego, CA, July 1997).

45. Dudek, J. J., Edwards, R. G., Mathur, N. & Richards, D. G. Charmonium excited state spectrum in lattice QCD. *Phys. Rev. D* **77,** 034501. `https://link.aps.org/doi/10.1103/PhysRevD.77.034501` (3 2008).

46. Irges, N. & Knechtli, F. Lattice gauge theory approach to spontaneous symmetry breaking from an extra dimension. *Nuclear Physics B* **775,** 283–311 (July 2007).

47. Lüscher, M. & Wolff, U. How to calculate the elastic scattering matrix in two-dimensional quantum field theories by numerical simulation. *Nuclear Physics B* **339,** 222–252. ISSN: 0550-3213. `https://www.sciencedirect.com/science/article/pii/055032139090540T` (1990).

48. Blossier, B., Morte, M. D., von Hippel, G., Mendes, T. & Sommer, R. On the generalized eigenvalue method for energies and matrix elements in lattice field theory. *Journal of High Energy Physics* **2009,** 094–094. `https://doi.org/10.1088/1126-6708/2009/04/094` (2009).

49. Fischer, M. *et al.* On the generalised eigenvalue method and its relation to Prony and generalised pencil of function methods. *The European Physical Journal A* **56.** `https://doi.org/10.1140/epja/s10050-020-00205-w` (Aug. 2020).

50. Dudek, J. J., Edwards, R. G., Peardon, M. J., Richards, D. G. & Thomas, C. E. Toward the excited meson spectrum of dynamical QCD. *Physical Review D* **82.** `https://doi.org/10.1103/physrevd.82.034508` (Aug. 2010).

51. Bulava, J. *et al.* String breaking by light and strange quarks in QCD. *Physics Letters B* **793,** 493–498. ISSN: 0370-2693. `https://www.sciencedirect.com/science/article/pii/S0370269319303284` (2019).

52. Koch, V. *String breaking from Lattice QCD with* $N_f = 2 + 1$ *dynamical fermions* PhD thesis (Trinity College Dublin, 2019).

53. Balog, J. *et al.* Comparison of the O(3) bootstrap σ model with lattice regularization at low energies. *Phys. Rev. D* **60,** 094508. `https://link.aps.org/doi/10.1103/PhysRevD.60.094508` (9 1999).

54. Niedermayer, F., Rüfenacht, P. & Wenger, U. Fixed point gauge actions with fat links: scaling and glueballs. *Nuclear Physics B* **597,** 413–450. ISSN: 0550-3213. `https://www.sciencedirect.com/science/article/pii/S0550321300007318` (2001).

55. Bailas, G., Blossier, B. & Morénas, V. Some hadronic parameters of charmonia in $N_f = 2$ lattice QCD. *The European Physical Journal C* **78.** `https://doi.org/10.1140/epjc/s10052-018-6495-4` (Dec. 2018).

56. Albanese, M. *et al.* Glueball masses and string tension in lattice QCD. *Physics Letters B* **192,** 163–169. `https://doi.org/10.1016/0370-2693(87)91160-9` (June 1987).

57. Hasenfratz, A. & Knechtli, F. Flavor symmetry and the static potential with hypercubic blocking. *Physical Review D* **64.** `https://doi.org/10.1103/physrevd.64.034504` (July 2001).

58. Morningstar, C. & Peardon, M. Analytic smearing of SU(3) link variables in lattice QCD. *Physical Review D* **69.** `https://doi.org/10.1103/physrevd.69.054501` (Mar. 2004).

59. Teper, M. An improved method for lattice glueball calculations. *Physics Letters B* **183,** 345–350. `https://doi.org/10.1016/0370-2693(87)90976-2` (Jan. 1987).

60. Capitani, S., Dürr, S. & Hoelbling, C. Rationale for UV-filtered clover fermions. *Journal of High Energy Physics* **2006,** 028–028. `https://doi.org/10.1088/1126-6708/2006/11/028` (Nov. 2006).

61. Bernard, C & DeGrand, T. Perturbation theory for fat-link fermion actions. *Nuclear Physics B - Proceedings Supplements* **83-84.** Proceedings of the XVIIth International Symposium on Lattice Field Theory, 845–847. ISSN: 0920-5632. `https://www.sciencedirect.com/science/article/pii/S092056320091822X` (2000).

62. Duane, S., Kennedy, A., Pendleton, B. J. & Roweth, D. Hybrid Monte Carlo. *Physics Letters B* **195,** 216–222. ISSN: 0370-2693. `https://www.sciencedirect.com/science/article/pii/037026938791197X` (1987).
63. Weingarten, D. & Petcher, D. Monte Carlo integration for lattice gauge theories with fermions. *Physics Letters B* **99,** 333–338. ISSN: 0370-2693. `https://www.sciencedirect.com/science/article/pii/037026938190112X` (1981).
64. Wolff, U. Monte Carlo errors with less errors. *Computer Physics Communications* **156,** 143–153. ISSN: 0010-4655. `https://www.sciencedirect.com/science/article/pii/S0010465503004673` (2004).
65. Schaefer, S., Sommer, R. & Virotta, F. Critical slowing down and error analysis in lattice QCD simulations. *Nuclear Physics B* **845,** 93–119. ISSN: 0550-3213. `https://www.sciencedirect.com/science/article/pii/S0550321310006188` (2011).
66. Joswig, F., Kuberski, S., Kuhlmann, J. T. & Neuendorf, J. *pyerrors: a python framework for error analysis of Monte Carlo data* 2022. `https://arxiv.org/abs/2209.14371`.
67. Ramos, A. Automatic differentiation for error analysis of Monte Carlo data. *Computer Physics Communications* **238,** 19–35. ISSN: 0010-4655. `https://www.sciencedirect.com/science/article/pii/S0010465519300013` (2019).
68. Güsken, S. *et al.* Non-singlet axial vector couplings of the baryon octet in lattice QCD. *Physics Letters B* **227,** 266 –269. ISSN: 0370-2693. `http://www.sciencedirect.com/science/article/pii/S0370269389800346` (1989).
69. Allton, C. R. *et al.* Gauge-invariant smearing and matrix correlators using Wilson fermions a β=6.2. *Physical Review D* **47,** 5128–5137. `https://doi.org/10.1103/physrevd.47.5128` (June 1993).
70. Güsken, S. A study of smearing techniques for hadron correlation functions. *Nuclear Physics B - Proceedings Supplements* **17,** 361 –364. ISSN: 0920-5632. `http://www.sciencedirect.com/science/article/pii/092056329090273W` (1990).
71. Best, C. *et al.* π and ρ structure functions from lattice QCD. *Physical Review D* **56,** 2743–2754. `https://doi.org/10.1103/physrevd.56.2743` (Sept. 1997).
72. Alexandrou, C., Güsken, S., Jegerlehner, F., Schilling, K. & Sommer, R. The static approximation of heavy-light quark systems. A detailed lattice study. *Nuclear Physics B* **414,** 815–855. `https://doi.org/10.1016/0550-3213(94)90262-3` (Feb. 1994).
73. Basak, S. *et al.* Group-theoretical construction of extended baryon operators in lattice QCD. *Physical Review D* **72.** `https://doi.org/10.1103/physrevd.72.094506` (Nov. 2005).
74. Alford, M., Klassen, T. & Lepage, P. The D234 action for light quarks. *Nuclear Physics B - Proceedings Supplements* **47,** 370–373. `https://doi.org/10.1016/0920-5632(96)00076-x` (Mar. 1996).
75. DeGrand, T. A. & Loft, R. D. Wave-function tests for lattice QCD spectroscopy. *Computer Physics Communications* **65,** 84 –91. ISSN: 0010-4655. `http://www.sciencedirect.com/science/article/pii/001046559190158H` (1991).
76. Lichtl, A. *et al.* Combining Quark and Link Smearing to Improve Extended Baryon Operators. `https://arxiv.org/abs/hep-lat/0509179` (2005).

77. Lanczos, C. An iteration method for the solution of the eigenvalue problem of linear differential and integral operators. *Journal of Research of the National Bureau of Standards* **45,** 255. `https://doi.org/10.6028/jres.045.026` (Oct. 1950).
78. Golub, G. H. & Loan, C. F. V. *Matrix Computations* Fourth Edition. ISBN: 1-4214-0794-9 (The Johns Hopkins University Press, Baltimore, 2013).
79. Trefethen, L. N. & Bau, D. *Numerical Linear Algebra* ISBN: 0-89871-361-7 (Society for Industrial and Applied Mathematics, Philadelphia, 1997).
80. Bai, Z., Demmel, J., Dongarra, J., Ruhe, A. & van der Vorst, H. *Templates for the Solution of Algebraic Eigenvalue Problems* (eds Bai, Z., Demmel, J., Dongarra, J., Ruhe, A. & van der Vorst, H.) eprint: `https://epubs.siam.org/doi/pdf/10.1137/1.9780898719581`. `https://epubs.siam.org/doi/abs/10.1137/1.9780898719581` (Society for Industrial and Applied Mathematics, 2000).
81. Paige, C. C. *The Computation of Eigenvalues and Eigenvectors of very large sparse matrices* PhD thesis (London University Institute of Computer Science, 1971).
82. Parlett, B. N. *The symmetric eigenvalue problem* (SIAM, 1998).
83. Parlett, B. A new look at the Lanczos algorithm for solving symmetric systems of linear equations. *Linear Algebra and its Applications* **29,** 323–346. `https://doi.org/10.1016/0024-3795(80)90248-7` (Feb. 1980).
84. Wu, K. & Simon, H. D. *Thick-restart Lanczos method for symmetric eigenvalue problems* in *Solving Irregularly Structured Problems in Parallel* (eds Ferreira, A., Rolim, J., Simon, H. & Teng, S.-H.) (Springer Berlin Heidelberg, Berlin, Heidelberg, 1998), 43–55.
85. Wu, K. & Simon, H. D. Dynamic Restarting Schemes for Eigenvalue Problems. `https://www.osti.gov/biblio/760299`.
86. Grcar, J. *Analyses of the Lanczos algorithm and of the approximation problem in Richardson's method* PhD thesis (University of Illinois at Urbana-Champaign, 1981).
87. Simon, H. D. The Lanczos algorithm with partial reorthogonalization. *Mathematics of Computation* **42,** 115–115. `https://doi.org/10.1090/s0025-5718-1984-0725988-x` (Jan. 1984).
88. Sorensen, D. C. & Yang, C. *Accelerating The Lanczos Algorithm Via Polynomial Spectral Transformations* tech. rep. (Rice University, 1997).
89. Dhillon, I. S. *A new* $O(n^2)$ *algorithm for the symmetric tridiagonal eigenvalue/eigenvector problem* tech. rep. (CALIFORNIA UNIV BERKELEY GRADUATE DIV, 1997).
90. Dhillon, I. S., Parlett, B. N. & Vömel, C. The Design and Implementation of the MRRR Algorithm. *ACM Trans. Math. Softw.* **32,** 533–560. ISSN: 0098-3500. `https://doi.org/10.1145/1186785.1186788` (Dec. 2006).
91. Dhillon, I. S. & Parlett, B. N. Multiple representations to compute orthogonal eigenvectors of symmetric tridiagonal matrices. *Linear Algebra and its Applications* **387,** 1–28. `https://doi.org/10.1016/j.laa.2003.12.028` (Aug. 2004).
92. Anderson, E. *et al. LAPACK Users' Guide* Third. ISBN: 0-89871-447-8 (paperback) (Society for Industrial and Applied Mathematics, Philadelphia, PA, 1999).

93. Saad, Y. *Iterative Methods for Sparse Linear Systems* Second. eprint: `https://epubs.siam.org/doi/pdf/10.1137/1.9780898718003`. `https://epubs.siam.org/doi/abs/10.1137/1.9780898718003` (Society for Industrial and Applied Mathematics, 2003).

94. Barrett, R. *et al. Templates for the Solution of Linear Systems: Building Blocks for Iterative Methods* eprint: `https://epubs.siam.org/doi/pdf/10.1137/1.9781611971538`. `https://epubs.siam.org/doi/abs/10.1137/1.9781611971538` (Society for Industrial and Applied Mathematics, 1994).

95. Saad, Y. & Schultz, M. H. GMRES: A Generalized Minimal Residual Algorithm for Solving Nonsymmetric Linear Systems. *SIAM Journal on Scientific and Statistical Computing* **7,** 856–869. eprint: `https://doi.org/10.1137/0907058`. `https://doi.org/10.1137/0907058` (1986).

96. Axelsson, O. Conjugate gradient type methods for unsymmetric and inconsistent systems of linear equations. *Linear Algebra and its Applications* **29.** Special Volume Dedicated to Alson S. Householder, 1–16. ISSN: 0024-3795. `https://www.sciencedirect.com/science/article/pii/0024379580902268` (1980).

97. Frommer, A., Kahl, K., Krieg, S., Leder, B. & Rottmann, M. Adaptive Aggregation-Based Domain Decomposition Multigrid for the Lattice Wilson–Dirac Operator. *SIAM Journal on Scientific Computing* **36,** A1581–A1608. eprint: `https://doi.org/10.1137/130919507`. `https://doi.org/10.1137/130919507` (2014).

98. Lüscher, M. `https://luscher.web.cern.ch/luscher/openQCD/`.

99. Lüscher, M. *Computational Strategies in Lattice QCD* 2010. `https://arxiv.org/abs/1002.4232`.

100. Lüscher, M. Local coherence and deflation of the low quark modes in lattice QCD. *Journal of High Energy Physics* **2007,** 081. `https://dx.doi.org/10.1088/1126-6708/2007/07/081` (2007).

101. Fritzsch, P. *et al.* The strange quark mass and Lambda parameter of two flavor QCD. *Nuclear Physics B* **865,** 397–429. ISSN: 0550-3213. `https://www.sciencedirect.com/science/article/pii/S0550321312004142` (2012).

102. Calì, S., Knechtli, F. & Korzec, T. How much do charm sea quarks affect the charmonium spectrum? *The European Physical Journal C* **79.** `https://doi.org/10.1140/epjc/s10052-019-7108-6` (July 2019).

103. Lüscher, M. Properties and uses of the Wilson flow in lattice QCD. *Journal of High Energy Physics* **2010.** `https://doi.org/10.1007/jhep08(2010)071` (Aug. 2010).

104. Athenodorou, A. *et al.* How perturbative are heavy sea quarks? *Nuclear Physics B* **943,** 114612. ISSN: 0550-3213. `https://www.sciencedirect.com/science/article/pii/S0550321319300926` (2019).

105. Fritzsch, P. *et al.* The strange quark mass and Lambda parameter of two flavor QCD. *Nuclear Physics B* **865,** 397–429. ISSN: 0550-3213. `https://www.sciencedirect.com/science/article/pii/S0550321312004142` (2012).

106. Lüscher, M. & Schaefer, S. Lattice QCD without topology barriers. *Journal of High Energy Physics* **2011.** `https://doi.org/10.1007/jhep07(2011)036` (July 2011).

107. Höllwieser, R., Knechtli, F. & Korzec, T. Scale setting for N_f=3+1 QCD. *The European Physical Journal C* **80.** `https://doi.org/10.1140/epjc/s10052-020-7889-7` (Apr. 2020).
108. Burch, T., Hagen, C., Hetzenegger, M. & Schäfer, A. Low and high spin mesons from $N_f = 2$ clover-Wilson lattices. *Phys. Rev. D* **79,** 114503. `https://link.aps.org/doi/10.1103/PhysRevD.79.114503` (11 2009).
109. Gattringer, C., Glozman, L. Y., Lang, C. B., Mohler, D. & Prelovsek, S. Derivative sources in lattice spectroscopy of excited light-quark mesons. *Phys. Rev. D* **78,** 034501. `https://link.aps.org/doi/10.1103/PhysRevD.78.034501` (3 2008).
110. Liu, L. *et al.* Excited and exotic charmonium spectroscopy from lattice QCD. *Journal of High Energy Physics* **2012.** `https://doi.org/10.1007/jhep07(2012)126` (July 2012).
111. Dudek, J. J., Edwards, R. G., Peardon, M. J., Richards, D. G. & Thomas, C. E. Highly Excited and Exotic Meson Spectrum from Dynamical Lattice QCD. *Phys. Rev. Lett.* **103,** 262001. `https://link.aps.org/doi/10.1103/PhysRevLett.103.262001` (26 2009).
112. Georgi, H. *Lie algebras in particle physics* (Westview Press, Philadelphia, PA, Oct. 1999).
113. Rykhlinskaya, K. & Fritzsche, S. Generation of Clebsch–Gordan coefficients for the point and double groups. *Computer Physics Communications* **174,** 903–913. `https://doi.org/10.1016/j.cpc.2006.01.001` (June 2006).
114. Liao, X. & Manke, T. *Excited charmonium spectrum from anisotropic lattices* 2002. `https://arxiv.org/abs/hep-lat/0210030`.
115. Dudek, J. J. & Rrapaj, E. Charmonium in lattice QCD and the nonrelativistic quark model. *Physical Review D* **78.** `https://doi.org/10.1103/physrevd.78.094504` (Nov. 2008).
116. Meyer, C. A. & Van Haarlem, Y. Status of exotic-quantum-number mesons. *Phys. Rev. C* **82,** 025208. `https://link.aps.org/doi/10.1103/PhysRevC.82.025208` (2 2010).
117. Morningstar, C. *et al.* Improved stochastic estimation of quark propagation with Laplacian Heaviside smearing in lattice QCD. *Physical Review D* **83.** `https://doi.org/10.1103/physrevd.83.114505` (June 2011).
118. Cheung, G. K. *et al.* Excited and exotic charmonium, D s and D meson spectra for two light quark masses from lattice QCD. *Journal of High Energy Physics* **2016.** `https://doi.org/10.1007/jhep12(2016)089` (Dec. 2016).
119. Dudek, J. J., Edwards, R. G., Guo, P. & Thomas, C. E. Toward the excited isoscalar meson spectrum from lattice QCD. *Physical Review D* **88.** `https://doi.org/10.1103/physrevd.88.094505` (Nov. 2013).
120. Knechtli, F., Korzec, T., Peardon, M. & Urrea-Niño, J. A. Optimizing creation operators for charmonium spectroscopy on the lattice. *Phys. Rev. D* **106,** 034501. `https://link.aps.org/doi/10.1103/PhysRevD.106.034501` (3 2022).
121. Bali, G. S., Collins, S. & Ehmann, C. Charmonium spectroscopy and mixing with light quark and open charm states from $n_F = 2$ lattice QCD. *Phys. Rev. D* **84,** 094506. `https://link.aps.org/doi/10.1103/PhysRevD.84.094506` (9 2011).

122. Höllwieser, R., Knechtli, F., Korzec, T., Peardon, M. & Urrea-Niño, J. A. Constructing static quark-antiquark creation operators from Laplacian eigenmodes. *Phys. Rev. D* **107,** 034511. `https://link.aps.org/doi/10.1103/PhysRevD.107.034511` (3 2023).

123. Nishida, N. & Vidal, G. Conversion to tail recursion in term rewriting. *The Journal of Logic and Algebraic Programming* **83,** 53–63. ISSN: 1567-8326. `https://www.sciencedirect.com/science/article/pii/S1567832613000313` (2014).

124. Parlett, B. N. & Scott, D. S. The Lanczos algorithm with selective orthogonalization. *Mathematics of Computation* **33,** 217–238. `https://doi.org/10.1090/s0025-5718-1979-0514820-3` (Jan. 1979).

125. Donnellan, M., Knechtli, F., Leder, B. & Sommer, R. Determination of the static potential with dynamical fermions. *Nuclear Physics B* **849,** 45–63. ISSN: 0550-3213. `https://www.sciencedirect.com/science/article/pii/S0550321311001647` (2011).

126. DeTar, C., Kronfeld, A. S., Lee, S.-h., Mohler, D. & Simone, J. N. Splittings of low-lying charmonium masses at the physical point. *Phys. Rev. D* **99,** 034509. `https://link.aps.org/doi/10.1103/PhysRevD.99.034509` (3 2019).

127. Vadacchino, D. *A review on Glueball hunting* 2023. `https://arxiv.org/abs/2305.04869`.

128. McNeile, C., Michael, C. & Sharkey, K. J. Flavor singlet mesons in QCD. *Phys. Rev. D* **65,** 014508. `https://link.aps.org/doi/10.1103/PhysRevD.65.014508` (1 2001).

129. Brandstaeter, F., Kronfeld, A. & Schierholz, G. Critical signal-to-noise ratio and glueball mass calculations. *Nuclear Physics B* **345,** 709–729. ISSN: 0550-3213. `https://www.sciencedirect.com/science/article/pii/0550321390904064` (1990).

130. Berg, B. & Billoire, A. Glueball spectroscopy in 4d SU(3) lattice gauge theory (I). *Nuclear Physics B* **221,** 109–140. `https://doi.org/10.1016/0550-3213(83)90620-x` (July 1983).

131. Sakai, K. & Sasaki, S. Glueball spectroscopy in lattice QCD using gradient flow. *Phys. Rev. D* **107,** 034510. `https://link.aps.org/doi/10.1103/PhysRevD.107.034510` (3 2023).

132. Sun, W. *et al.* Glueball spectrum from Nf = 2 lattice QCD study on anisotropic lattices*. *Chinese Physics C* **42,** 093103. `https://dx.doi.org/10.1088/1674-1137/42/9/093103` (2018).

133. Lüscher, M. & Weisz, P. Definition and general properties of the transfer matrix in continuum limit improved lattice gauge theories. *Nuclear Physics B* **240,** 349–361. ISSN: 0550-3213. `https://www.sciencedirect.com/science/article/pii/0550321384902700` (1984).

134. Necco, S. *The static quark potential and scaling behavior of SU(3) l attice Yang-Mills theory* 2003. `https://arxiv.org/abs/hep-lat/0306005`.

135. Guagnelli, M., Heitger, J., Sommer, R. & Wittig, H. Hadron masses and matrix elements from the QCD Schrödinger functional. *Nuclear Physics B* **560,** 465–481. ISSN: 0550-3213. `https://www.sciencedirect.com/science/article/pii/S0550321399004666` (1999).

136. Bruno, M. *The energy scale of the 3-flavour Lambda parameter* PhD thesis (Humboldt U., Berlin, 2015).

137. Bruno, M., Korzec, T. & Schaefer, S. Setting the scale for the CLS 2+1 flavor ensembles. *Physical Review D* **95.** `https://doi.org/10.1103/physrevd.95.074504` (Apr. 2017).
138. Moir, G. *et al.* Coupled-channel Dπ, Dη and $D_s\bar{K}$ scattering from lattice QCD. *Journal of High Energy Physics* **2016.** `https://doi.org/10.1007/jhep10(2016)011` (Oct. 2016).
139. Prelovsek, S., Collins, S., Mohler, D., Padmanath, M. & Piemonte, S. Charmonium-like resonances with $J^{PC} = 0^{++}$, 2^{++} in coupled $D\bar{D}$, $D_s\bar{D}_s$ scattering on the lattice. *Journal of High Energy Physics* **2021.** `https://doi.org/10.1007/jhep06(2021)035` (June 2021).
140. Peardon, M. Private communication. 2020.